Alma Mater Studiorum – Università di Bologna

Facoltà di Scienze Matematiche, Fisiche e Naturali
Dipartimento di Astronomia

DOTTORATO DI RICERCA IN
ASTRONOMIA
Ciclo XXIII

Settore scientifico–disciplinare: Area 02 – Scienze Fisiche
FIS/05 Astronomia e Astrofisica

Dynamics of the halo gas in disc galaxies

Presentata da:
Federico Marinacci

Coordinatore:
Chiar.mo Prof. Lauro Moscardini

Relatore:
Chiar.mo Prof. Luca Ciotti

Co-relatori:
Dr. Filippo Fraternali
Dr. Carlo Nipoti

Esame finale anno 2011

To my family.

Contents

Abstract

This Thesis studies the dynamics of hot and cold gas outside the plane in galaxies like the Milky-Way (extra-planar gas) and focuses on the interaction between disc and halo material. Stationary models for the cold phase of the extra-planar gas are presented. They show that the kinematics of this phase must be influenced by the interaction with an ambient medium that we identify as the hot cosmological corona that surrounds disc galaxies. To study this interaction a novel hydrodynamical code has been implemented and a series of hydrodynamical simulations has been run to investigate the mass and momentum exchange between the cold extra-planar gas clouds and the hot corona. These simulations show that the coronal gas can condense efficiently in the turbulent wakes that form behind the cold clouds and it can be accreted by the disc to sustain star formation. They also predict that the corona cannot be a static structure but it must rotate and lag by $\sim 80 - 120\,\mathrm{km\,s^{-1}}$ with respect to the disc. Implications of the results of this Thesis for the evolution of star-forming galaxies and for the large-scale dynamics of galactic coronae are also briefly discussed.

1

Introduction

1.1 Halo gas in disc galaxies

In the past years much observational evidence has accumulated on the presence of multiphase gaseous layers in the halo region of spiral galaxies. This multiphase halo gas, also known as *extra-planar* gas[1], is readily explained by admitting the existence of flows of material towards and away from galactic discs. This is in agreement with the idea that galaxy discs are in dynamical connection with their environment and this connection, in the form of gas circulation, can strongly influence their evolution.

Halo gas can be produced by different mechanisms that are divided, on the basis of the origin of the gas, into internal and external. In internal mechanisms, it is supposed that the extra-planar gas is material originally located in the disc – hence galactic material – from which it is ejected by some process internal to the galaxy. On the other hand, in external mechanisms, the material is not of galactic origin. Note that the two frameworks just illustrated are not mutually exclusive as we will see later.

The most obvious internal cause of the halo gas is represented by the

[1]This term is more used for gas close to the plane, within say $\sim 5\,\mathrm{kpc}$.

(mechanical) energy that stellar feedback deposits in the interstellar medium of the galaxy. Part of this energy may be used to eject a fraction of the gas contained in the disc out of the galactic plane, a mechanism which is known as galactic fountain (Shapiro & Field 1976; Bregman 1980). In this scenario, partially ionised gas clouds are pushed out of the disc by the combined action of supernova explosions and stellar winds. It is usually assumed that the ejected clouds travel through the halo on almost ballistic trajectories, i.e. under the influence of the galaxy gravitational field only, and eventually fall back into the disc, given that ejection velocity is typically much lower than the escape velocity from the galaxy. The ballistic treatment of the galactic fountain is able to reproduce the distribution of the extra-planar gas observed in nearby spiral galaxies (Fraternali & Binney 2006), but there are inconsistencies between the predicted and the observed kinematics (see Section 1.1.1).

The interest for an extra-galactic origin of the halo gas is due to the fact that galaxy evolution is regulated by the availability of cold gas, which is necessary to form stars. It is well known that gas contained in the star-forming discs of galaxies like the Milky-Way would be exhausted in $\sim 1\,\mathrm{Gyr}$ at the typical star-formation rate of $\sim 1\,\mathrm{M}_\odot\,\mathrm{yr}^{-1}$. However, determinations of the star formation history in the Milky-Way (Twarog 1980; Cignoni et al. 2006) have shown that our Galaxy has formed stars at an approximately constant rate during its life. Therefore, accretion of external gas, to replace that consumed by star formation, becomes mandatory. Several mechanisms have been proposed as, for instance, merging with gas rich satellites (Sancisi et al. 2008), accretion of cold gas clouds, such as the Milky-Way's high-velocity clouds (Fraternali et al. 2007), and cold flows from the intergalactic medium (Kereš et al. 2009).

In the following Sections current observational evidence for the different phases of the extra-planar gas will be briefly presented together with some open issues concerning its interpretation.

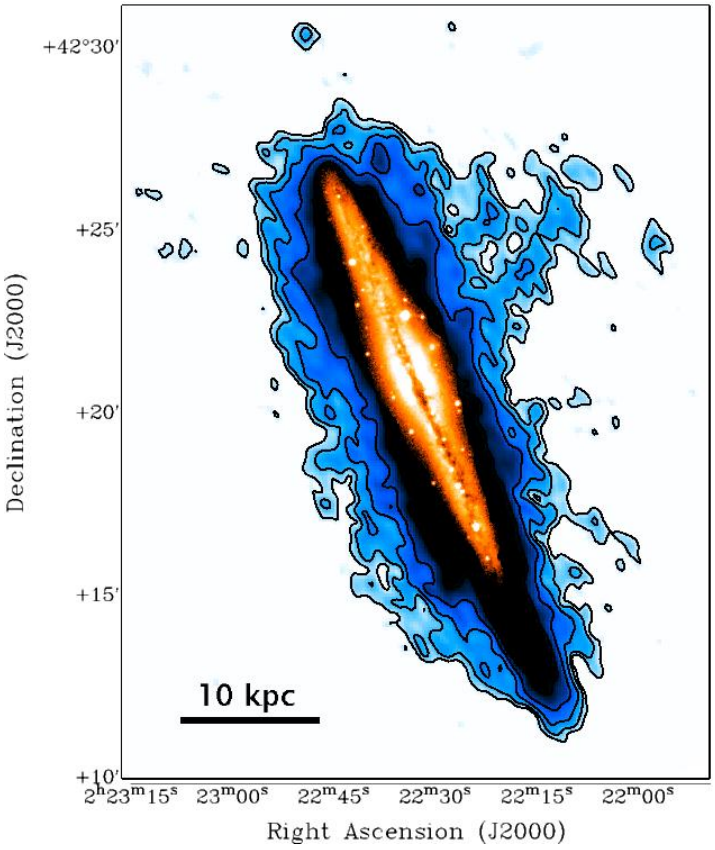

Figure 1.1: Contours of the total H I emission map for NGC 891 overlaid on the optical image of the galaxy (from Oosterloo et al. 2007). Note the extension of the H I halo emission, which reaches distances of $\sim 10\,\mathrm{kpc}$ from the stellar disc.

1.1.1 Neutral gas

The main difficulty associated to the observation of neutral gas in the halo region of nearby spiral galaxies is its low column density and very sensitive observations are required to detect this faint emission. For instance, a typical value for the hydrogen column density in the disc is $N_{\mathrm{H\,I}}$ is $\sim 10^{21}\,\mathrm{cm}^{-2}$, while in the halo region $N_{\mathrm{H\,I}} \sim 10^{19-20}\,\mathrm{cm}^{-2}$. In edge-on galaxies, one can spatially separate the H I halo emission from that of the disc, and neutral extra-planar gas has been traced at heights up to $\sim 10 - 20\,\mathrm{kpc}$ above the galactic plane. Figure 1.1 shows the H I extra-planar emission of the

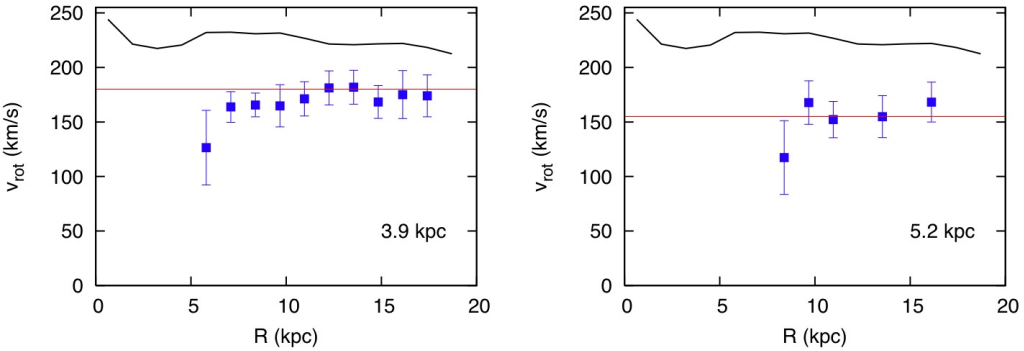

Figure 1.2: H I rotation curves of NGC 891 (points with error bars) at an height of 3.9 kpc (left panel) and 5.2 kpc (right panel) above the plane. The solid black line shows for comparison the rotation curve of the disc while the solid red line highlights the decrease of the gas rotational velocity with increasing distance from the plane (vertical gradient). The gradient is $\simeq -15\,\mathrm{km\,s^{-1}\,kpc^{-1}}$ and very regular (approximately constant) at any given height (from Fraternali et al. 2005).

edge-on galaxy NGC 891, the most prominent H I halo so far. The mass of the H I halo of this galaxy amounts to about 25% of the total H I mass (Oosterloo et al. 2007), while typically, in galaxies that have been observed with enough sensitivity, it is around 10% (Sancisi et al. 2008).

The kinematics of the neutral phase of the extra-planar gas is well studied and its most remarkable feature is represented by a regularly decreasing rotational velocity with increasing height above the galactic plane (vertical velocity gradient). In the case of NGC 891 (see Figure 1.2) a gradient of $\simeq -15\,\mathrm{km\,s^{-1}\,kpc^{-1}}$ has been measured both in H I and in ionised gas (Oosterloo et al. 2007; Heald et al. 2006a; Kamphuis et al. 2007). In our Galaxy Marasco & Fraternali (2011) found that the magnitude of the vertical gradient is again $\simeq -15\,\mathrm{km\,s^{-1}\,kpc^{-1}}$. Similar values have been estimated for other spirals (Fraternali 2010). The kinematics of the extra-planar H I gas shows also the presence of non-circular motions and in particular a possible large-scale radial inflow is observed (Fraternali et al. 2001).

The most likely process at the origin of these H I haloes, and indeed of most of the extra-planar gas phenomenon in the vicinity (say within

$\sim 5\,\mathrm{kpc}$) of the disc, is the galactic fountain. There are several observational indications that properties of the neutral halo gas, such as high-velocity features observed in nearly face-on galaxies, are tightly associated to star-forming regions in the galaxy (Boomsma et al. 2008). Moreover, H I haloes are quite massive and if they were of external origin, their accretion on to galactic discs would lead to implausibly high accretion rates, substantially exceeding the present-day star formation rates observed in nearby spiral galaxies (Fraternali & Binney 2008).

Alternative descriptions have been also proposed to model the dynamical state of the neutral extra-planar gas, such as turbulence (Struck & Smith 2009) or stationary fluid configurations (Barnabè et al. 2006). These latter successfully reproduce the observed decline in the rotational velocity of the gas with increasing distances from the plane. However, the temperature required for the gas to be in hydrostatic equilibrium with the vertical gravitational field of the galaxy is of the order of $10^5\,\mathrm{K}$, and the relation of this medium to the cold neutral extra-planar gas is not straightforward. A new class of stationary models, which are based on the stationary Jeans equations and can directly describe the neutral gas, are presented in Chapter 2 of this Thesis.

Ballistic galactic fountain models, while able to reproduce the observed vertical distribution of the H I in galactic haloes, predict a kinematics which is not in agreement with the observational findings. In particular, the theoretical rotational velocity of the H I gas is always higher than the observed one. In other words, a ballistic galactic fountain underestimates the vertical velocity gradient of the extra-planar gas. This is illustrated in Figure 1.3 where two rotation curves (points with error bars) of the extra-planar H I gas of NGC 891, taken at different heights above the plane, are presented, together with the predictions of a ballistic fountain model (red lines). The grey dashed lines in each panel show, for comparison, the rotation curve of the disc to make apparent the vertical velocity gradient of the halo gas, while the blue lines show the results of a fountain model that includes ac-

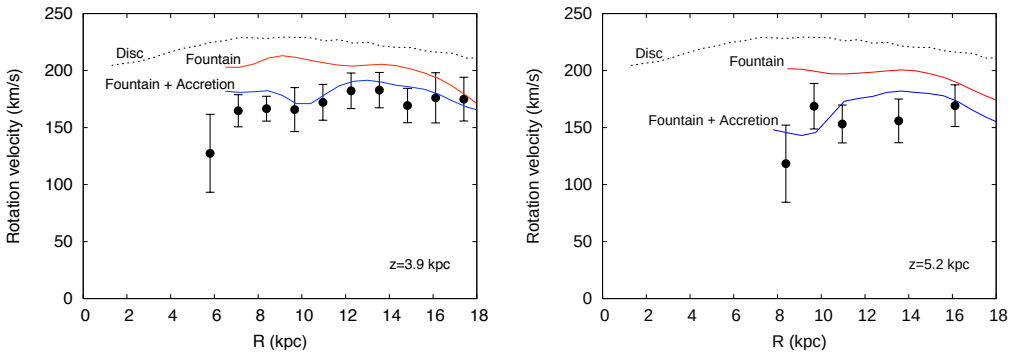

Figure 1.3: H I rotation curves above the plane of NGC 891 (points with error bars) at $z = 3.9\,\mathrm{kpc}$ (left panel) and $z = 5.2\,\mathrm{kpc}$ (right panel). The dashed line in each panel represent the rotation curve of the disc and is shown to make apparent the vertical gradient in the rotational velocity of the gas. The predictions of a ballistic fountain model (red lines) and a fountain model that includes accretion of material from an ambient medium (blue lines) are also shown (from Fraternali & Binney 2008).

cretion of material from an ambient medium (Fraternali & Binney 2008). Accretion of ambient material allows the clouds to lose the excess of angular momentum visible in the galactic fountain, reconciling the values of the rotational velocity with the observed ones. The only free parameter in this model is the accretion rate of the clouds, which Fraternali & Binney (2008) tuned to reproduce the observed H I data-cube of the galaxy. Remarkably, the global estimated accretion rate is very close to the star formation rate of NGC 891. Therefore, accretion driven by galactic fountain clouds seems to be a viable mechanism for star-forming galaxies to get the gas needed to sustain star formation. However, the physical process by which a fountain cloud can accrete ambient material and even the nature of the latter were not addressed by Fraternali & Binney (2008).

In this Thesis we explore the possibility that the ambient medium interacting with the fountain clouds is the coronal gas at virial temperature in which galaxies are embedded (see Section 1.1.3). In particular, Chapters 4 and 5 are devoted to the study of this interaction, which causes mass and momentum to be exchanged by the fountain clouds and the corona, with

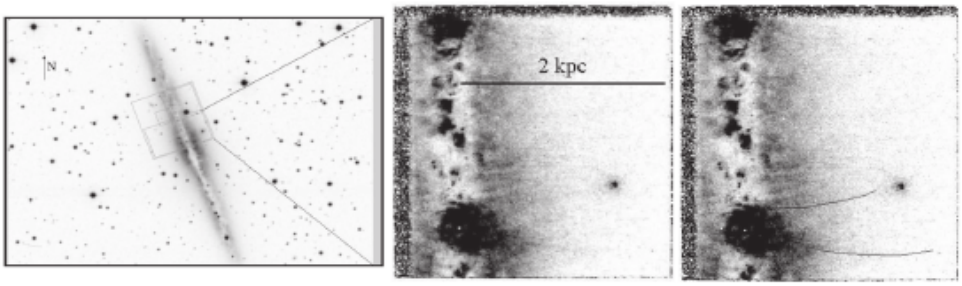

Figure 1.4: Diffuse ionised gas emission in NGC 891. Left panel: DSS image of the galaxy overlaid with the WFPC2 field of view. Central panel: Hα image of the disc-halo region north of the bulge. The emission due to the ionised gas is characterised by the presence of filaments, which reach distances from the mid-plane of $\sim 2\,$kpc. The filaments originate from a supergiant shell region in the disc. Right panel: the same as central panel but with the two most prominent filaments traced in black (from Rossa et al. 2004).

substantial consequences for the dynamics of the halo gas.

1.1.2 Ionised gas

The extra-planar gas has also a ionised warm ($\sim 10^4\,$K) component which is observed in Hα and other optical emission lines. The emission coming from the extra-planar ionised gas is usually concentrated in layers, which are called diffuse ionised gas (DIG) layers. In the Milky-Way the same component is often referred to as the Reynolds' layer (Reynolds 1991). It is not uncommon for these layers to extend up to several kiloparsecs from the disc (Hoopes et al. 1999; Collins et al. 2000). In some cases, as for instance NGC 891, DIG emission presents a filamentary structure (see Figure 1.4). Most of the emission from DIG is associated to regions of active star formation (Rossa & Dettmar 2003) and this clearly points towards an internal origin of the extra-planar ionised gas. There is also a possible correlation between the thickness of the ionised layer and its kinematics with the star formation rate in the galaxy (Heald et al. 2007). As in the case of the neutral phase, the most likely mechanism that produces the ionised component

of the halo gas is the galactic fountain. The source of ionization for this gas is thought to be the radiation flux from the stars in the disc (Reynolds 1990), but more recent studies have pointed out that this source is probably insufficient (Rand et al. 2008). The kinematics of the extra-planar ionised gas is consistent with that of the neutral phase, with a gradient in the rotational velocity which is similar to those observed in H I (e.g. Heald et al. 2006b; Heald et al. 2007). Also in this ionised component non-circular motions have been detected and there are indications of large-scale radial motions towards the centre of the galaxy (Fraternali et al. 2004).

1.1.3 Hot gas

Current cosmological models predict that most of the baryons originally associated with the dark matter halo of galaxies comprise an extensive corona of gas at virial temperature ($\sim 10^6\,\mathrm{K}$) in which galaxies are embedded. These hot atmospheres are a cosmologically significant reservoirs of gas, which, in principle, can be accreted by star-forming galaxies to sustain star formation at the current observed rates (see Section 1.1). Therefore, coronae may play a major role in galaxy evolution by regulating the availability of (cold) gas. A key point is how this gas can cool from the virial temperature down to $\lesssim 10^4\,\mathrm{K}$, so that it can be transferred from these extensive atmospheres to thin discs where stars can form.

Most of the theoretical effort in this field has focussed on the idea of a direct cooling of the corona, in a way akin to a classical cooling flow. In this scenario patches of the corona spontaneously cool due to thermal instability and are then accreted on to the disc. However, investigations by Binney et al. (2009) and Nipoti (2010) have shown that thermal instability in galactic coronae is damped by the combined effect of heat conduction and buoyancy. Recent numerical simulations (Peek et al. 2008; Kaufmann et al. 2009) confirm this analytic expectation. Moreover, even in the most favourable conditions (entropy profile nearly flat), the accretion rate of the coronal gas is only $\approx 0.2{-}0.3\,\mathrm{M}_\odot\,\mathrm{yr}^{-1}$, approximately an order of magnitude

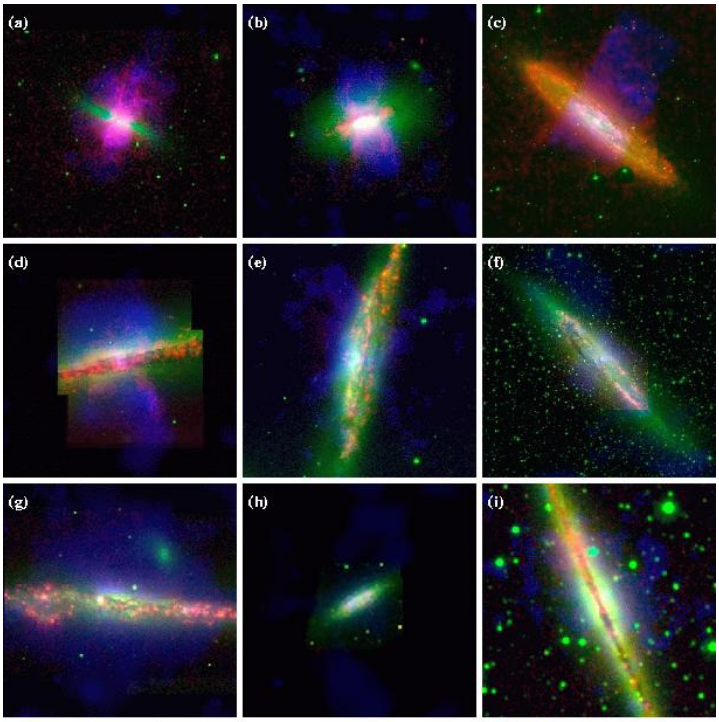

Figure 1.5: A sample of nine galaxies showing soft X-ray emission (blue) indicative of hot gas at $\sim 10^6$ K. The spatial location of the emission is predominantly associated to star-forming regions in the galaxy. Each box has a side of 20 kpc (from Strickland et al. 2004).

less than that required to replace the gas that is consumed by star formation. Interestingly this is also the accretion observed in the Milky-Way from the so-called high-velocity clouds (Wakker et al. 2008) and analogous clouds in external galaxies (Fraternali 2010).

In this Thesis we present an alternative scenario, in which cooling of the hot corona is enhanced by the interaction with the cold disc gas ejected towards the halo by galactic fountains. We will show, with two-dimensional grid hydrodynamical simulations, that this interaction can be a viable mechanism to efficiently cool coronal gas at the rate needed to sustain star formation.

Haloes of hot gas at virial temperature are commonly detected around rich clusters of galaxies through their free-free emission in the X-ray band

(Sarazin 2009). On the other hand, X-ray coronae have so far escaped to direct detection around relatively isolated spiral galaxies (Rasmussen et al. 2009). This implies that these structures must be characterised by a surface brightness that falls below the sensitivity of the current X-ray instrumentation. Therefore, most of the evidence that we have on the existence of a hot medium that surrounds disc galaxies is indirect and comes, for instance, from absorption UV spectroscopy (Sembach et al. 2003), morphology of high- and intermediate-velocity clouds (Brüns et al. 2001; Westmeier et al. 2005), rotation measure of pulsars (Anderson & Bregman 2010) and ram pressure stripping of dwarf galaxies (Grcevich & Putman 2009). From these observations only rough constraints on total mass, X-ray luminosity, density and temperature profiles of galactic coronae can be derived.

On the other hand, extra-planar X-ray emission is observed around spiral galaxies having high star formation activity. In particular, a sample of these galaxies, which has been studied by (Strickland et al. 2004), is presented in Figure 1.5, where the X-ray emission is indicated by the blue regions. From the correlation between the X-ray luminosity and the stellar energy feedback of these galaxies, and from the spatial location of the X-ray emission, on the top of active star forming regions, Strickland et al. (2004) are led to the conclusion that origin of this hot gas is a galactic fountain or a galactic wind. Therefore, the X-ray emitting halo is of galactic origin and it is detected because it emits much more efficiently than a cosmological corona with primordial metal abundances, due to its higher (approximately solar) metallicity. This fountain component must mix with the pre-existing corona enhancing its metallicity up to values that are approximately 0.1 solar (Sembach et al. 2003; Shull et al. 2009).

1.2 This Thesis

This Thesis is a study of the dynamics of hot and cold gas in the halo region of galaxies like the Milky-Way, which can provide fundamental clues

to our understanding of the connection between star-forming galaxies and the intergalactic environment in which they from and evolve.

We first focus, in Chapter 2, on the neutral phase of the extra-planar gas. To reproduce its peculiar kinematics (see Section 1.1.1) we model the neutral phase as a system of cold, non-interacting clouds that obey the stationary Jeans equations. We show that the predictions of the Jeans models are not in agreement with the extra-planar H I kinematics that is observed in nearby spiral galaxies such as NGC 891. This seems to indicate that cold clouds must interact with an ambient medium, which we identify with the virial-temperature cosmological corona that surrounds galaxies like the Milky-Way.

We study this interaction by running a series of hydrodynamical simulations of a cold ($T \sim 10^4\,\mathrm{K}$) cloud travelling through a hot ($T \sim 10^6\,\mathrm{K}$) medium, representing the corona, at different relative velocities. To this purpose a novel hydrodynamical code (ECHO++), based on high-order, shock-capturing algorithms has been implemented (Chapter 3). Chapters 4 and 5 are devoted, respectively, to the exchange of mass and momentum between the two phases as a consequence of their interaction. Finally, in Chapter 6, implications of the results of this Thesis for the evolution of star-forming galaxies and hot cosmological coronae are briefly discussed.

2

Stationary models for the cold extra-planar gas

2.1 Introduction

Sensitive H I observations of several nearby spiral galaxies have revealed cold and massive gaseous haloes that surround the galactic discs. In edge-on galaxies, such as NGC 891 (Oosterloo et al. 2007), this extra-planar gas has been traced up to $10 - 20$ kpc from the plane and its kinematics has been studied in detail. The distinctive feature of the kinematics of the extra-planar gas is its steady decline in the rotational velocity with increasing distances from the mid-plane (vertical gradient). A number of models have been proposed to reproduce this vertical gradient and, among them, an important class is represented by models that try to clarify the global dynamical state of the extra-planar gas under the assumption of stationarity (Benjamin 2002; Barnabè et al. 2006).

In the stationary approach, the extra-planar gas is described as a homogeneous fluid in permanent rotation in which vertical and radial motions of the gas are neglected. Thus, the vertical gravitational field of the galaxy

is balanced only by the pressure gradient of the gas. According to the Poincaré-Wavre theorem (Lebovitz 1967; Tassoul 1978), a vertical gradient in the rotational velocity can be present only if the pressure of the medium is not stratified on its density. Therefore, in fluid homogeneous models the gas distribution in the presence of a vertical rotation gradient is necessarily *baroclinic*[1] (Barnabè et al. 2006; see also Waxman 1978). Although in their study of NGC 891 Barnabè et al. (2006) found that a baroclinic configuration well reproduces the observed rotation curves at different heights above the galactic disc, the temperature predicted for the system is $> 10^5$ K, so that a direct description of the H I extra-planar gas is not possible.

The main aim of the present Chapter is to investigate if and how this "temperature problem" can be solved. To do this we exploit the formal identity between stationary fluid equations, for a gaseous system in permanent rotation, and the stationary Jeans equations, for an axisymmetric system with isotropic velocity dispersion. In practice, the baroclinic configuration is tentatively interpreted as a "gas" of cold H I clouds described by the stationary Jeans equations, where the support against the vertical component of the galaxy's gravitational field is provided by the velocity dispersion of the cold clouds rather than by the thermal pressure. Because of the formal identity between the fluid and Jeans equations, also in this latter case a decrease of rotational velocities with increasing distances from the mid-plane is obtained when the density field is built using the approach described by Barnabè et al. (2006).

The stationary Jeans equations are then used to model the kinematics of the extra-planar gas of the edge-on galaxy NGC 891, which is one of the best studied cases so far. Several Jeans models, both with isotropic and anisotropic velocity dispersion tensors, are investigated and their predictions compared to the available H I observations of that galaxy. The substitution of a fluid system with a collection of clouds poses several is-

[1]Differently from a barotropic fluid, in a baroclinic fluid surfaces of constant density and surfaces of constant pressure are not parallel.

sues from the point of view of the comparison with the observations (see Section 2.3.3). To overcome these problems the approach of Fraternali & Binney (2006, 2008) is followed and an *artificial cube*, with the same resolution and total flux as the *data cube* of the H I observations, is constructed as an output for each model. The comparison with the raw data removes all the intermediate stages of data analysis and their associated uncertainties, assuring, in the meantime, the full control of projection and resolution effects.

The results of this Chapter have been published in paper form in Marinacci et al. (2010b).

2.2 Jeans-based description of fluid baroclinic solutions

To treat the extra-planar gas as a system of cold clouds described by the usual stationary Jeans equations two important conditions must be satisfied: (i) the clouds must move ballistically in the halo region under the influence of the galaxy gravitational field; (ii) the system must be collisionless. However, clouds are embedded in a hot medium, called corona (see Chapter 1), that is about a thousand times less dense than the clouds and provides the pressure required to confine them (Spitzer 1956; Wolfire et al. 1995). The interaction with this hot corona, which takes the form of mass and momentum exchange between the two phases, may have a significant influence on their dynamics (see Chapters 4 and 5). In this Chapter we neglect these effects and we treat the clouds as if they were moving on ballistic trajectories. This assumption is commonly employed in galactic fountain models (e.g. Bregman 1980; Collins et al. 2002) and can be justified in the limit of large cloud masses. Taking as a fiducial value $10^5\,\mathrm{M}_\odot$ for the mass of a typical halo cloud (see Wakker et al. 2008; Thilker et al. 2004), the timescales of the mass and momentum exchange mentioned above are more than 10 times the dynamical time, and it is therefore fair to treat the sys-

tem as subject only to gravitational forces. Moreover, if the H I halo of a galaxy like NGC 891 is made up of clouds with these masses and radii of 100 pc, the collision time between clouds turns out to be about 5 times the dynamical time and the system can be considered roughly collisionless.

2.2.1 Isotropic Jeans solutions

In cylindrical coordinates, consider an axisymmetric density distribution of gas clouds moving under the influence of an axisymmetric galactic gravitational potential $\Phi(R, z)$, so that all the physical quantities are independent of the azimuthal angle φ. The galactic gravitational potential Φ is the sum of the dark-matter halo, the bulge and the stellar and gaseous disc potentials. The contribution to the gravitational field of the extra-planar gas, which represents a very small fraction of the total mass (for instance, less than 1% in NGC 891), is neglected. If the velocity dispersion tensor of the cloud distribution is isotropic, the associated stationary Jeans equations are

$$\begin{cases} \dfrac{1}{\rho}\dfrac{\partial(\rho\sigma_z^2)}{\partial z} = -\dfrac{\partial\Phi}{\partial z}\,, \\ \\ \dfrac{1}{\rho}\dfrac{\partial(\rho\sigma_R^2)}{\partial R} = -\dfrac{\partial\Phi}{\partial R} + \dfrac{\overline{\mathrm{v}_\varphi^2} - \sigma_R^2}{R}\,, \end{cases} \tag{2.1}$$

where ρ is the cloud density distribution, $\sigma_R = \sigma_z = \sigma$ is the one-dimensional velocity dispersion, and v_φ is the velocity of each cloud around the $z-$axis (e.g., Binney & Tremaine 2008). The phase-space average is indicated by a bar over the quantity of interest so $u_\varphi = \overline{\mathrm{v}}_\varphi$, and it is further assumed that $u_R = u_z = 0$, i.e. no net motion in the radial and the vertical directions is considered, as in the homogeneous fluid treatment. Under these assumptions the streaming velocity of the clouds is given by

$$u_\varphi^2 = \overline{\mathrm{v}_\varphi^2} - \sigma^2\,, \tag{2.2}$$

and equations (2.1) are formally identical to the equations describing a stationary fluid in permanent rotation, where the thermodynamic pressure of the fluid is replaced by the quantity $\rho\sigma^2$.

To solve equations (2.1) one fixes the galactic gravitational potential $\Phi(R, z)$ and assumes a cloud density distribution $\rho(R, z)$ consistent with the observations and vanishing at infinity (see Section 2.3). With this procedure, the obtained configuration is in general baroclinic. Therefore, from the first of equations (2.1) with boundary condition $\rho\sigma_z^2 \to 0$ for $z \to \infty$, one obtains

$$\rho\sigma_z^2 = \int_z^\infty \rho \frac{\partial \Phi}{\partial z}\, \mathrm{d}z\,, \tag{2.3}$$

and u_φ is calculated from the second of the equations (2.1) and equation (2.2). Note that the rotational velocity field u_φ can be obtained in general by the "commutator-like" relation

$$\frac{\rho u_\varphi^2}{R} = \int_z^\infty \left(\frac{\partial \rho}{\partial R}\frac{\partial \Phi}{\partial z} - \frac{\partial \rho}{\partial z}\frac{\partial \Phi}{\partial R} \right) \mathrm{d}z\,, \tag{2.4}$$

(e.g., see Barnabè et al. 2006; and references therein).

The expression above reveals that the existence of physically acceptable solutions with $u_\varphi^2 \geq 0$ everywhere is not guaranteed for arbitrary choices of ρ and Φ. In Barnabè et al. (2006) general rules for constructing physically acceptable baroclinic solutions (i.e. with a resulting $u_\varphi^2 \geq 0$ everywhere) are illustrated. For example, in the usual case in which $\partial\Phi/\partial R \geq 0$ and $\partial\Phi/\partial z \geq 0$, a sufficient condition to ensure the positivity of u_φ^2 is that $\partial\rho/\partial z \leq 0$ and $\partial\rho/\partial R \geq 0$. The same rules apply also in the Jeans case, suggesting the use of centrally depressed density distributions. This choice is consistent with the radial H I distribution observed in nearby spiral galaxies such as NGC 891 (Oosterloo et al. 2007).

2.2.2 Anisotropic Jeans solutions

In the present analysis, simple phenomenological models including velocity dispersion anisotropy have been also explored for completeness. This exploration is also necessary because, as it will be shown in Section 2.3, Jeans isotropic models (the natural kinetic counterpart of homogeneous fluid

models) fail to reproduce some features of the extra-planar gas kinematics in NGC 891.

Given the gravitational potential Φ and the cloud density distribution ρ, the solution of the stationary axisymmetric Jeans equations with an anisotropic velocity dispersion tensor is unique if one assigns the orientation and the shape of the intersection of the velocity dispersion ellipsoid everywhere in the meridional plane. For the problem considered here, this is done by maintaining $u_R = u_z = 0$ and assuming a suitable parametrization for the ratio σ_R/σ_z. The simplest choice is that of a constant anisotropy which, following Cappellari (2008), can expressed as $\sigma_R^2 = b\sigma_z^2$ with $b \geq 0$[2]. Thus, equations (2.1) become

$$\begin{cases} \dfrac{1}{\rho}\dfrac{\partial \rho\sigma_z^2}{\partial z} = -\dfrac{\partial \Phi}{\partial z}\,, \\ \\ \dfrac{b}{\rho}\dfrac{\partial \rho\sigma_z^2}{\partial R} = -\dfrac{\partial \Phi}{\partial R} + \dfrac{\overline{\mathrm{v}_\varphi^2} - b\sigma_z^2}{R}\,. \end{cases} \tag{2.5}$$

Thus σ_z^2 is given by equation (2.3) as in the isotropic case, whilst it can be shown that now

$$\begin{aligned} \frac{\rho(\overline{\mathrm{v}_\varphi^2} - b\sigma_z^2)}{R} = \\ b\int_z^\infty \left(\frac{\partial \rho}{\partial R}\frac{\partial \Phi}{\partial z} - \frac{\partial \rho}{\partial z}\frac{\partial \Phi}{\partial R}\right)\,\mathrm{d}z \,+ (1-b)\,\rho\frac{\partial \Phi}{\partial R}\,. \end{aligned} \tag{2.6}$$

Equation (2.6) can be rewritten in a more compact form as

$$\overline{\mathrm{v}_\varphi^2} - b\sigma_z^2 = bu_{\varphi,\mathrm{iso}}^2 + (1-b)\,u_\mathrm{c}^2\,, \tag{2.7}$$

where $u_{\varphi,\mathrm{iso}}$ is the rotational velocity field of the corresponding isotropic model (obtained with $b = 1$) and

$$u_\mathrm{c}^2 \equiv R\,\frac{\partial \Phi}{\partial R} \tag{2.8}$$

[2]Note that this anisotropy cannot be realised under the common assumption of a two-integral distribution function depending on energy and angular momentum along the $z-$axis, as in this case necessarily $\sigma_R = \sigma_z$ (i.e. $b = 1$).

is the circular velocity at position (R, z). The streaming velocity field is then obtained by splitting $\overline{\mathrm{v}_\varphi^2}$ into the streaming motion u_φ^2 and the azimuthal velocity dispersion σ_φ^2. Following the standard Satoh (1980) k-decomposition one has

$$u_\varphi^2 = k^2(\overline{\mathrm{v}_\varphi^2} - b\sigma_z^2)\,, \tag{2.9}$$

so that

$$\sigma_\varphi^2 = b\sigma_z^2 + (1-k^2)\,(\overline{\mathrm{v}_\varphi^2} - b\sigma_z^2)\,, \tag{2.10}$$

with $0 \leq k \leq 1$; in general k can be function of the position, i.e. $k = k(R, z)$ (e.g., see Ciotti & Pellegrini 1996). For $k = 0$ no ordered motions are present, whilst $\sigma_\varphi^2 = \sigma_R^2$ in the case $k = 1$; the isotropic case is recovered for $k = b = 1$. From equation (2.9) it follows that the Satoh decomposition procedure can be applied only when $\overline{\mathrm{v}_\varphi^2} - b\sigma_z^2 \geq 0$, so k and b are not independent. Note that if the corresponding isotropic model leads to a physically acceptable solution, then a sufficient condition to ensure the positivity of u_φ^2 is $b \leq 1$: if $u_{\varphi,\mathrm{iso}}^2 \geq 0$, the left-hand-side of equation (2.7) can be negative only if $b > 1$, so the use of the Satoh decomposition is consistent with the assumption $\sigma_R \leq \sigma_z$. This requirement is in agreement with the observations that show large vertical motions of the order of $50 - 100\,\mathrm{km\,s^{-1}}$ and velocity dispersion along R and φ of the extra-planar gas of approximately $20\,\mathrm{km\,s^{-1}}$ (Boomsma et al. 2008; Oosterloo et al. 2007). Summarizing, this simple parametrization of the velocity dispersion anisotropy is consistent with physically acceptable solutions provided that: (i) $0 < b \leq 1$ and (ii) the corresponding isotropic model has $u_\varphi^2 \geq 0$ everywhere.

2.2.3 Conditions to have negative vertical gradients

The most important kinematic property of the extra-planar gas is its steady decrease of the rotational velocity with increasing distance from the galactic plane, at fixed galactocentric radius R. To study the kinematics of the extra-planar gas in the models it is helpful to have general expressions

(such as equation [2] of Waxman 1978) relating the vertical gradient of the rotational velocity to other physical quantities in stationary configurations.

For example, in the isotropic case, if equation (2.4) is differentiated with respect to z, one obtains

$$\frac{\partial u_\varphi^2}{\partial z} = \frac{\partial \ln \rho}{\partial z}\left(u_\mathrm{c}^2 - u_\varphi^2\right) - \frac{\partial \ln \rho}{\partial \ln R}\frac{\partial \Phi}{\partial z}\,. \tag{2.11}$$

Thus, the necessary and sufficient condition to have a decrease in the rotational velocity is the negativity of the right hand side of equation (2.11). Of a particular interest is the case of a typical gravitational potential such that $\partial\Phi/\partial z \geq 0$ and a centrally depressed density distribution vanishing for $R \to \infty$ with $\partial\rho/\partial z \leq 0$. For each value of z there is a radius R_max such that ρ increases with R for $R < R_\mathrm{max}$ and then decreases with R for $R \geq R_\mathrm{max}$. From equation (2.11) it follows that for $R \geq R_\mathrm{max}$ a necessary condition for a solution to exhibit a negative vertical gradient in the rotational velocity is $u_\varphi^2 \leq u_\mathrm{c}^2$.

For systems with anisotropic velocity dispersion tensor of the class here considered, there is not a simple expression for the vertical gradient of the rotational velocity, unless k is independent of z. In this case, a useful expression for the vertical gradient of the rotational velocity can be obtained by substituting equation (2.9) into equation (2.7) and by differentiating the result with respect to z. This leads to

$$\frac{\partial\, u_\varphi^2}{\partial z} = k^2\left[b\frac{\partial\, u_{\varphi,\mathrm{iso}}^2}{\partial z} + (1-b)\frac{\partial\, u_\mathrm{c}^2}{\partial z}\right]\,, \tag{2.12}$$

where $u_{\varphi,\mathrm{iso}}$ is the rotational velocity of the corresponding isotropic model. It follows that in the usual cases, in which $\partial u_\mathrm{c}^2/\partial z \leq 0$ and $b < 1$ (see Section 2.2.2), a negative vertical velocity gradient in the corresponding isotropic model is a sufficient condition to have $\partial u_\varphi/\partial z \leq 0$ also in the anisotropic models of the family considered here.

2.3 Application to NGC 891

The general rules of Section 2.2 are now applied to the specific case of the extra-planar gas of NGC 891, to explore whether the proposed models reproduce the observed decrease of the rotational velocity for increasing z. The resulting models can directly describe the extra-planar H I gas seen in the observations because the vertical "pressure" support, needed against the galaxy gravitational field, is now provided by the velocity dispersion of the clouds, rather than by the thermodynamic temperature as in the homogeneous baroclinic models of Barnabè et al. (2006). The present investigation differs from that of Barnabè et al. (2006) in three main aspects: (i) the density distribution for the extra-planar gas was directly derived from the observations, and not just guessed, (ii) the comparison with the H I data was substantially improved by constructing an artificial cube for each model with the same resolution and total flux as the observations, (iii) the mass model of the galaxy was tailored on the most recent observational constraints (see next Section).

2.3.1 The galaxy model

For the determination of the gravitational potential of NGC 891, we fitted the H I rotation curve of the galaxy, obtained by Fraternali et al. (2005) with an envelope tracing technique (see Section 2.3.3), with a maximum-disc mass model. This mass model consists of four distinct components: two exponential discs (stellar and gaseous), a bulge and a dark-matter halo. The volume density of the two disc components is given by

$$\rho(R,z) = \rho_0 \mathrm{e}^{-R/R_\mathrm{d}}\, \zeta\left(\frac{z}{h_\mathrm{d}}\right) , \tag{2.13}$$

where ρ_0 is the central density, $\zeta(z/h_\mathrm{d})$ is the vertical density distribution, either an exponential or a sech^2 law, and the dimensional constants R_d and h_d are, respectively, the scale-length and the scale-height of the disc. The bulge and the dark halo components are modelled using the double

Component	Parameter	Value
Stellar disc	ρ_0 ($\mathrm{M}_\odot\,\mathrm{kpc}^{-3}$)	6.76×10^8
	R_d (kpc)	4.4
	h_d (kpc)	1.05
	ζ	sech^2
Gaseous disc	ρ_0 ($\mathrm{M}_\odot\,\mathrm{kpc}^{-3}$)	3.1×10^8
	R_d (kpc)	5.7
	h_d (kpc)	0.3
	ζ	exp
Bulge	ρ_0 ($\mathrm{M}_\odot\,\mathrm{kpc}^{-3}$)	9.6×10^6
	a (kpc)	10.8
	α	2
	β	5
	e	0.8
DM halo	ρ_0 ($\mathrm{M}_\odot\,\mathrm{kpc}^{-3}$)	3.0×10^7
	a (kpc)	4.0
	α	0
	β	2
	e	0

Table 2.1: Parameters of the maximum disc model used to fit the rotation curve of NGC 891 (see Figure 2.1).

power-law spheroidal density profile (Dehnen & Binney 1998)

$$\rho(m) = \frac{\rho_0}{(m/a)^\alpha\,(1+m/a)^{\beta-\alpha}}\,, \tag{2.14}$$

where

$$m^2 = R^2 + \frac{z^2}{1-e^2}\,, \tag{2.15}$$

e is the eccentricity of the spheroid, α and β are the inner and outer slopes, and a is the scale-length. The adopted values of the parameters to reproduce the rotation curve in the plane of NGC 891 are reported in Table 2.1. Figure 2.1 shows the results of the fit. Note that in the inner regions of the galaxy ($R < 2\,\mathrm{kpc}$) the rotational velocity rises quite steeply. This can be an indication of a fast rotating inner ring or of a presence of an inner bar, which induces non-circular motions in the gas (Garcia-Burillo &

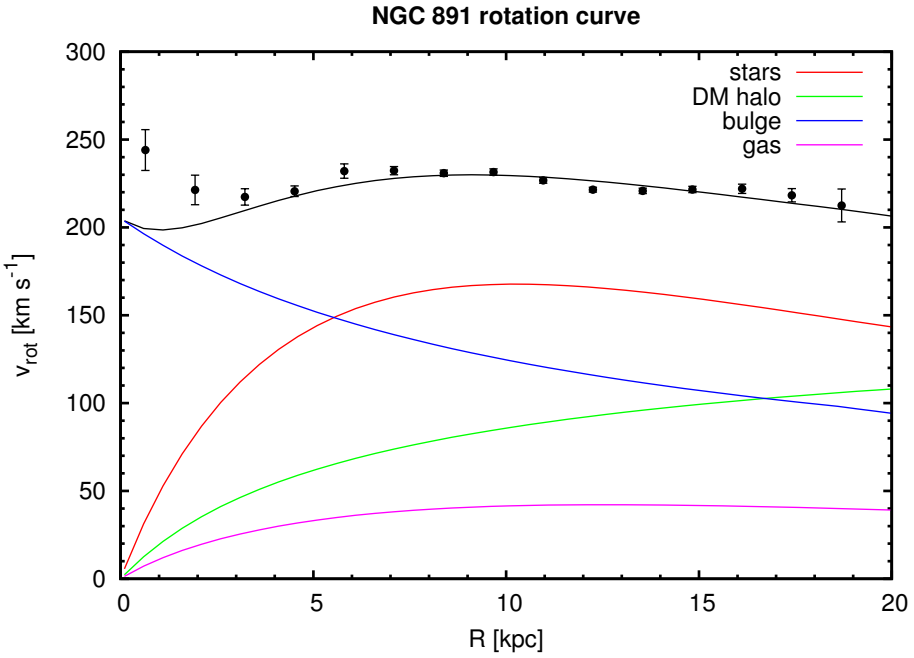

Figure 2.1: Fit of the H I rotation curve of NGC 891 (point with error bars) obtained with the maximum disc model of Table 2.1. The two innermost points of the rotation curve have not been considered in the fit because the gas motion in the inner regions of the galaxy may be dominated by non-circular motions.

Guelin 1995). Because of these uncertainties in the interpretation of the gas motion in the inner regions of the galaxy, the two innermost points of the rotation curve are not included in the fit. The adopted mass decomposition is similar to that in Fraternali & Binney (2006) where other mass models compatible with the rotation curve of NGC 891 are also discussed.

2.3.2 The cloud distribution

A proper Jeans-based analysis of baroclinic fluid solutions requires the choice of a cloud density distribution similar to that observed. For the cloud density distribution the following function is adopted

$$\rho(R,z) = \rho_0 \left(1 + \frac{R}{R_\mathrm{g}}\right)^{\gamma} \mathrm{e}^{-R/R_\mathrm{g}} \,\mathrm{sech}^2\left(\frac{z}{h_\mathrm{g}}\right) , \qquad (2.16)$$

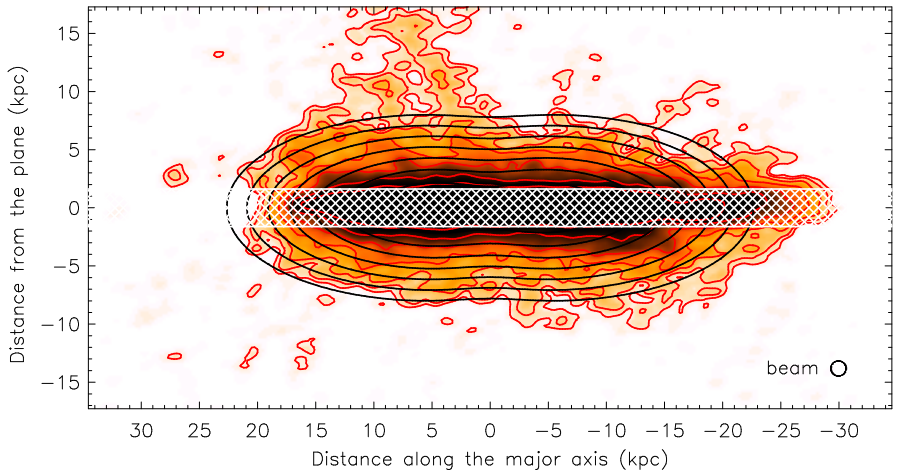

Figure 2.2: Total H I emission map of NGC 891 as obtained by the observations (red contours and colour scale) and by the cloud density distribution of Section 2.3.2 (black contours). The map has a spatial resolution of 25" ($\sim 1.2\,$kpc) with contour levels, starting from the outermost, of 0.15, 0.3, 0.6, 1.2, 2.4, 4.8, 9.6 $\times 10^{20}\,\mathrm{cm}^{-2}$. The shaded area delimits the emission expected from the disc.

which is similar to that used by Oosterloo et al. (2007). In the equation above ρ_0 is the central density, $\gamma \geq 0$, R_g is the scale-length and the scale-height h_g depends upon R as

$$h_\mathrm{g}(R) = h_0 + \left(\frac{R}{h_R}\right)^{\delta}, \quad \delta \geq 0, \tag{2.17}$$

i.e. the density distribution is flared. The parameters of the distribution, excluded the central density ρ_0, are chosen is such a way that the function reproduces the H I total map shown in Figure 2.2 and their values are: $R_\mathrm{g} = 1.61\,$kpc, $\gamma = 4.87$, $h_0 = 2.3\,$kpc , $\delta = 2.25$ and $h_R = 18.03\,$kpc. The central density $\rho_0 = 6.63 \times 10^{-4}\mathrm{cm}^{-3}$ is such that the total mass of the cloud system is that derived by the total H I emission; the corresponding halo mass (i.e. the mass computed for $|z| \geq 1\,$kpc) of $1.13 \times 10^9\,\mathrm{M}_\odot$ is consistent with the value given in Oosterloo et al. (2007). Examples of radial density profiles obtained by equation (2.16) for three different distances from the

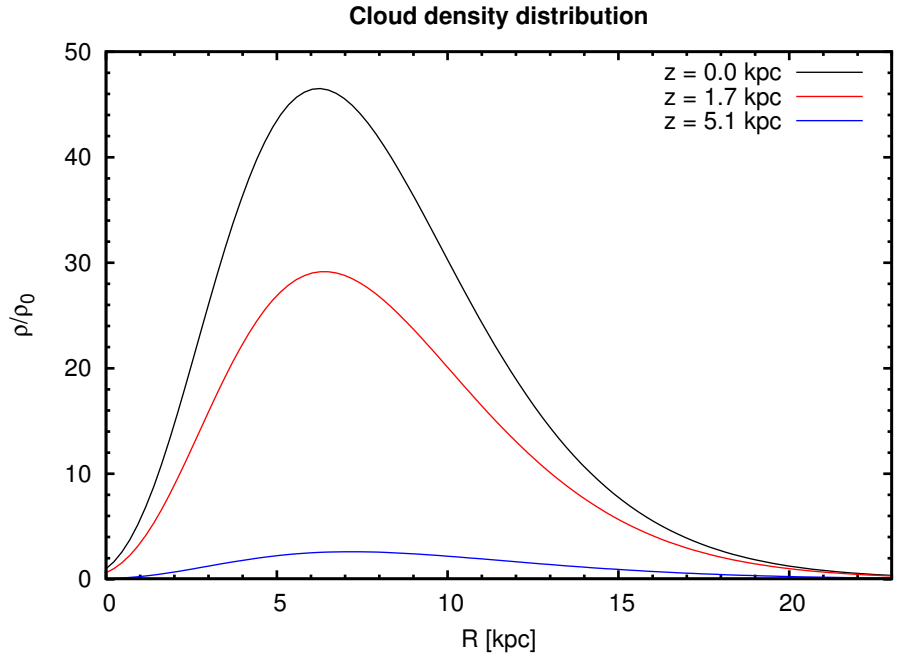

Figure 2.3: Radial profiles of the cloud density distribution (2.16) at three different heights above the mid-plane.

mid-plane are given in Figure 2.3

It can be easily shown that $\partial\rho/\partial z \leq 0$ for the density distribution (2.16), whilst, as it is apparent in Figure 2.3, the radial density profile presents for each z a maximum at some value $R_{\max}(z)$: the positivity of u_φ^2 is then guaranteed in the region $R \leq R_{\max}$, where $\partial\rho/\partial R > 0$, whilst it has to be investigated in the external region, where $\partial\rho/\partial R < 0$, by numerical inspection (see Section 2.2.1). We found that, with the adopted parameters, the density distribution (2.16) produces physically acceptable solutions for all the models considered. For what concerns the vertical velocity gradient, the considerations made in Section 2.2.3 are valid: in particular, it is expected that the rotational velocities of the models are lower than the circular velocity (2.8) for $R \geq R_{\max}$, if the vertical velocity gradient is negative.

The present models aim to reproduce the extra-planar gas and, there-

fore, the region where emission from the disc is expected is neglected. Such a region is covered by shaded areas in all the figures where the comparison with the data is shown (Figures 2.2, 2.5, 2.7, and 2.8). The size of this region ($|z| < 1.64\,\mathrm{kpc}$), is calculated as $\pm 3\sigma \times$ (spatial resolution of the data) assuming that the galactic disc is perfectly co-planar. In fact the resolution of the observations (HPBW= 0.64 kpc) is much larger than the expected intrinsic scale height of the H I disc ($100 - 200\,\mathrm{pc}$), i.e. the disc is not resolved. The exclusion of the disc is necessary to avoid the complication of a region where the gas is almost certainly not described by the considered Jeans equations. It is therefore assumed that, in a real galaxy, at the lower halo boundaries the velocity dispersion, induced by some (unspecified) physical process in the disc, is the same as the one provided by the density distribution (2.16). This requirement is necessary for the system to be stationary.

2.3.3 Construction of the model

Having fixed the galaxy gravitational field and the cloud density distribution, σ_z is computed for each model by integrating numerically equation (2.3) with a finite difference scheme. In the isotropic case, the rotational field is obtained from equation (2.4) using the same numerical scheme. In the anisotropic cases equation (2.7) is used. The rotation velocity and the azimuthal component of the velocity dispersion are then evaluated on the numerical grid by means of equations (2.9) and (2.10).

As an output for the models an artificial cube, with the same spectral and spatial resolutions and total flux as the data cube of H I observations, is generated by the following procedure. In each grid point the cloud density, the rotational velocity and the velocity dispersion are projected numerically along the line-of-sight for the inclination of the galaxy, which is assumed to be seen exactly edge-on. From the projected velocity a first version of the cube is constructed and, to account for the effect of the velocity dispersion, the projected density in each cell of this cube is convolved with a normalised

Gaussian profile with a dispersion equal to the velocity dispersion along the line-of-sight. Finally, the cube is smoothed to the same spatial resolution as the data ($FPBW = 28'' \approx 1.3\,\mathrm{kpc}$).

The construction of an artificial data cube is crucial in the present investigation because it bypasses all the intermediate stages of data analysis, and the assumptions made in these stages. A critical case is the comparison of the data rotation curves with the rotational velocities predicted by the models. The rotation curves of the extra-planar gas (and of edge-on galaxies in general), are usually derived by using fixing the so-called envelope tracing method (see Sancisi & Allen 1979; Fraternali et al. 2005). This method requires the determination, at each position, of the terminal velocity of the gas v_{term}, i.e. the maximum value of the velocity along the line-of-sight. In a edge-on galaxy the terminal velocity is a first approximation of the rotational velocity v_{rot} of the gas, if its motion is dominated by the rotation. What it is done in practice to estimate v_{rot} is to correct the terminal velocity for the observational error σ_{obs} and the random velocities of the H I clouds σ_{ran} as

$$v_{\mathrm{rot}} = v_{\mathrm{term}} - \sqrt{\sigma^2_{\mathrm{obs}} + \sigma^2_{\mathrm{ran}}} \tag{2.18}$$

(see Fraternali & Binney 2008). Clearly, if a model has velocity dispersions inconsistent with that adopted to derive the rotation curves from the data (as it happens here, see Section 2.4), the simple comparison of the two curves is meaningless (see Section 2.5).

2.4 Results

2.4.1 Isotropic model

In this Section, the main features of the isotropic model, i.e. the analogue of a stationary baroclinic fluid model where the thermal pressure of the gas is replaced by a globally isotropic velocity dispersion tensor, are described. Due to this analogy, it is expected that the behaviour of the isotropic model

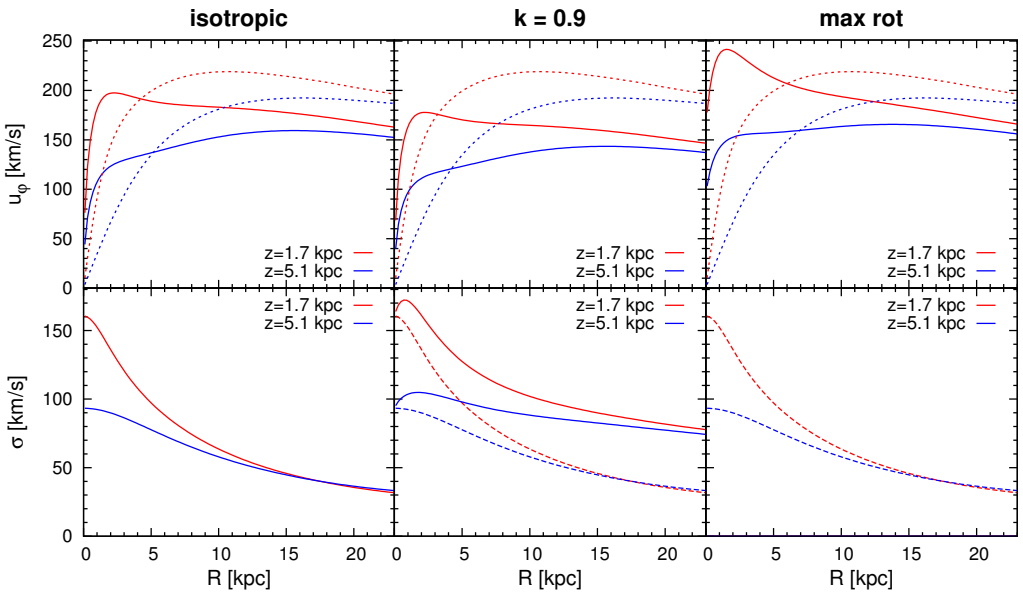

Figure 2.4: Intrinsic rotational velocities and velocity dispersion for system of clouds that can be described by a classical two-integral phase-space distribution function ($b = 1$), at $z = 1.7\,\mathrm{kpc}$ and $z = 5.1\,\mathrm{kpc}$. From left to right: isotropic model ($k = 1$), anisotropic model obtained by using the standard Satoh decomposition with $k = 0.9$ and maximally rotating model [$k = k_{\max}(R, z) > 1$, $\sigma_\varphi = 0$]. Velocity panels: the dotted lines represent the circular velocity u_c whilst the solid lines are the model rotational velocities u_φ. Dispersion panels: the dashed lines indicate σ_z and the solid lines σ_φ. In the isotropic case all the components of the dispersion are the same, whilst in the other two models $\sigma_z = \sigma_R$.

is similar to the baroclinic solutions of Barnabè et al. (2006). However, there is an important difference between these two models in the choice of the density distribution. In the isotropic Jeans model the density is chosen to match the observed H I emission (see Figure 2.2), whilst the density distribution of Barnabè et al. (2006) was just chosen to satisfy the general rules that guarantee a physically acceptable rotational velocity field (i.e. $u_\varphi^2 \geq 0$). The adoption of a cloud distribution derived from the H I observations results in values for $\sigma_z = \sigma_R = \sigma_\varphi$ ranging from 160 (in the centre) to $35\,\mathrm{km\,s^{-1}}$ (at $R \sim 20\,\mathrm{kpc}$) with mean values between 50 and $100\,\mathrm{km\,s^{-1}}$ (Figure 2.4, bottom left panel).

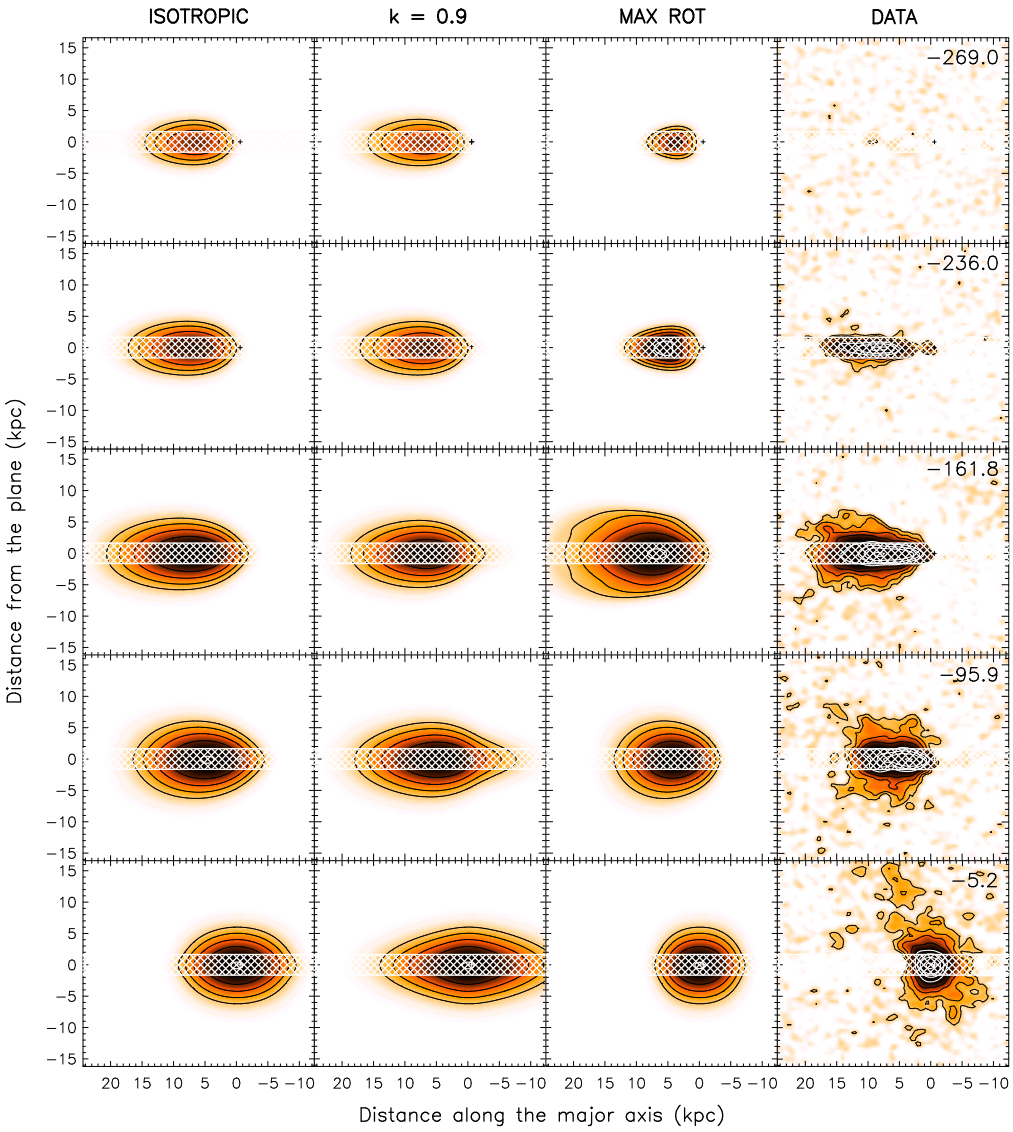

Figure 2.5: Comparison of representative velocity channels of the H I data cube of NGC 891 and the predictions of 3 stationary models with $b = 1$ (thus described by a two-integral phase-space distribution function). From left to right: isotropic ($k = 1$) model, anisotropic model obtained by the standard Satoh decomposition with $k = 0.9$ and maximally rotating [$k = k_{\max}(R, z) > 1$, $\sigma_\varphi = 0$] model. The shaded area in each channel delimits the emission expected from the disc. The contour levels, starting from the outermost, are 0.25, 0.5, 1, 2, 5, 10, 20, 50 mJy/beam; the beam size is 28" = 1.3 kpc.

In the left panels of Figure 2.4 the rotation curves (top) and the radial velocity dispersion profiles (bottom) are presented at distances from the plane $z = 1.7\,\mathrm{kpc}$ (lower halo boundary) and $z = 5.1\,\mathrm{kpc}$; the dashed lines show the circular velocities u_c. As expected from the considerations of Section 2.2.3, in the external regions of the galaxy the rotational velocity is below the circular velocity because of the negative vertical gradient in u_φ. The radial profile of the velocity dispersion shows a monotonic decrease with R but the values of the dispersion are everywhere greater than the mean observed value of $\sim 20\,\mathrm{km\,s^{-1}}$.

Figure 2.5 (first column from the left) shows the artificial cube constructed from this Jeans model, whilst each panel in the rightmost column represents the observed emission of H I gas in a particular velocity channel. The numbers on the top right corners of the data column represent the deviations of the line-of-sight velocities from the systemic one ($528\,\mathrm{km\,s^{-1}}$, Oosterloo et al. 2007) whilst the shaded area on each map delimits the emission expected from the disc ($\pm 3\sigma$ spatial resolution), that this model is not attempting to reproduce. The observed H I emission at higher rotational velocity (corresponding to the channel at $v_\mathrm{los} = -236.0\,\mathrm{km\,s^{-1}}$) is fully due to the mid-plane, i.e. the halo is not visible. This is not surprising because the halo gas rotates more slowly than the gas in the disc and in fact, at lower rotational velocities (channels in the bottom panels), the halo emission becomes important. Due to its high velocity dispersion, in the isotropic Jeans model some emission in the halo region is present also in the upper two velocity channels; only in the middle channel the agreement is good whilst in the bottom channels the emission is too horizontally elongated.

Summarizing, it is possible to construct an isotropic Jeans model with a realistic halo density distribution, in which a negative vertical gradient in the rotational velocity is present. However, the predicted velocity dispersions along the line-of-sight are much higher than those observed, so that a number of features of the data cube are not reproduced. In order to solve these problems, in the next Section different models with anisotropic

velocity dispersion tensors are considered.

2.4.2 Anisotropic models

The assumption of anisotropy in the velocity dispersion can overcome, at least in principle, the problems originated by the high values of σ obtained in the isotropic model. We investigate both the classical Satoh decomposition in a two-integral distribution function (i.e., $\sigma_R = \sigma_z$ everywhere) and the case of a three-integral phase-space distribution function. In the following, $\sigma_{\rm los}$ indicates the component of the velocity dispersion along the line-of-sight on each place in the galaxy.

Two-integral anisotropic systems

These systems are described by a two-integral phase-space distribution function, for which $\sigma_z = \sigma_R$. The relevant equations are obtained by taking $b = 1$ in equations (2.5), and adopting a Satoh decomposition in the azimuthal direction. When $k = 0$ σ_φ^2 is maximal, while when $k = 1$ the system is isotropic. Allowing for $k = k(R, z)$, more rotationally supported models can be constructed, up to the maximally rotating one where $\sigma_\varphi^2 = 0$ (Ciotti & Pellegrini 1996). First of all, a model with constant k, fixed to 0.9, is investigated; for lower values the disagreement with the data increases. It is expected that the model is not better than the isotropic ($k = 1$) case in reproducing the observations, because $\sigma_{\rm los}$ is increased by the adopted anisotropy, i.e. $\sigma_\varphi \geq \sigma_z = \sigma_R$, as can be inferred from equation (2.10). The central column of Figure 2.4 (bottom panel) clearly illustrates this fact, showing a difference among σ_φ and the other two components of approximately $30\,{\rm km\,s^{-1}}$, on average. For what concerns the properties of the rotation curves, the considerations carried out in the isotropic case are still valid, because from equations (2.7) and (2.9) it follows that $u_\varphi = k\, u_{\varphi,{\rm iso}}$ so that in the external regions of the galaxy $u_\varphi < u_{\rm c}$. The artificial cube of this model presented in Figure 2.5 (second column) shows that in the channels close to the systemic velocity (bottom) the emission is even more

elongated than in the isotropic model, in complete disagreement with the data.

In two-integral systems, the line-of-sight velocity dispersion can be reduced only if $k > 1$. As a limit case, the results for the maximally rotating model, in which $k = k_{\max}(R, z) \geq 1$ such that the rotational velocity has its maximum value everywhere and $\sigma_\varphi = 0$, are presented. The corresponding intrinsic rotation curves are shown in Figure 2.4 (top right panel) and their peculiarity is the steep rise in the central regions. The reduced value of $\sigma_{\rm los}$ improves the agreement with the data, as it can be seen from the artificial data cube of the model in Figure 2.5, especially in the channels near the systemic velocity. This agreement is not so good in the channel at $v_{\rm los} = -236.0\,{\rm km\,s^{-1}}$ and in general in all the channels between $-236.0\,{\rm km\,s^{-1}}$ and $-161.8\,{\rm km\,s^{-1}}$ (not shown here) where, due to the steep rise in the rotational velocity at small R, there is emission in the central halo regions that is not present in the data.

Three-integral anisotropic systems

In this Section, anisotropic Jeans models with $b \leq 1$ (see again equations [2.5]), and thus supported by a three-integral phase-space distribution function, are discussed, starting from the case $\sigma_R = \sigma_\varphi$ (i.e. $k = 1$). The best fit to the data is obtained by an anisotropic model with $b \sim 0.1$, which limits the line-of-sight velocity dispersion to about $20\,{\rm km\,s^{-1}}$ for a large interval of R (Figure 2.6, bottom left panel). The rotation curves for this model (top left panel) are very similar to the circular velocity curves, in accordance with equation (2.7) which states that, in the limiting case $b = 0$, the curves coincide. The artificial data cube of the model is presented in Figure 2.7 (leftmost column). In the high velocity channels (top panels) the halo emission is still present but, at variance with the isotropic case, this is due to the fact that the rotational velocities of the model are slightly higher than those observed. In the low velocity channels (bottom panels) the halo emission is narrower than the data along the horizontal axis, due to a rapid

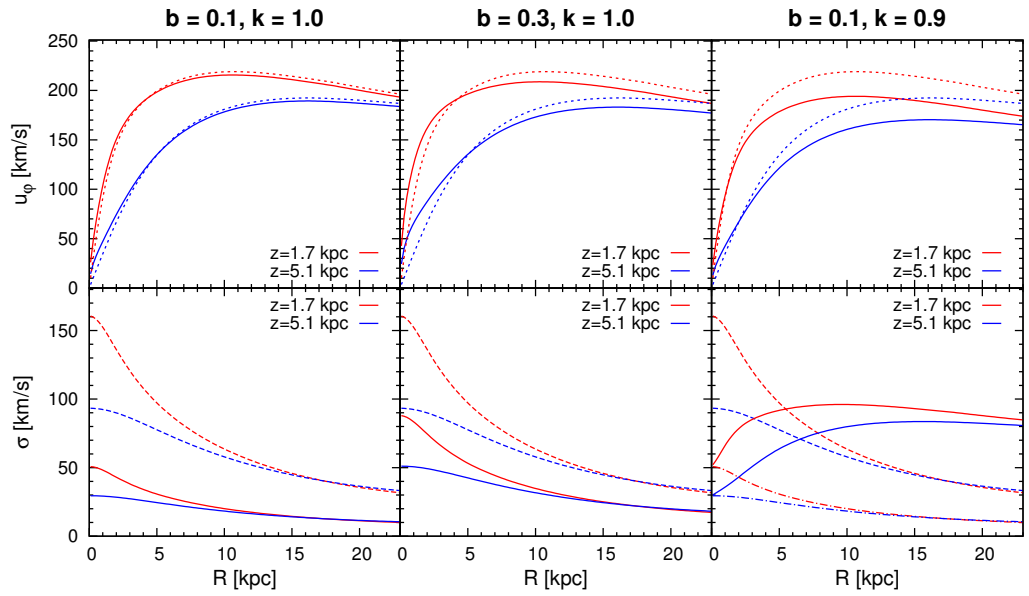

Figure 2.6: Intrinsic rotational velocities and velocity dispersion for anisotropic Jeans models described by a three-integral phase-space distribution function ($b < 1$), at $z = 1.7$ kpc and $z = 5.1$ kpc. From left to right: $b = 0.1$ and $k = 1$ model, $b = 0.3$ and $k = 1$ model and $b = 0.1$ and $k = 0.9$ model. Rotational velocity panels: the dotted lines represent the circular velocity u_c whilst the solid lines are the rotational velocities u_φ. Dispersion panels: the dashed lines indicate σ_z, the solid lines σ_φ and the dashed-dotted lines σ_R; in the first two cases $\sigma_\varphi = \sigma_R$.

decrease of the velocity dispersion in the outer parts. These discrepancies will be considered in more detail in Section 2.5.

An important issue regarding the anisotropic models is the effect that the choice of the parameters b and k may have on the properties of the solutions. This aspect is analysed by fixing the value of one of the two parameters and by varying the other. The results of this comparison, for representative values of b and k, are shown in Figure 2.6, where the model with $b = 0.1$ and $k = 1$ (which, hereafter, is also referred to as the "high-σ_z model") has been taken as a reference case. In particular, increasing the value of b at fixed k has the net result of increasing the line-of-sight velocity dispersion (i.e. σ_R and σ_φ) whilst the rotational velocity is decreased;

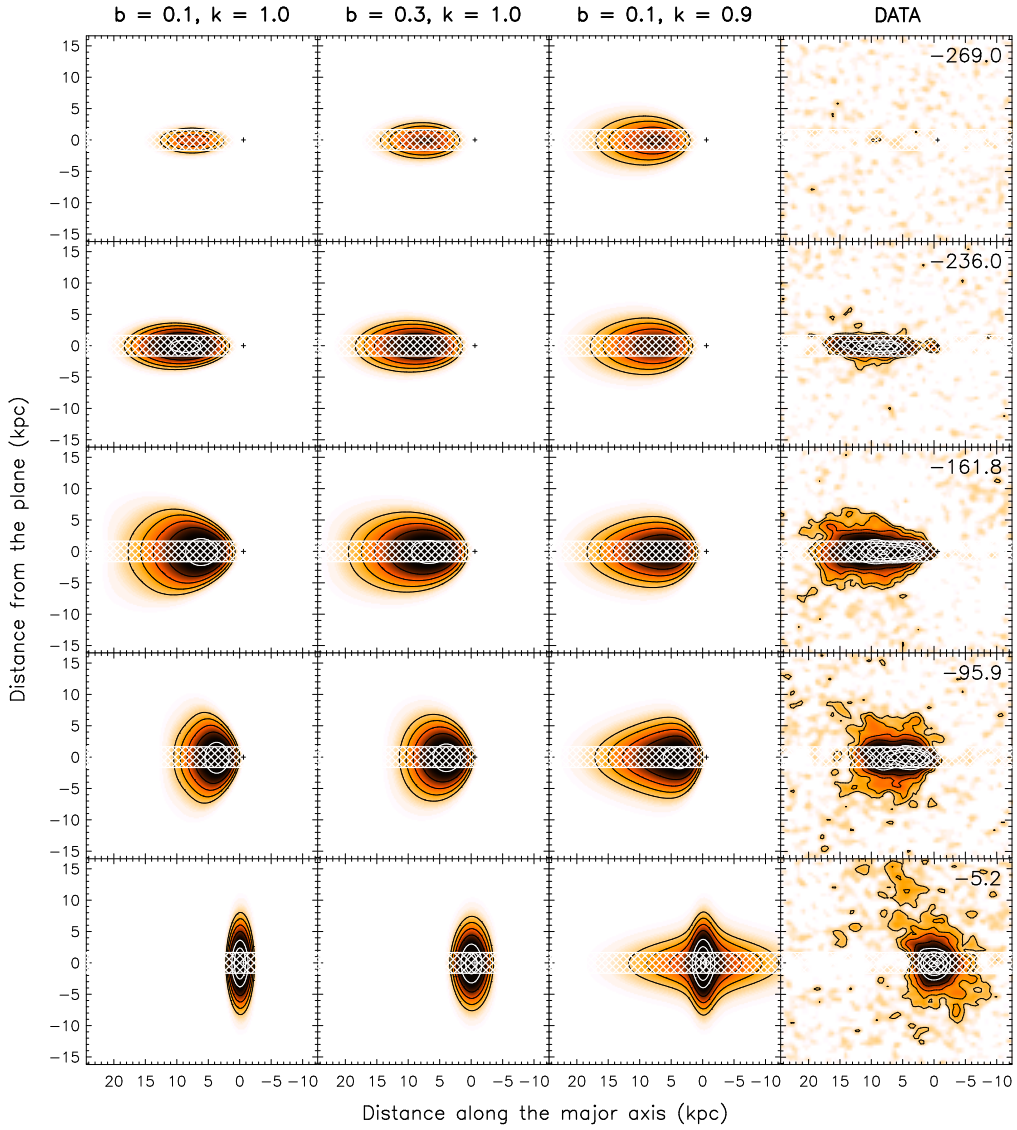

Figure 2.7: Comparison of five representative velocity channels of the H I data cube of NGC 891 and the predictions of 3 anisotropic models described by a three-integral phase-space distribution function: $b = 0.1$ and $k = 1$ (first column), $b = 0.3$ and $k = 1$ (second column), $b = 0.1$ and $k = 0.9$ (third column). The shaded area in each channel delimits the emission expected from the disc. The contour levels, starting from the outermost, are 0.25, 0.5, 1, 2, 5, 10, 20, 50 mJy/beam; the beam size is 28" = 1.3 kpc.

the decrease in rotational velocity is also obtained when the value of k is decreased at fixed b, but in this case only the value of σ_φ is affected. In Figure 2.7 the artificial cubes of the models just described are presented. The emission of the reference model ($b = 0.1$, $k = 1$) in all the velocity channels is less horizontally extended than that of the model with $b = 0.3$, due to the smaller values of $\sigma_{\rm los}$. Although the $b = 0.3$ model seems to agree better with the data in the channel maps close to systemic velocity, the top panels of Figure 2.7 show substantial halo emission, due to the now increased line-of-sight velocity dispersion. The interpretation of the differences between the reference model and the model with $k \neq 1$ (third column) is complicated by the fact that $\sigma_\varphi \neq \sigma_R$ so that the extension of the emission strongly depends on their relative contribution to the velocity dispersion along the line-of-sight. In particular, the importance of σ_φ is maximum in the high velocity channels (top panels), and then it progressively diminishes in the channels near the systemic velocity in favour of σ_R.

In short, three-integral models with $b < 1$ and $k = 1$ perform better than the isotropic and the two-integral models because $\sigma_{\rm los}$ can be reduced to values comparable to the the observed one. However, a number of features of the data cubes are still not reproduced revealing intrinsic problems with all these stationary models that are discussed in the next Sections.

2.4.3 Position-velocity plots

Among the models presented above the three most representative are selected and further compared with the H I data. Figure 2.8 shows two cuts of data cube of NGC 891 (rightmost column) taken perpendicularly to the plane of the galaxy at $R = 7.5\,$kpc (first row) and $R = 2.8\,$kpc (third row) from the centre towards North-East. These plots are analogous to those shown in Figure 16 of Oosterloo et al. (2007). The position-velocity diagrams are compared with the prediction of three models: the isotropic model, the maximum rotation model and the three-integral high-σ_z model.

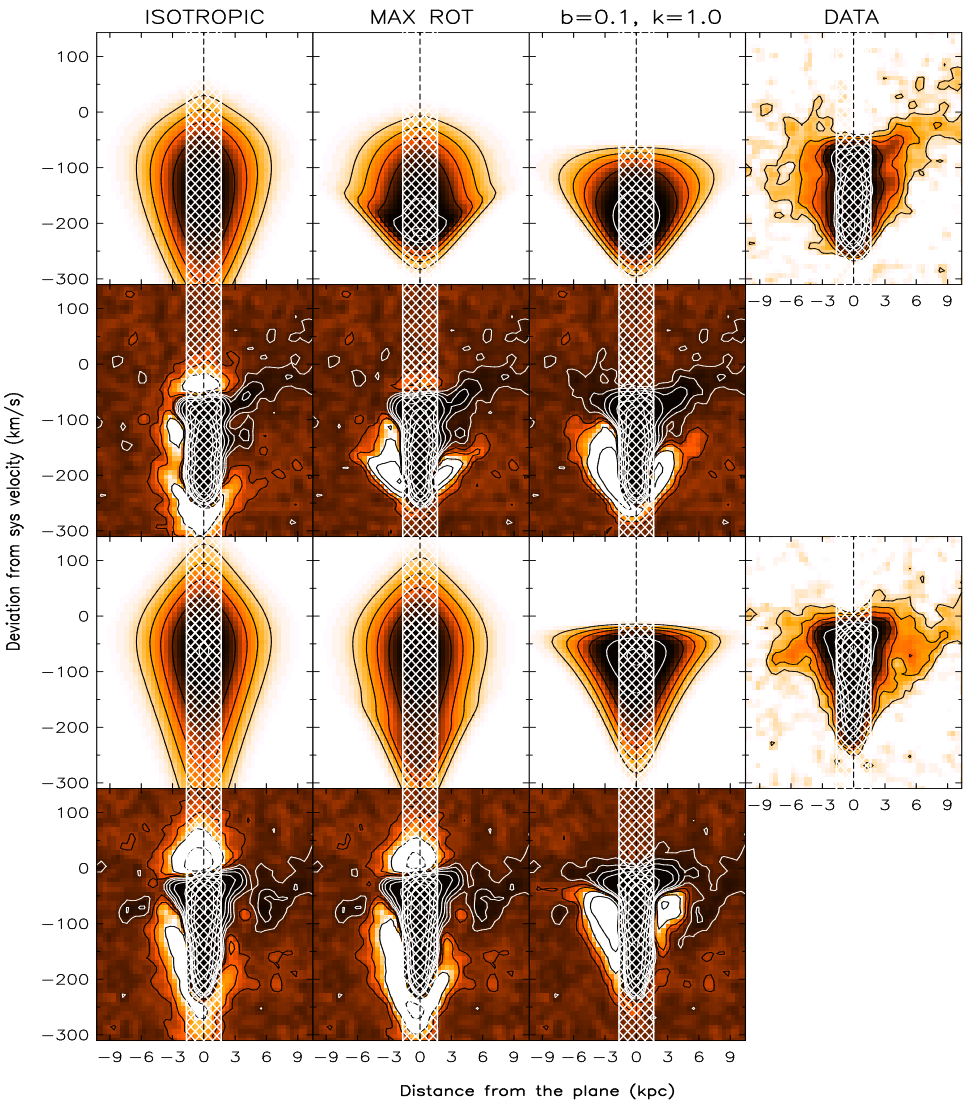

Figure 2.8: Comparison between two position-velocity cuts perpendicular to the plane of NGC 891 and some representative models. In the first row the cut is extracted at $R = 7.5\,\mathrm{kpc}$ on the N-E side of the galaxy, where the gas is moving towards the observer, and the corresponding residuals are presented in the second row. In the third row the cut is on the same side of the galaxy but at $R = 2.8\,\mathrm{kpc}$, and the corresponding residuals are shown in the fourth row. The shaded area in each plot delimits the emission expected from the disc. The contour levels are those of Figure 2.5. For the residuals, computed subtracting the model to the data, the black contours represents positive values whilst the white contours are the negative ones. The same contour levels (absolute value) of the position-velocity cuts are used.

Also the corresponding residuals are shown (second and fourth rows) computed as the difference between the data and the models; the shaded area in each position-velocity plot delimits the emission expected from the disc.

The characteristic triangular shape of the data diagrams (rightmost column) is due to the negative vertical gradient in the rotational velocity of the halo and is the key feature that the models should reproduce. Clearly, this is not the case for the isotropic model as the high velocity dispersion makes the emission very elongated, although a negative vertical gradient in the rotational velocity is visible. In the 2.8 kpc cut (third row), the emission is so elongated that a substantial amount of gas is apparently "counter-rotating" (upper part of the plot). The maximally rotating model (second column) also does not reproduce the shape of the emission especially at $R = 2.8$ kpc from the centre of the galaxy (third row). Also in this case the predicted line-of sight velocity dispersion is too high. The position-velocity diagrams for the high-σ_z model (third column) show a qualitative agreement with the data as the triangular shape is reproduced. However, the velocity dispersion in the upper halo $|z| > 5$ kpc is clearly not matched and there is a downward shift of the emission particularly visible in the 7.5 kpc cut. These features are also apparent in the residual maps and in particular the high-σ_z model, despite reproducing well the shape of the data, shows substantial residuals. In addition, the residuals also accentuate the intrinsic asymmetric distribution of the extra-planar gas with respect to the mid-plane of NGC 891.

Figure 2.8 gives a different view of the discrepancies already noted in Figures 2.5 and 2.7. The advantage of a cut perpendicular to the plane of the galaxy is that it captures in one diagram the kinematics of the extra-planar gas at different heights and, as mentioned, its characteristic triangular shape is the evidence of the gradient in rotational velocity with height. The only model that reproduces, at least qualitatively, this shape is the $b = 0.1, k = 1$ anisotropic model.

2.5 Discussion

In the previous Sections we have presented an alternative interpretation of the baroclinic fluid homogeneous models for extra-planar gas, i.e. that of a "gas" of H I clouds described by the stationary Jeans equations. Due to the formal equivalence of the equations describing the two systems, a similarity in the behaviour of the isotropic Jeans model and that of the baroclinic solutions of Barnabè et al. (2006) is expected. The present investigation is not just a re-interpretation of the results of of Barnabè et al. (2006): even in the isotropic case the Jeans models analysed here differ from those of of Barnabè et al. (2006) in the choice of the galaxy mass and the cloud density distribution. The choice of the mass model has a little impact on the properties of the solutions, but the form of the density distribution is critical. Barnabè et al. (2006) adopted a very flat density distribution, to reproduce the off-plane rotation curves. A flat density distribution requires less pressure support against the vertical gravitational field of the galaxy which results in a relatively low temperature of the gas, typically 10^5 K. For such a temperature the expected velocity dispersion in a Jeans isotropic model would have been of the order of $30\,\mathrm{km\,s^{-1}}$, close to the mean observed value (Oosterloo et al. 2007). Instead, in the present investigation the parameters of the density distribution are tuned to reproduce the observed H I distribution which has a greater scale-height than that used by Barnabè et al. (2006, see equation [2.17]). Thus, the typical values of the velocity dispersion necessary to sustain the halo are of a factor ~ 3 higher than the above. This high velocity dispersion has a large impact on the observable kinematics of the extra-planar gas and it is the main reason why the isotropic model fails to reproduce the data. The higher values of the velocity dispersion also influence the rotational velocities: indeed the rotation curves of the isotropic Jeans model are about $20\,\mathrm{km\,s^{-1}}$ lower than those obtained by Barnabè et al. (2006).

The high values of the velocity dispersion of the H I halo clouds may appear, at a first sight, unphysical. However, it should be noted that these velocities are unavoidable in any model attempting to reproduce gaseous haloes with such large scale-heights (e.g. Fraternali & Binney 2006). The source of kinetic energy for these clouds must ultimately come from supernovae, and indeed hydrodynamical simulations of superbubble expansion in galactic discs predict these kinds of blowout velocities (e.g. Mac Low & McCray 1988). In addition, velocities of the order of $100\,\mathrm{km\,s^{-1}}$ are in fact typical for halo clouds in the Milky Way (Wakker & van Woerden 1997) and have been observed in external galaxies whenever the inclination of the disc along the line-of-sight is favourable (e.g. Boomsma et al. 2008).

As already mentioned in Section 2.4.3, the most satisfactory model is the anisotropic $b = 0.1$, $k = 1$ model (or high-σ_z model), which has been constructed in order to have $\sigma_R = \sigma_\varphi < \sigma_z$. These requirements are roughly in agreement with the prescriptions for a galactic fountain where the material is ejected mostly vertically from the disc and falls back also vertically. Fraternali & Binney (2006, 2008) have built galactic fountain models for NGC 891 and compared them with the data cube in the same way as it was done here. They found that the halo gas distribution is well reproduced by fountain clouds that are kicked out of the disc with a Gaussian distribution of initial velocities and dispersion of about $80\,\mathrm{km\,s^{-1}}$, which is a value very similar to the average σ_z predicted by the stationary models presented here (Figure 2.6). Moreover, Fraternali & Binney (2006) investigated the opening angles about the normal to the plane of the ejected clouds finding that it has to be lower than 15 degrees, in other words the clouds are ejected almost vertically. Therefore, the $b = 0.1, k = 1$ model is quantitatively similar to the fountain models. What makes the difference between the two is the lack of non-circular (inflow and outflow) ordered motions in the stationary Jeans model that, instead, in fountain models are always present.

The most problematic discrepancy between the high-σ_z model and the data is visible in the channel map close to the systemic velocity (see channel

at $-5.2\,\mathrm{km\,s^{-1}}$ in Figure 2.7). This map shows the gas that has a null velocity component along the line-of-sight (once the systemic velocity has been removed). Much of this gas is located in the outer parts (in R) of the galaxy both in the disc and in the halo. The width of the channel (along the horizontal axis) is mostly due to the velocity dispersion of this gas. The high-σ_z model fails to reproduce the data in two ways: 1) the channel map is too narrow, 2) the width (in the x-axis) of the emission decreases with height in contrast to what it is seen in the data. These differences are caused by the fact that the velocity dispersion in the model decreases both with R and with z, whilst in the data the two behaviours seem reversed. The fact that the velocity dispersion increases with height has been clearly shown by Oosterloo et al. (2007) who built artificial cubes with different parameters and compared them with the NGC 891 data cubes. These authors also kept the dispersion constant with R and reproduced much better the shape of the channel maps close to the systemic velocity (see their Figure 14). The decrease of the velocity dispersion with R and z is a common problem of all the stationary Jeans models and may be related to the lack of (ordered) non-circular motions mentioned above.

In the high-σ_z model the rotational velocities can be directly compared with those obtained from the data because the line-of-sight velocity dispersion has values comparable with the observed one. Figure 2.9 shows the rotation curves of NGC 891 at distances from the plane of 3.9 kpc (top panel) and 5.2 kpc (from Fraternali et al. 2005). The rotational velocities predicted by the $b = 0.1, k = 1$ model are represented by solid lines, the dashed line indicates the rotation curve in the plane. In the derivation of these rotation curves from the data, it has been assumed a constant value of the velocity dispersion[3] ($20\,\mathrm{km\,s^{-1}}$). The curves have been obtained using

[3]Fraternali et al. (2005) assumed $\sigma_{\rm gas} \sim 8\,\mathrm{km\,s^{-1}}$, for the disc and the halo. Oosterloo et al. (2007) found that the velocity dispersion in the halo is actually larger and about $20\,\mathrm{km\,s^{-1}}$, thus it is appropriate to shift the data points of Fraternali et al. (2005) down by $11\,\mathrm{km\,s^{-1}}$ (see Fraternali & Binney 2008, for details). This is equivalent to derive the rotation curves assuming a constant $\sigma_{\rm gas} \sim 20\,\mathrm{km\,s^{-1}}$ for the halo region.

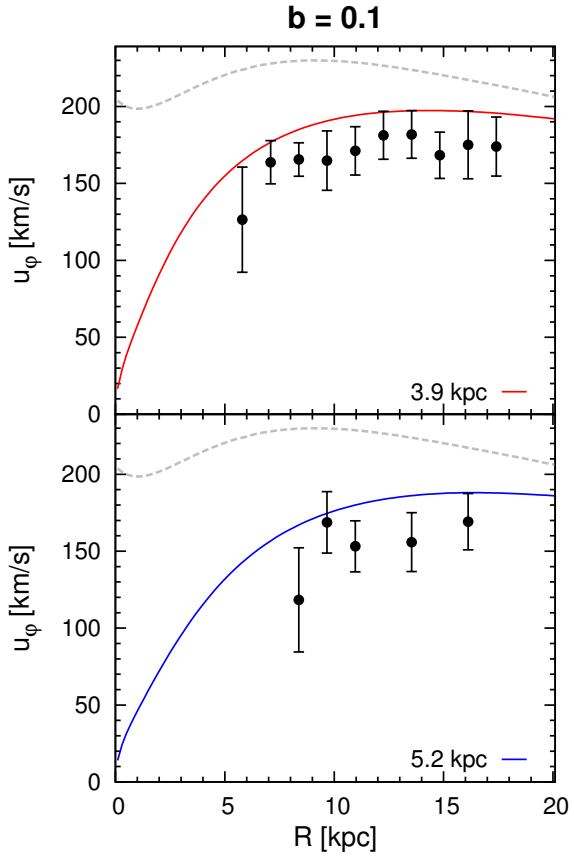

Figure 2.9: Rotational velocities of the model $b = 0.1$ and $k = 1$ (solid line) and rotation curves in the H I by Fraternali et al. (2005) (points with error bars) at $z = 3.9\,\mathrm{kpc}$ (top) and $z = 5.2\,\mathrm{kpc}$ (bottom). For each plot the long-dashed line represents the rotational velocity on the mid-plane.

the envelope tracing method, which is such that the larger is the velocity dispersion one assumes the lower is the obtained rotational velocity (recall equation [2.18]). In the high-σ_z model the velocity dispersion is not constant along R and it is exactly $20\,\mathrm{km\,s^{-1}}$ only at $\sim 10\,\mathrm{kpc}$ (Figure 2.6). Ideally one should correct the data points for this effect obtaining slightly lower velocities for $R < 10\,\mathrm{kpc}$ and higher for $R > 10\,\mathrm{kpc}$ but the effect is minimal. Overall, for what concerns the rotation curves of NGC 891, the high-σ_z stationary model predicts a gradient that is quite close to (although slightly lower than) the observed one.

The stationary models presented in this Chapter do not aim to explain the origin of the extra-planar gas. Instead their goal is to find a stationary description for the extra-planar gas phenomenon whatever physical mechanism is producing it, assuming that it can be considered roughly stationary. This assumption should be reasonably valid if the extra-planar gas is produced, for instance, by a galactic fountain and the star formation rate of the galaxy does not vary considerably with time as it seems to be the case for galaxies like the Milky Way (e.g. Twarog 1980; Cignoni et al. 2006). The investigation presented by Fraternali & Binney (2006) shows that the rotational velocities predicted by a galactic fountain model are systematically higher than the one derived from the data and also higher than those predicted by the stationary high-σ_z model shown in Figure 2.9. Fraternali & Binney (2008) revised the fountain model by including interactions of the fountain clouds with the surrounding ambient medium (see also Barnabè et al. 2006 for a similar suggestion and Chapter 4 and 5 of this Thesis). These interactions cause the fountain clouds to lose part of their angular momentum and to decrease their rotation velocities. Such a model is to date the best description for the dynamics of the extra-planar gas. In addition to the rotational velocities, this latter model reproduces the data cube in detail including the channel maps close to the systemic velocity (see Figure 2 of Fraternali & Binney 2008). Kaufmann et al. (2006) also reproduced the rotation curves of NGC 891 fairly well with a model in which the extra-planar gas forms by condensation of the extended warm-hot corona, but they did not attempt to build artificial data cubes to compare directly with the observations. However, the thermal instability on which such a model is based is unlikely to occur in galactic coronae, because of the combined effect of buoyancy and thermal conduction (Binney et al. 2009).

In the Jeans approach (but also in the baroclinic fluid homogeneous models) non-circular motions of the gas clouds have been neglected for simplicity, but in the kinematics of the extra-planar gas this kind of motions are clearly present (e.g. Boomsma et al. 2008; Fraternali et al. 2001) and

they could affect substantially the observed kinematics of the halo. More likely, the cause of the discrepancy between the Jeans treatment and the observations lies on the assumptions of a Jeans-based model and in particular on the ballistic nature of the cloud motion. Not only the drag between the H I halo clouds and the corona may have an important dynamical effect but also at the turbulent cloud/corona interface there may be a considerable exchange of mass and momentum. The analysis of these issues is deferred to Chapter 4 and 5 where hydrodynamical simulations of the cloud-corona interaction are presented.

2.6 Summary

Motivated by the results of Barnabè et al. (2006), the possibility that the extra-planar gas in spiral galaxies can be modelled as a "gas" composed by cold H I clouds, that obeys the stationary Jeans equations, was investigated. The implicit assumption of this approach is that the H I clouds, confined by the pressure of the hot corona, are moving almost ballistically in the halo. This assumption is valid in the limit of massive clouds having negligible rates of mass and momentum exchange with the corona.

Stationary and isotropic Jeans models can be considered as an alternative interpretation of fluid baroclinic models where the thermal pressure is replaced by the velocity dispersion tensor of the clouds, so that the problem of high temperature of gaseous homogeneous models is eliminated and the kinematics of the H I can be directly described. Simple phenomenological anisotropic models, which have not a fluid homogeneous counterpart, were also considered in this Chapter.

We constructed both anisotropic models in the well-constrained gravitational field of the spiral galaxy NGC 891 and we compared their predictions to the observed kinematics of the extra-planar gas in that galaxy. For each model, an artificial cube with the same resolution and total flux as the observations was built. The main results of this analysis can be summarized

as follows.

(i) The cloud density distribution, derived by the H I observations, leads to physically acceptable solutions ($u_\varphi^2 \geq 0$) in all the models investigated. This density distribution is centrally depressed and it has higher scale-height than that used by Barnabè et al. (2006) to match the vertical extension of the H I halo of NGC 891.

(ii) In all the models analysed, a negative vertical gradient in the rotational velocity, the distinctive feature of the kinematics of the extra-planar gas, is always present.

(iii) Vertical velocity dispersions σ_z of the order of $50 - 100\,\mathrm{km\,s^{-1}}$ are required to provide support against the vertical gravitational field of the galaxy. In the isotropic model, this implies that the line-of-sight velocity dispersion is a factor $\sim 3 - 4$ higher than that observed.

(iv) With the introduction of the anisotropy it is possible to reconcile the line-of-sight velocity dispersion to the observed values. Unfortunately, the predicted vertical gradient in the rotational velocity is too shallow and other features of the data cube are not fully reproduced.

The careful comparison with the observations performed in this Chapter, clearly indicates that the dynamics of extra-planar gas is not fully described by any of the stationary models considered here. However, a model with an anisotropic velocity dispersion tensor, which mimics a galactic fountain is the preferable among all. The fact that none of the stationary Jeans models analysed here can reproduce all the features of the observed (extra-planar) gas kinematics might suggest that the cloud motion is not purely ballistic, and that the interaction between the clouds and the coronal gas, in the form of mass and momentum exchange, plays an important dynamical role. These two processes, and their consequences for both the dynamics of the halo gas and the evolution of star-forming disc galaxies, are investigated, with the help of hydrodynamical numerical simulations, in Chapters 4 and

5, respectively. In the next Chapter we first describe the numerical code with which these simulations are carried out.

3

Numerical schemes for gas dynamics

3.1 Introduction

The dynamical processes in astrophysical gas systems can be modelled by the Euler equations – on the implicit assumption that the rate of collisions is sufficiently fast to justify a fluid description – where pressure is isotropic and a local thermodynamic equilibrium holds. In particular, this assumption allows to represent specific kinetic processes like viscosity, thermal conduction and radiative cooling, in terms of fluid models which can then be incorporated into the inviscid Euler system.

The numerical integration of the Euler equations requires specific algorithms, generically denoted as *upwind* or *shock-capturing* schemes. Several grid codes implementing upwind integration are available and widely used in the astrophysical community (e.g. ENZO Bryan & Norman 1997; RAMSES Teyssier 2002; PLUTO Mignone et al. 2007). Typically, these codes are based on second-order integration schemes, and take advantage of the AMR (Adaptive Mesh Refinement) technique to improve the accuracy locally.

In this Thesis a different approach has been adopted by using a higher order extension of the reference second order upwind schemes on a fixed (non adaptive) grid. This strategy appears to be preferred in astrophysical problems where mass, momentum and energy exchanges are dominated by turbulent mixing. In fact, higher order schemes reduce numerical diffusivity and thus allow to better represent small-scale structures generated by the turbulent motion.

In the present work we have implemented a C++ code, called ECHO++, based on the algorithm design of the ECHO (Eulerian Conservative High-Order, Del Zanna et al. 2007; Landi et al. 2008) code, where high-order, shock-capturing schemes are developed for fluid dynamics and magnetohydrodynamics (MHD), with a proper extension to relativistic regimes.

In the following, after a short introduction on the Euler equations, the basic upwind procedures designed to solve them on a grid and the corresponding implementation on our code are presented. Two Sections are dedicated, respectively, to the details of the implementation of the radiative cooling and to the discussion of the advection of passive scalars (used to treat different metallicities of the gas). Finally, some tests of the capabilities of the code will be presented.

3.2 Euler equations

This Section gives a short presentation of the main properties of the equations of hydrodynamics and in particular of the system of equations governing an inviscid flow, which are called Euler equations. These equations are the formalization of fundamental conservation laws and, in Cartesian coordinates, are given by

$$\frac{\partial \rho}{\partial t} + \nabla \cdot \rho \mathbf{v} = 0\,, \tag{3.1}$$

$$\frac{\partial \rho v_j}{\partial t} + \sum_{i=1}^{3} \frac{\partial}{\partial x_i} \left(\rho v_i v_j\right) + \frac{\partial P}{\partial x_j} = S_{\rho v}\,, \tag{3.2}$$

$$\frac{\partial E}{\partial t} + \nabla \cdot (E + P)\,\mathbf{v} = S_E\,, \tag{3.3}$$

which represent, respectively, conservation of mass, momentum (along the direction j) and energy. In the previous equations ρ is the mass density, $\mathbf{v}$ the velocity vector, P the pressure and E the total energy per unit volume of the fluid. The indexes i and j, which appear in equation (3.2), refer to the three Cartesian component of the velocity $\mathbf{v}$ along the spatial directions $(x_1, x_2, x_3) = (x, y, z)$. The terms on the right-hand-side of the momentum and energy conservation equations are called source terms and account for the variation of momentum and energy due to the action of external forces (such as gravity), diffusion processes (e.g. thermal conduction) and radiative cooling. In the current version of the code, only the case of an external gravitational field and the radiative cooling of the gas (which is presented in detail in Section 3.5) are implemented. To close the system given by equations (3.1), (3.2) and (3.3) an expression for the total energy per unit volume of the fluid is needed. In the case of an ideal fluid (the only that will be treated here) it is possible to express this latter as

$$E = \frac{1}{2}\rho||\mathbf{v}||^2 + \frac{P}{\gamma - 1}, \tag{3.4}$$

where the first term on the right-hand-side represents the kinetic energy of the fluid, the second term its internal energy (both per unit volume) and γ, assumed constant, is the adiabatic index.

Neglecting the source terms, the Euler equations (3.1), (3.2) and (3.3) can be written in the more compact form

$$\frac{\partial \mathbf{u}}{\partial t} + \sum_{i=1}^{3} \frac{\partial \mathbf{f_i}(\mathbf{u})}{\partial x_i} = 0, \tag{3.5}$$

where $\mathbf{u} = (\rho, \rho\mathbf{v}, E)$ is called vector of *conserved* variables and $\mathbf{f_i}(\mathbf{u})$ is the flux vector in the direction i. In some parts of the code (for example in reconstruction routines, see Section 3.4.1) *primitive* variables, defined as $\mathbf{w} = (\rho, \mathbf{v}, P)$, are also considered. The importance of equation (3.5) will become clearer in the course of the Chapter when numerical techniques, developed to solve the Euler equations, will be discussed.

A remarkable property of the Euler equations is that they are an *hyperbolic* system of conservation laws. Returning to equation (3.5), it can be easily shown that

$$\frac{\partial \mathbf{u}}{\partial t} + \sum_{i=1}^{3} \frac{\partial \mathbf{f_i}(\mathbf{u})}{\partial \mathbf{u}} \frac{\partial \mathbf{u}}{\partial x_i} = 0, \tag{3.6}$$

by expanding the spatial derivatives. The matrix $\mathbf{J_i} \equiv \mathbf{f_i}(\mathbf{u})/\partial \mathbf{u}$ in the previous equation is known as the Jacobian matrix of the flux and the system (3.6) is called hyperbolic if each $\mathbf{J_i}$ is diagonalizable and all its eigenvalues are real. Euler equations satisfy these requirements and in particular each $\mathbf{J_i}$ admits three distinct eigenvalues, also called characteristic speeds of the system, $\lambda^+ = v_i + c_s$, $\lambda^0 = v_i$ (of multiplicity 3), and $\lambda^- = v_i - c_s$, where v_i is the velocity of the fluid along the spatial direction i and c_s is known as the sound speed. In the case of an ideal fluid $c_s = (\gamma P/\rho)^{1/2}$. In addition, since the matrix $\mathbf{J_i}$ is diagonalizable it admits a complete basis set of eigenvectors, with respect to which equation (3.6) can be rewritten by defining the so-called *characteristic* variables (essentially a projection of the conservative variables $\mathbf{u}$ on to the *characteristic* directions defined by the eigenvectors). Without entering too much the mathematical details, it can be shown that locally (i.e. in the neighborhood of a reference state), in the basis defined by the eigenvectors, equation (3.6) – and in general any hyperbolic system – assumes the form of a system of decoupled wave equations, whose propagation speed is given by the eigenvalues of $\mathbf{J_i}$. However, due to the non-linearity of the Euler equations, the interaction among the waves is not given by a simple superposition but becomes more complex. In particular, this process may lead to the formation of discontinuous solutions that propagate with their own speed (which in general does not coincide with the eigenvalues of the system) into the fluid. For the Euler equations it is possible to distinguish two kind of discontinuous solutions: shock waves and tangential discontinuities. If primitive variables are considered, in the former case all the fluid variables but the tangential components of the velocity have a jump across the discontinuity, while in the latter the jump

is present in the density and in the tangential components of the velocity only[1]. Tangential discontinuities in which all the components of the velocity are continuous are called contact discontinuities.

Many numerical methods for the solutions of Euler equations rely on the hyperbolicity of the system and in particular on the decomposition along the characteristic directions of the equations. For what concerns the code presented in this Chapter, characteristic decomposition is avoided but nevertheless the eigenstructure of the Euler equations will be useful in Section 3.4.2, where the construction of approximate Riemann solvers is illustrated. The discussion about the properties of the eigenstructure of hyperbolic systems is not intended to be exhaustive. A more complete treatment can be found in any textbook of numerical methods for hyperbolic partial differential equations such as, for instance, Toro (1999) or Trangenstein (2009).

3.3 Structure of the code

All the simulations presented in this Thesis were performed with the numerical code ECHO++. ECHO++ is an Eulerian and fixed-grid (i.e. no adaptive mesh refinement is exploited) code, based on the algorithm design of the ECHO (Eulerian Conservative High-Order, Del Zanna et al. 2007; Landi et al. 2008) code, that employs high-order, shock-capturing schemes to solve the equations of hydrodynamics (3.1), (3.2) and (3.3) in presence of an external gravitational field and radiative cooling of the gas. The code is multi-dimensional and parallelized using the MPI-2 (Message Passing Interface) library.

The code was originally written in FORTRAN90 and it has been ported, as a part of this PhD project, in C++. The translation to another programming language has implied the necessity to modify some algorithms of the code, mainly for efficiency purposes. For instance, the input/output

[1] It is implicitly assumed that the surface of discontinuity is planar, and the fluid variables in the two regions of the space separated by this surface are constant.

routines were changed to make full use of the parallel input/output functionalities provided by the MPI-2 library. In particular, output and restart files can now be written or read collectively by all the processors. This simplifies code maintenance and increases its performances, especially for large files, since communication among the processors is avoided. Parallelization of the code is achieved by one-dimensional splitting (along the x direction) of the computational domain evenly among the processors. However, tests for three dimensional problems have shown that the adopted approach leads to poor scaling with the grid dimension. A version of the code exploiting a two-dimensional domain decomposition, which should give better performances, is currently under development and testing.

The most important part of the work carried out on the code during this PhD project was the implementation of the radiative cooling module, that support multiple metallicities of the gas, based on the cooling function of Sutherland & Dopita (1993). In particular, explicit time integration of the cooling term, which is directly added to the energy flux, was adopted. At least at this stage, other time integration strategies to treat the cooling term have not been included, but their implementation in future versions of the code will be considered. Further details on the (multi-metallicity) cooling module can be found in Sections 3.5 and 3.6.

The code solves the Euler equations (3.1), (3.2) and (3.3) by dividing the computational domain in a number of equal cells and adopting a *finite difference* formalism: instead of cell-averaged quantities, point values of the conservative variables $\mathbf{u}$, computed at cell centers, are evolved in time. This has the main advantage that the extension to the multi-dimensional case is simpler because the discretization of the fluxes at the cell boundaries [see equation (3.8) below] can be made separately, dimension by dimension, and there is no need for a complicated and computationally expensive multi-dimensional numerical interpolation. Since the extension to multiple dimensions is straightforward, the numerical solution of equation (3.5) is treated for simplicity in the one-dimensional case only.

Consider an interval $[a, b]$ divided in N cells $I_j = [x_{j-1/2}, x_{j+1/2}]$ of equal length $\Delta x = (b-a)/N$. Then the positions of the cell centers, which are identified as the grid points, are given by

$$x_j = a + (j - 1/2)\Delta x; \qquad j = 1, \ldots, N. \tag{3.7}$$

Discretization of equation (3.5) on the one-dimensional grid defined by equation (3.7) leads, in the so-called semi-discrete formalism (which consists in discretizing the spatial dependence only while retaining continuous time dependence), to

$$\frac{d\mathbf{u_j}}{dt} = -\frac{\hat{\mathbf{f}}_{\mathbf{j+1/2}} - \hat{\mathbf{f}}_{\mathbf{j-1/2}}}{\Delta x}, \tag{3.8}$$

where $\hat{\mathbf{f}}_{\mathbf{j\pm 1/2}}$ are called *numerical fluxes* and their difference on the right-hand-side is an approximation of the derivative of physical fluxes at the grid point x_j, while $\mathbf{u_j}$ are the conserved variables computed at the same location. Equation (3.8) is then integrated (notice that the subscript j was dropped for ease of notation) by using the standard total variation diminishing schemes of the second order

$$\begin{cases} \mathbf{u}^{(1)} = \mathbf{u}^n + \Delta t \mathcal{L}\left(\mathbf{u}^n\right) \\ \mathbf{u}^{n+1} = \dfrac{1}{2}\mathbf{u}^n + \dfrac{1}{2}\left[\mathbf{u}^{(1)} + \Delta t \mathcal{L}\left(\mathbf{u}^{(1)}\right)\right] \end{cases} \tag{3.9}$$

or third order

$$\begin{cases} \mathbf{u}^{(1)} = \mathbf{u}^n + \Delta t \mathcal{L}(\mathbf{u}^n) \\ \mathbf{u}^{(2)} = \dfrac{3}{4}\mathbf{u}^n + \dfrac{1}{4}\left[\mathbf{u}^{(1)} + \Delta t \mathcal{L}\left(\mathbf{u}^{(1)}\right)\right] \\ \mathbf{u}^{n+1} = \dfrac{1}{3}\mathbf{u}^n + \dfrac{2}{3}\left[\mathbf{u}^{(2)} + \Delta t \mathcal{L}\left(\mathbf{u}^{(2)}\right)\right] \end{cases} \tag{3.10}$$

based on Runge-Kutta methods (TVD-RK schemes, Shu & Osher 1988). In equations (3.9) and (3.10) the superscript n indicates the time discretization – the two schemes evolve the solution from the time step n to the time step $n+1$; $\mathbf{u}^{(1)}$ and $\mathbf{u}^{(2)}$ are just the intermediate stages of Runge-Kutta

methods – while the operator $\mathcal{L}$ represents the right-hand-side of equation (3.8) (source terms can be added if present). The two explicit time-integration schemes presented above are stable under the CFL (Courant-Friedrics-Lewy) condition $C < 1$, where C is called Courant number and enters the following determination of the maximum (stable) allowed time-step

$$\Delta t = C \min_i \left(\frac{\Delta x^i}{\alpha^i} \right), \quad C < 1 \tag{3.11}$$

where α^i is the largest speed of propagation of the characteristic waves (details in Section 3.4.2) and Δx^i the grid spacing both in the i direction.

To fully determine the solution strategy of equation (3.8), a procedure to compute its right-hand-side, and in particular the numerical fluxes $\hat{\mathbf{f}}_{\mathbf{j+1/2}}$, must be given (recall that source terms have a point value discretization equal to that of conservative variables). However, this procedure is rather involved due to the fact that Euler equations may admit discontinuous solutions (as, for example, shocks). Moreover, discontinuous solutions can also develop from smooth initial conditions, because of the non-linearity of the equations. The existence and the development of these discontinuities pose at least two important challenges from a computational point of view. The first one is the formation, near a discontinuity, of unphysical oscillations (Gibbs phenomenon) in the values of the flow variables, which ultimately lead the code to instability. The formation of the Gibbs phenomenon is intimately related to the interpolation process needed to recover the value of the fluid variables form the cell centers to the interfaces between them: oscillations appear whenever the interpolation is performed over a stencil[2] of points that crosses a discontinuity. The second challenge is that the algorithm must be able to "capture" the discontinuities that may eventually form during the evolution of the system. A discontinuity is captured when it is detected (located) and sharply resolved (in a few grid points). The procedure adopted in the code to recover the numerical

[2]In finite difference schemes, a stencil is the group of grid points used by a numerical procedure to obtain the desired approximation of a given variable.

fluxes is able to overcome the two challenges presented above because it is based on interpolations techniques having non-oscillatory properties, coupled with algorithms designed to efficiently solve a peculiar type of problem for the Euler equations known as Riemann problems (see Section 3.4.2). In particular, the procedure performs three steps that, starting from the point values of primitive variables $\mathbf{w_j}$ and passing through the point values of inter-cell fluxes $\mathbf{f_{j+1/2}}$, lead to the determination of the numerical flux functions $\hat{\mathbf{f}}_{\mathbf{j+1/2}}$. Each one of these steps will be analysed in detail in the next Section.

For completeness, the operations performed by the code at each time-step are listed below. In this list it is assumed that point values at the cell centers of the primitive variable are known.

(i) The left and right inter-cell states for primitive variables are reconstructed by means of one of the reconstruction routines presented in Section 3.4.1:

$$\{\mathbf{w_j}\} \rightarrow \{\mathbf{w_{j+1/2}}^{\mathrm{L}}\}, \{\mathbf{w_{j+1/2}}^{\mathrm{R}}\}; \qquad j = 1, \ldots, N. \tag{3.12}$$

(ii) The local Riemann problem at each inter-cell location $x_{j+1/2}$ is solved for the inter-cell flux $\mathbf{f_{j+1/2}}$, with an approximate Riemann solver (see Section 3.4.2):

$$\{\mathbf{w_{j+1/2}}^{\mathrm{L}}\}, \{\mathbf{w_{j+1/2}}^{\mathrm{R}}\} \rightarrow \{\mathbf{f_{j+1/2}}\}; \qquad j = 0, \ldots, N. \tag{3.13}$$

(iii) High-order correction to the inter-cell fluxes are computed (see Section 3.4.3) so that the approximation to the derivative of flux can be computed to the given order of accuracy:

$$\{\mathbf{f_{j+1/2}}\} \rightarrow \{\hat{\mathbf{f}}_{\mathbf{j+1/2}}\}; \qquad j = 0, \ldots, N. \tag{3.14}$$

(iv) Points from (i) to (iii) are repeated for every spatial direction.

(v) If present, source terms are added to the fluxes.

(vi) Conservative variables are recovered from primitive variables:

$$\{\mathbf{w_j}\} \rightarrow \{\mathbf{u_j}\}; \qquad j = 1, \ldots, N. \tag{3.15}$$

(vii) A sub-cycle of the TVD-RK routine is taken and the conservative variables are updated accordingly.

(viii) The new values of the primitive variables are recovered from the updated values of the conservative ones.

(ix) Points from (i) to (viii) are repeated for each sub-cycle of the TVD-RK time integration routine.

3.4 Algorithms

The discussion of the algorithms, implemented in ECHO++ for the determination of the numerical fluxes $\hat{\mathbf{f}}_{\mathbf{j+1/2}}$, closely follows that in Del Zanna et al. (2007) and Landi et al. (2008). The interested reader is invited to refer to these works, and references therein, for extensions to the MHD and the (general-)relativistic cases. We have just added, for completeness, some details on the implementation of the WENO (Weighted Essentially Non-Oscillatory) schemes, and a simple and standard method to construct the (approximate) Riemann solvers present in the code.

3.4.1 Reconstruction routines

The first step to recover an approximation of a given order to the numerical fluxes is to reconstruct the left and right inter-cell values $\mathbf{w}^{\mathbf{L}}_{\mathbf{j+1/2}}$ and $\mathbf{w}^{\mathbf{R}}_{\mathbf{j+1/2}}$ of primitive variables. The two reconstructed values are obtained by polynomial interpolation over two different sets of stencils, the first centered around x_j to approximate $\mathbf{w}^{\mathbf{L}}_{\mathbf{j+1/2}}$, and the second around x_{j+1} to approximate $\mathbf{w}^{\mathbf{R}}_{\mathbf{j+1/2}}$. [3]. In this Section, interpolation techniques

[3] It is worth mentioning the fact that, by symmetry, stencils used for the reconstruction of $\mathbf{w}^{\mathbf{L}}_{\mathbf{j+1/2}}$ are the same employed for the reconstruction of $\mathbf{w}^{\mathbf{R}}_{\mathbf{j-1/2}}$.

		$c_{i,k}$		
Stencil	k	$i=0$	$i=1$	$i=2$
WENO3				
S0	0	-1/2	3/2	–
S1	1	1/2	1/2	–
CENO3				
S0	0	3/8	-10/8	15/8
S1	1	-1/8	6/8	3/8
S2	2	3/8	6/8	-1/8
WENO5				
S0	0	3/8	-10/8	15/8
S1	1	-1/8	6/8	3/8
S2	2	3/8	6/8	-1/8

(*a*)

Scheme	η_1	η_2	η_3
WENO3	1/4	3/4	–
WENO5	1/16	10/16	5/16

(*b*)

Scheme	d_0	d_2	d_4
WENO3	1	-1/24	–
CENO3	1	-1/24	–
WENO5	1	-1/24	3/640

(*c*)

Table 3.1: Table of the coefficients for the schemes used in the code. Panel (a): coefficients $c_{i,k}$ of the interpolation routines. Panel (b): ideal weights for WENO schemes. Panel (c): coefficients for high-order flux correction.

based on CENO (Convex Essentially Non-Oscillatory, Liu & Osher 1998) and WENO (Weighted Essentially Non-Oscillatory, see Jiang & Shu 1996) schemes will be discussed. In these techniques, stencils are used *adaptively* to recover variables (or fluxes) at cell interfaces, in order to limit the presence of spurious oscillations that form in the solution near discontinuities (such as shocks). In particular, in the smooth part of the flow symmetric stencils are used, whilst near discontinuities the stencil shifts to the right or to the left, according to selection criteria embedded in the scheme, to choose the smoothest part of the flow for the interpolation process. In this way, the goal of high-resolution is achieved both in smooth and non-smooth regions of the flow and the discontinuities, that may eventually develop during the temporal evolution, are captured. In the essentially non-oscillatory framework spurious oscillations are not completely suppressed, but their magnitude is of the order of the truncation error of the scheme. However, oscillations given by symmetric stencils that cross a discontinuity would be much higher because, independently of the resolution, they are proportional

to the magnitude of the jump itself.

The reconstruction procedure, based on (essentially) non-oscillatory techniques, is presented in detail for $\mathbf{w}^{\mathbf{L}}_{\mathbf{j+1/2}}$ only. The corresponding reconstruction procedure for the right state can be easily obtained by symmetry. Since the techniques illustrated here can be separately applied to each component of the vector $\mathbf{w}$ of primitive variables, in the discussion that follows a generic component w of that vector is considered for ease of notation, and its values at x_j is indicated with w_j. Both CENO and WENO techniques start with k polynomials $p_k(x)$, associated to the stencils Sk shown in Figures 3.1 and 3.2, which, computed at $x_{j+1/2}$, assume the form

$$p_k = \sum_{i=0}^{r-1} c_{i,k} w_{i+j+k-r+1}, \qquad k = 0, \ldots, r-1, \tag{3.16}$$

and approximate (to the desired order r) the inter-cell value $w^L_{j+1/2}$. In equation (3.16) and $c_{i,k}$ are constant coefficients, listed in Table 3.4 (panel a) for all the schemes, that give the sought order of interpolation and can be obtained, for instance, by the application of the Lagrange formula (see Del Zanna et al. 2007). It should be noticed that the values of $c_{i,k}$ differ from those presented in the literature where, usually, the direct reconstruction of the fluxes is performed.

In the third order CENO procedure (from now onwards CENO3), three quadratic interpolants (order of interpolation $r = 3$) for the interface value $w^L_{j+1/2}$ are computed according to equation (3.16), together with the linear reconstruction

$$\bar{L} = w_j + \text{minmod}(w_j - w_{j-1}, w_{j+1} - w_j). \tag{3.17}$$

In the previous equation the minmod function is defined as

$$\text{minmod}(a,b) = \begin{cases} \min(a,b) & a > 0, \quad b > 0 \\ \max(a,b) & a < 0, \quad b < 0 \\ 0 & \text{otherwise} \end{cases} \tag{3.18}$$

and it is used as slope-limiter in the linear reconstruction to guarantee non-oscillatory properties. To compute the linear interpolation (3.17) other

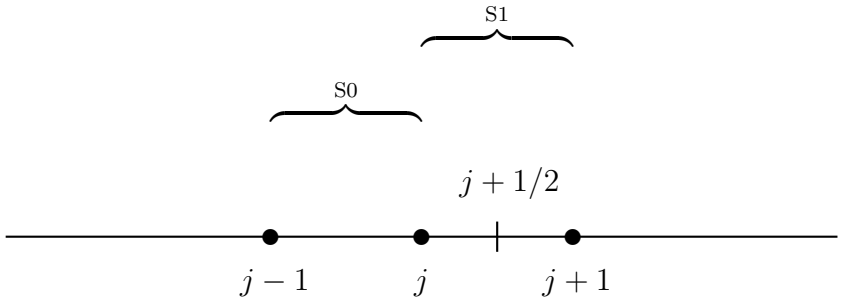

Figure 3.1: left interpolation stencils used in the WENO3 scheme. stencils for the point $j-1/2$.

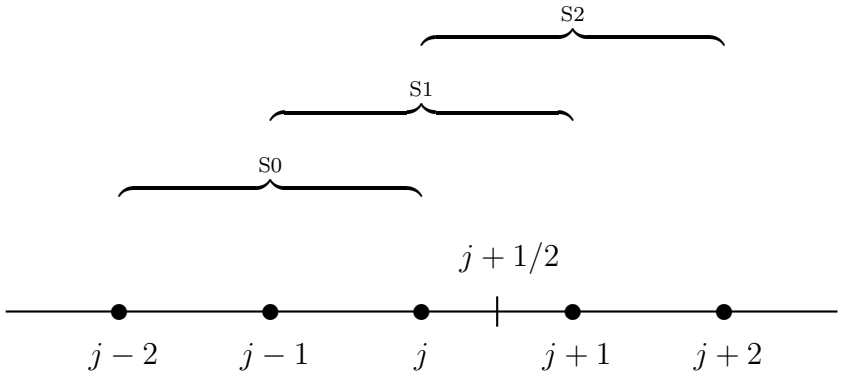

Figure 3.2: left interpolation stencils used in the CENO3 and WENO5 schemes.

slope-limiters (such as the monotonized centered Del Zanna et al. 2007) may be used as well. The selection of the smoothest approximation to $w^L_{j+1/2}$ starts by taking weighted differences of the three quadratic interpolants p_k with the linear reconstruction $\bar{L}$ of the form

$$D_k = \beta_k(p_k - \bar{L}), \tag{3.19}$$

where the values of the weights β_k are fixed to $\beta_0 = 1$, $\beta_1 = 0.7$ and $\beta_2 = 1$ in order to bias towards central interpolation. Then, in the regions where

all the D_k have the same sign

$$w^L_{j+1/2} = p_{\underline{k}}, \qquad |D_{\underline{k}}| = \min_k(|D_k|), \tag{3.20}$$

whereas in the other regions the linear interpolant is chosen. Therefore, near discontinuities the CENO3 scheme reduces to linear or even to first order reconstructions.

WENO schemes adopt a different strategy to obtain the sought approximation to $w^L_{j+1/2}$. The basic idea is to combine the k polynomial approximations p_k (each of order r) as

$$w^L_{j+1/2} = \sum_{k=0}^{r-1} \eta_k p_k, \tag{3.21}$$

to obtain an approximation of order $2r-1$ to the inter-cell values of the primitive variables. The quantities η_k in equation (3.21) are called optimal weights and their values for the third order (WENO3) and the fifth order (WENO5) schemes are listed in Table 3.4 (panel b). To ensure, however, non-oscillatory properties to the reconstruction, the optimal weights η_k must be adapted to the relative smoothness of the interpolant p_k in such a way that interpolants which cross a discontinuity are effectively assigned a zero weight, while for smooth region one recovers the $2r-1$ order approximation (3.21). For this purpose a parameter, that measure the smoothness of the interpolant over the cell $[x_{j-1/2}, x_{j+1/2}]$, is assigned to each p_k. These *smoothness indicators* IS_k are defined as (Jiang & Shu 1996)

$$IS_k = \sum_{l=1}^{r-1} \int_{x_{j-1/2}}^{x_{j+1/2}} \Delta x^{2l-1} \left(\frac{d\, p_k(x)^{(l)}}{dx} \right)^2 dx, \tag{3.22}$$

and provide a smoothness measurement of the interpolating polynomials by summing the squares of the L^2 norm of the first $r-1$ derivatives of $p_k(x)$ over the cell. The smaller the norm, the smaller the variation of $p_x(x)$ in the considered interval of the integration, which in turn implies a smoother approximation to the inter-cell value. Equation (3.22) gives the following results for the WENO3 scheme

$$IS_0 = (w_j - w_{j-1})^2, \tag{3.23}$$

$$IS_1 = (w_{j+1} - w_j)^2, \tag{3.24}$$

while for the WENO5 scheme

$$IS_0 = \frac{13}{12}(w_{j-2} - 2w_{j-1} + w_j)^2 + \frac{1}{4}(w_{j-2} - 4w_{j-1} + 3w_j)^2, \tag{3.25}$$

$$IS_1 = \frac{13}{12}(w_{j-1} - 2w_j + w_{j+1})^2 + \frac{1}{4}(w_{j-1} - w_{j+1})^2, \tag{3.26}$$

$$IS_2 = \frac{13}{12}(w_j - 2w_{j+1} + w_{j+2})^2 + \frac{1}{4}(3w_j - 4w_{j+1} + w_{j+2})^2. \tag{3.27}$$

Once the smoothness indicators are computed, new weights are formed by taking

$$\omega_k = \frac{\alpha_k}{\sum_{i=0}^{r-1} \alpha_i}, \tag{3.28}$$

where

$$\alpha_k = \frac{\eta_k}{(\epsilon + IS_k)^2}. \tag{3.29}$$

In equation (3.29) ϵ is a small number (usually fixed at 10^{-6}) introduced to avoid division by zero. As a final step, the approximation to the interface value $w^L_{j+1/2}$ is computed by replacing, in equation (3.21), the ideal weights η_k with the new weights ω_k. The definition of ω_k is such that non-oscillatory properties are guaranteed to the reconstruction of $w^L_{j+1/2}$ because in smooth regions ω_k reduce to the ideal weights η_k, allowing for the maximum order of spatial reconstruction while, in the presence of a discontinuity in one or more of the stencils, the associated ω_k assumes a value close to zero effectively disabling the usage of the corresponding p_k in the interpolation process.

3.4.2 Riemann solvers

After having reconstructed the inter-cell values $\mathbf{w^L_{j+1/2}}$ and $\mathbf{w^R_{j+1/2}}$ with one of the techniques presented in Section 3.4.1, a value for the inter-cell flux $\mathbf{f_{j+1/2}}$ must be recovered. In particular, the variable reconstructed at the inter-cell mentioned above define a *Riemann problem* for the Euler equations (3.1), (3.2) and (3.3) whose solution provides the required value for $\mathbf{f_{j+1/2}}$.

In general, Riemann problems can be defined for every system of conservation laws (or any system of hyperbolic partial differential equations) and their solution is a fundamental part in any high-resolution, shock-capturing code. They consist in a particular set of initial conditions for the system under examination composed by two constant states separated by a single discontinuity. In a one-dimensional problem (the only case in which we are interested in the present discussion) let us suppose, without any loss of generality, that the discontinuity (which coincides with the interface between two cells) is located at[4] $x = 0$. Thus, the initial conditions, in conservative variables, can be expressed as

$$\mathbf{u} = \begin{cases} \mathbf{u_L} & x \leq 0 \\ \mathbf{u_R} & x > 0, \end{cases} \tag{3.30}$$

Depending on the system of conservations laws considered, the initial conditions (3.30) will evolve in a way that is intimately linked with the eigenstructure of the system itself. As a general rule, the initial states will interact in the region around the discontinuity, giving rise to a number of intermediate states (that may not be distinct), connecting $\mathbf{u_L}$ and $\mathbf{u_R}$, equal to the number of the distinct eigenvalues of the system decreased by one. The states (including $\mathbf{u_L}$ and $\mathbf{u_R}$) are separated by i characteristic waves that propagate with a given speed α^i, i being the number of distinct eigenvalues. Therefore, the solution of a Riemman problem involves the determination of both the intermediate states and the values of the wave speeds. With this information, the flux at the interface (i.e. $\mathbf{f_{j+1/2}}$) can be easily computed. Figure 3.3 illustrate the structure of a Riemann problem in the case of a system with two opposed values for the wave speeds. As a final remark, we must stress that wave speeds *do not* in general coincide with the eigenvalues of the system, and this is the reason why they must be determined to completely solve the problem. A typical case in the Euler equation is represented by a shock wave that propagates with a velocity that is always greater than the highest eigenvalue of the system (in absolute value).

[4]It is always possible, by shifting the system of coordinates, to reduce to this case.

In the case of Euler equations a general Riemann problem can be solved analytically. However, the analytic solution has a high computational cost that makes its implementation impractical in numerical codes. Thus, from the point of view of computational efficiency, it is convenient to develop methods that solve Riemann problems in some approximate way. These algorithms are know as (approximate) Riemann solvers. The literature about this subject is vast and a number of solvers has been developed and tested with success. In this Section the discussion is limited to the two solvers actually implemented into the code: the (local) Lax-Friedrics (Lax 1954; Rusanov 1961) and the HLL (Harten et al. 1983) solvers. For a more complete discussion on Riemann problems and the design of (approximate) Riemann solvers, even for systems of conservation laws different from the equations of hydrodynamics, the interested reader may refer to Toro (1999) and Trangenstein (2009).

The philosophy underneath approximate Riemann solvers is to suitably approximate the original Riemann problem (3.30) and then to solve it exactly. The usual approach is to make assumptions on the structure of the solution. In particular, the solvers presented here impose that the solution of the problem must have the following simplified form: (i) there are two wave speeds only (instead of three) and, (ii) the state that connects the initial states $\mathbf{u_L}$ and $\mathbf{u_L}$, which is indicated as $\mathbf{u}^*$, has a constant value. These assumptions are illustrated in Figures 3.3 and 3.5 for the Lax-Friedrics (LxF) and the HLL solvers, respectively. Then, from an operational point of view, the solution of the Riemann problem proceeds through the following steps.

(i) An estimate of the wave speeds is adopted. For stabilty reasons these speeds must bound the wave speeds of the original (not approximate) problem, so that, in a time-step, Riemann problems coming from distinct interfaces cannot interact. This latter is an important point, however the numerical tests performed with ECHO++ have shown that, usually, the greatest and the smallest eigenvalues of the system

work remarkably well.

(ii) The value of the intermediate state $\mathbf{u}^*$ is computed by reverting to the integral form of the equations (i.e. by integrating them in a control volume, that contains the discontinuity, and over a time interval Δt) and by applying the Stokes' theorem in the resulting integration domain.

(iii) Finally, the flux at the interface is evaluated by using the same technique (although on a different integration domain).

Points (ii) and (iii) require further explanations. In particular, over the whole Chapter it has been claimed that Euler equations may admit discontinuous solutions. However, it should be noticed that these conservation equations, expressed in the form (3.1), (3.2) and (3.3), are no longer valid when a discontinuity is present simply because spatial derivatives are not defined for discontinuous functions. So discontinuous solutions must be considered as solution in *weak* sense that is, loosely speaking, solutions which satisfy the integral (or weak) form of the equations. It is in the integral form of the equations that Stokes' theorem becomes a powerful tool, which is used to determine the intermediate states (and the flux at the interface) needed for the solution of Riemann problems. To see how Stokes' theorem is linked to the construction of approximate Riemann solvers it is better to directly present the construction of the solvers used in the code, starting form the LxF case.

LxF approximate Riemann solver

In this particular solver it is further assumed that the two wave speeds are equal in magnitude but with opposed sign and their magnitude is indicated α. In Figure 3.3 a sketch in the $x-t$ plane of how the solution of the problem evolves in time is presented. The two lines $t = \pm\alpha x$ divide the $x-t$ plane in three regions (the L,R and star regions), where the solution is represented by the constant states $\mathbf{u_L}$, $\mathbf{u_R}$ and $\mathbf{u}^*$, respectively. To find

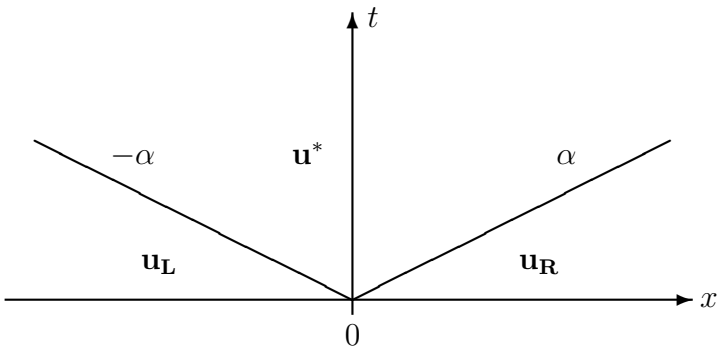

Figure 3.3: sketch of the approximate LxF Riemann solver. This solver can be viewed as an HLL solver where $\alpha = \max(|\alpha^+|, |\alpha^-|)$.

$\mathbf{u}^*$ equation (3.5) is integrated in the rectangular domain $[x_L, x_R] \times [0, \Delta t]$, delimited in Figure 3.4 (panel a) by the contours with the arrows, to obtain

$$\begin{aligned}\int_0^{\Delta t}\int_{x_L}^{x_R}\left(\frac{\partial \mathbf{u}}{\partial t}+\frac{\partial \mathbf{f}(\mathbf{u})}{\partial x}\right)\,dxdt = \\ -\int_{\Delta t}^{0}\mathbf{f}(\mathbf{u_R})\,dt-\int_0^{\Delta t}\mathbf{f}(\mathbf{u_L})\,dt+\quad\int_{x_L}^{x_R}\mathbf{u}^*\,dx \\ +\int_0^{x_L}\mathbf{u_L}\,dx+\quad\int_{x_R}^{0}\mathbf{u_R}\,dx=0,\end{aligned}\tag{3.31}$$

where the last equality holds because the integrand in the left-hand-side is zero. It is apparent form the previous equation that it is perfectly equivalent to integrate equation (3.5) over the bi-dimensional domain $[x_L, x_R] \times [0, \Delta t]$, or to consider in the integration along the contour defined by the arrows of the vector field $(\mathbf{u}, -\mathbf{f}(\mathbf{u}))$. This is exactly what Stokes' theorem states. Therefore, performing the contour integration in equation (3.31) and recalling that $x_L = -\alpha\Delta t$ and $x_R = \alpha\Delta t$ (as it is apparent from the figure), yields

$$\mathbf{f}(\mathbf{u_R}) - \mathbf{f}(\mathbf{u_L}) + 2\alpha\mathbf{u}^* - \alpha\mathbf{u_L} - \alpha\mathbf{u_R} = 0,\tag{3.32}$$

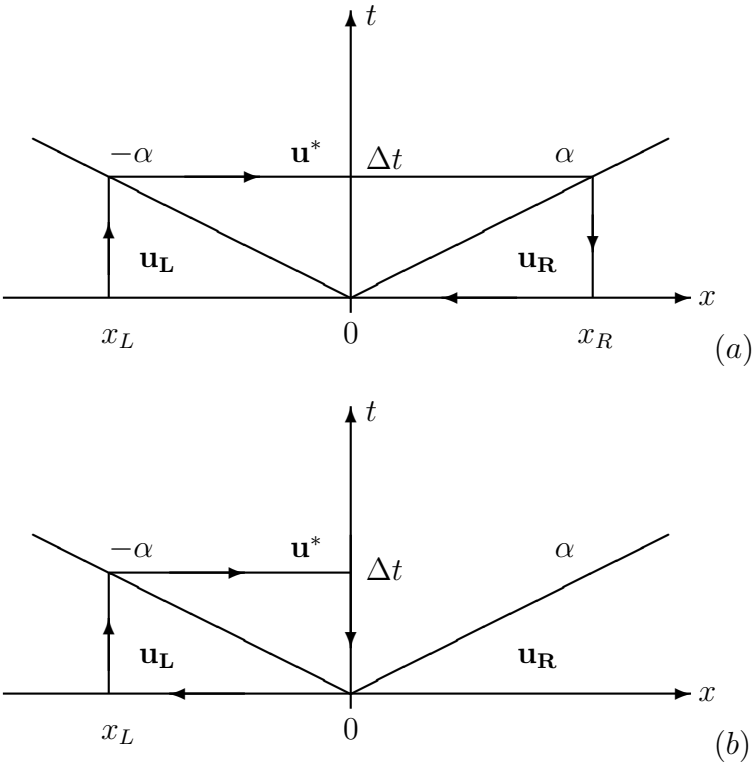

Figure 3.4: circuits used to compute the solution of the approximate Riemann problem in the Lax-Friedrics case. Panel (a): integration contour for the intermediate state $\mathbf{u}^*$. Panel (b): integration contour for the flux.

which can be readily solved for $\mathbf{u}^*$, leading to

$$\mathbf{u}^* = \frac{\mathbf{f}(\mathbf{u_L}) - \mathbf{f}(\mathbf{u_R}) + \alpha(\mathbf{u_L} + \mathbf{u_R})}{2\alpha}. \tag{3.33}$$

To compute the flux at the inter-cell (i.e. at $x = 0$) Stokes' theorem is applied to the two-dimensional region shown in Figure 3.4 (panel b), leading to

$$-\int_0^{\Delta t} \mathbf{f}(\mathbf{u_L})\, dt - \int_{\Delta t}^{0} \mathcal{F}^{\mathrm{LxF}}\, dt + \int_{x_L}^{0} \mathbf{u}^* + \int_0^{x_L} \mathbf{u_L} = 0, \tag{3.34}$$

where the flux at the inter-cell has been indicated as $\mathcal{F}^{\mathrm{LxF}}$. Recalling again that $x_L = -\alpha\Delta t$ and evaluating the integrals, we obtain

$$\mathcal{F}^{\mathrm{LxF}} = \mathbf{f_L} - \alpha(\mathbf{u}^* - \mathbf{u_L}) \tag{3.35}$$

and thus, by substituting equation (3.33),

$$\mathcal{F}^{\mathrm{LxF}} = \frac{\mathbf{f_L} + \mathbf{f_R} - \alpha(\mathbf{u_R} - \mathbf{u_L})}{2}. \tag{3.36}$$

The value of $\mathcal{F}^{\mathrm{LxF}}$ in equation (3.36) will be then assigned to the inter-cell flux $\mathbf{f_{j+1/2}}$. For what concerns the estimate of the wave speed α several choices are possible. The procedure implemented in the code is to construct a reference state for the interface as $(\mathbf{w^L_{j+1/2}} + \mathbf{w^R_{j+1/2}})/2$ and to take, at the reference state, the maximum (in magnitude) among the eigenvalues of the Euler equations. The values of α are also used in equation (3.11) for the determination of the time-step.

HLL approximate Riemann solver

The only complication introduced in the HLL Riemann solver with respect to the solver presented above is that the two wave speeds, indicated as α^- and α^+ have not the same magnitude, and in particular $\alpha^- < \alpha^+$. As can be seen by looking at the Figure 3.5, also in this case the $x - t$ plane is divided in three regions, called again L, R and star, where the solution is represented by the constant states $\mathbf{u_L}$, $\mathbf{u_R}$ and $\mathbf{u}^*$, respectively. The states $\mathbf{u_L}$ and $\mathbf{u}^*$ are separated by the line $t = \alpha^- x$, while the line $t = \alpha^+ x$ separates $\mathbf{u}^*$ and $\mathbf{u_R}$. However, three configurations are possible for the problem, which are depicted in the three panels of the Figure, depending on the signs of the wave speeds. In configuration (b), where both speeds are positive, and configuration (c), where both are negative, the evaluation of the inter-cell flux is trivial: by a careful inspection of Figure 3.5 it can be seen that in the former case (panel b) the flux is equal to $\mathbf{f_L}$, while in the latter (panel c) the value $\mathbf{f_R}$ is taken. The last case to discuss is that shown in panel (a) where $\alpha^- < 0 < \alpha^+$. For this case the flux is evaluated by following the same procedure adopted for the LxF solver.

Application of Stokes' theorem to the two-dimensional region shown in

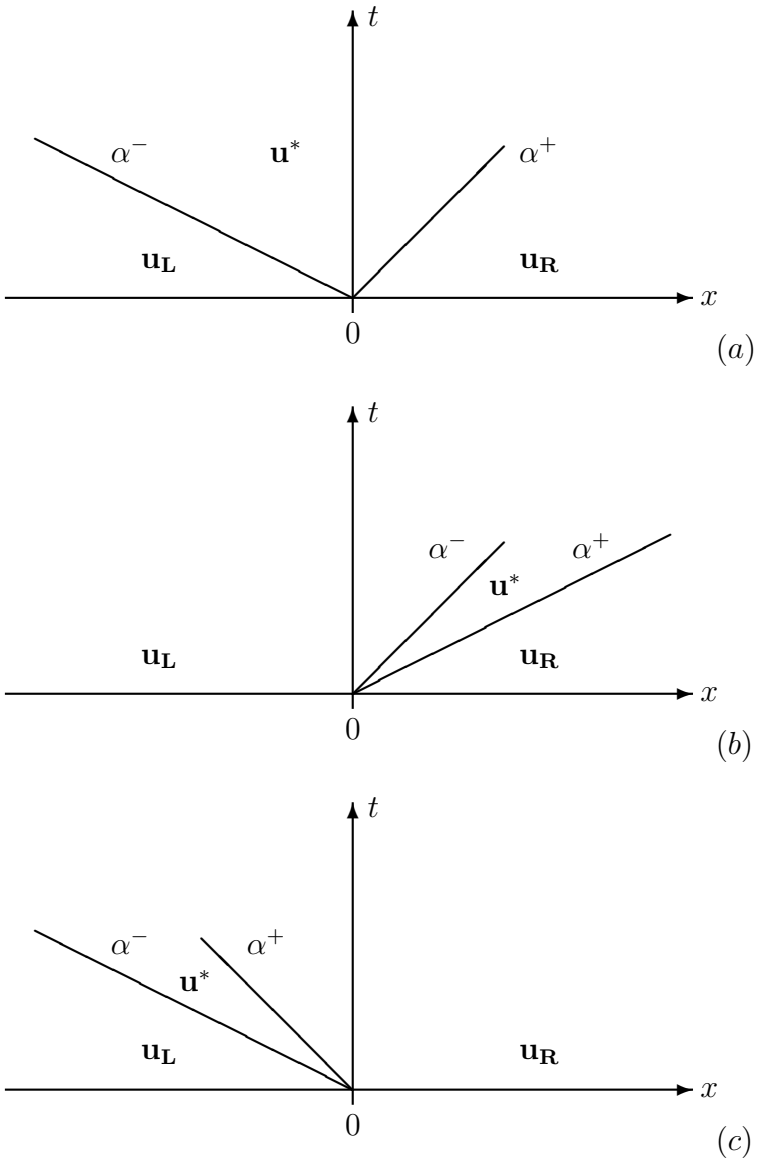

Figure 3.5: sketch of the approximate HLL Riemann solver. Panel (a): $\alpha^+ \neq \alpha^-$. Panel (b): $\alpha^- \geq 0$. Panel (c): $\alpha^+ \leq 0$.

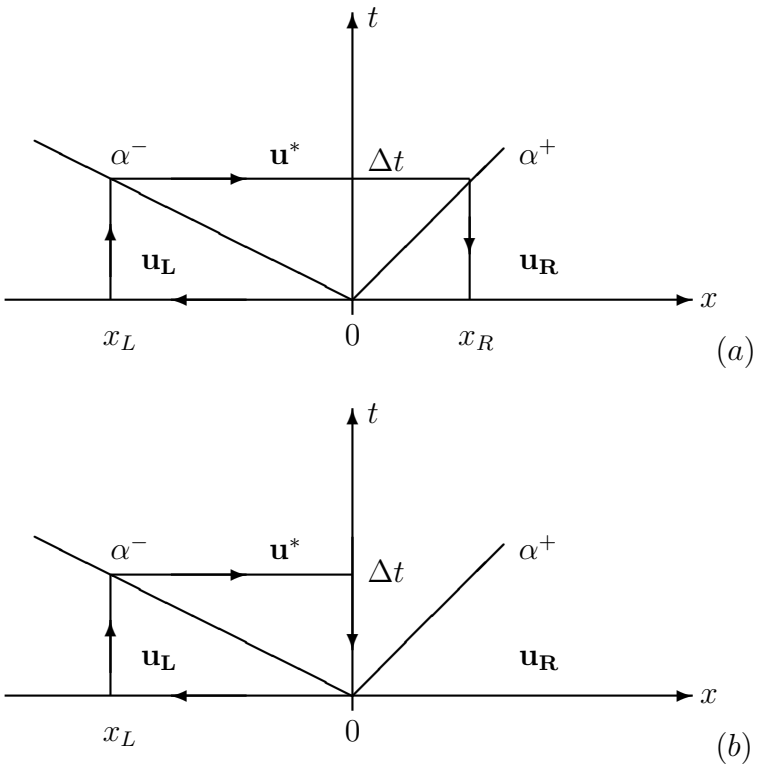

Figure 3.6: circuits used to compute the solution of the approximate Riemann problem in the HLL case. Panel (a): integration contour for the intermediate state $\mathbf{u}^*$. Panel (b): integration contour for the flux.

Figure 3.6 (panel a) gives

$$-\int_0^{\Delta t}\mathbf{f}(\mathbf{u_L})\,dt-\int_{\Delta t}^{0}\mathbf{f}(\mathbf{u_R})\,dt+\int_{x_L}^{x_R}\mathbf{u}^*\,dx + \int_0^{x_L}\mathbf{u_L}\,dx+\int_{x_R}^{0}\mathbf{u_R}\,dx=0. \tag{3.37}$$

Integrations in the previous equation can be easily performed and, by recalling that $x_L=\alpha^-\Delta t$, $x_R=\alpha^+\Delta t$, we obtain

$$\mathbf{f}(\mathbf{u_L})-\mathbf{u}^*(\alpha^+-\alpha^-)-\mathbf{u_L}\alpha^-+\mathbf{u_R}\alpha^+-\mathbf{f}(\mathbf{u_R})=0, \tag{3.38}$$

which, solving for $\mathbf{u}^*$ leads to

$$\mathbf{u}^*=\frac{\mathbf{f}(\mathbf{u_L})-\mathbf{f}(\mathbf{u_R})+\mathbf{u_R}\alpha^+-\mathbf{u_L}\alpha^-}{\alpha^+-\alpha^-}. \tag{3.39}$$

The flux at the inter-cell $\mathcal{F}^{\mathrm{HLL}}$ is computed by integrating along the contour shown in Figure 3.6 (panel b). This procedure yields

$$\mathcal{F}^{\mathrm{HLL}} = \mathbf{f_L} + \alpha^-(\mathbf{u}^* - \mathbf{u_L}) \tag{3.40}$$

and by substituting equation (3.39)

$$\mathcal{F}^{\mathrm{HLL}} = \frac{\alpha^+\mathbf{f_L} - \alpha^-\mathbf{f_R} + \alpha^+\alpha^-(\mathbf{u_R} - \mathbf{u_L})}{\alpha^+ - \alpha^-}. \tag{3.41}$$

Summarizing, the general form of the flux in the HLL case, which takes into account all possible configurations of the problem, is given by

$$\mathcal{F}^{\mathrm{HLL}} = \begin{cases} \mathbf{f_L} & \alpha^- > 0 \\ \dfrac{\alpha^+\mathbf{f_L} - \alpha^-\mathbf{f_R} + \alpha^+\alpha^-(\mathbf{u_R} - \mathbf{u_L})}{\alpha^+ - \alpha^-} & \alpha^- < 0 < \alpha^+ \\ \mathbf{f_R} & \alpha^+ < 0 \end{cases} \tag{3.42}$$

and the value of $\mathcal{F}^{\mathrm{HLL}}$ will be then assigned to $\mathbf{f_{j+1/2}}$. Also in this case there are several possibilities to estimate the values of the wave speeds α^- and α^+. In the code the following procedure is adopted. First of all, at left and right state the highest λ^+ ad the lowest λ^- eigenvalues are computed. Then $\alpha^+ = \max(\lambda^+(\mathbf{w^L_{j+1/2}}), \lambda^+(\mathbf{w^R_{j+1/2}}))$ and $\alpha^- = \min(\lambda^-(\mathbf{w^L_{j+1/2}}), \lambda^-(\mathbf{w^R_{j+1/2}}))$. For the determination of the time-step the value $\alpha = \max(|\alpha^+|, |\alpha^-|)$ is used.

As a final consideration on the approximations made in the solvers presented in this Section, it is worth mentioning the fact that only two wave speeds are employed, instead of three as the structure of the Riemann problems for the Euler equations would require. This might potentially lead to a more pronounced smearing of the discontinuities, especially contact discontinuities (where only the density has a jump at $x = 0$). However, when the Riemann solvers of this Section are coupled with high-order schemes, like those presented in Section 3.4.1, their performances are comparable with those obtained by more sophisticated, but also more computationally expensive, codes in which other solvers (for example Roe-type solvers, Roe 1981) or characteristic decomposition are employed.

3.4.3 Derivation routines

Once the inter-cell fluxes $\mathbf{f_{j+1/2}}$ are obtained, the final step is to compute the numerical flux functions $\hat{\mathbf{f}}_{\mathbf{j+1/2}}$ in such a way that the quantity $(\hat{\mathbf{f}}_{\mathbf{j+1/2}} - \hat{\mathbf{f}}_{\mathbf{j-1/2}}/\Delta x)$ approximates to a given order r the flux derivative $\partial \mathbf{f}(\mathbf{u})/\partial x$ evaluated at x_j that is

$$\frac{\hat{\mathbf{f}}_{\mathbf{j+1/2}} - \hat{\mathbf{f}}_{\mathbf{j-1/2}}}{\Delta x} = \left.\frac{\partial \mathbf{f}(\mathbf{u})}{\partial x}\right|_{x=x_j} + \mathcal{O}(\Delta x^r). \tag{3.43}$$

This step is not needed in schemes up to second order because of the adopted central approximation to the derivative of the flux which is correct up to second order so that $\hat{\mathbf{f}}_{\mathbf{j+1/2}}$ can be taken equal to the inter-cell flux $\mathbf{f_{j+1/2}}$.

In schemes of higher order the numerical flux function is computed by combining the value of the inter-cell fluxes $\mathbf{f_{j+1/2}}$ in the stencils shown in Figure 3.7 as follows

$$\hat{\mathbf{f}}_{\mathbf{j+1/2}} = d_0 \mathbf{f_{j+1/2}} + d_2 \Delta^{(2)} \mathbf{f_{j+1/2}} + d_4 \Delta^{(4)} \mathbf{f_{j+1/2}} \tag{3.44}$$

where

$$\Delta^{(2)} \mathbf{f_{j+1/2}} \equiv \mathbf{f_{i-1/2}} - 2\mathbf{f_{j+1/2}} + \mathbf{f_{j+3/2}} \tag{3.45}$$

and

$$\begin{aligned} \Delta^{(4)} \mathbf{f_{j+1/2}} \equiv \quad & \Delta^{(2)} \mathbf{f_{j-1/2}} - 2\Delta^{(2)} \mathbf{f_{j+1/2}} + \Delta^{(2)} \mathbf{f_{j+3/2}} \\ = \, & \mathbf{f_{j-3/2}} - 4\mathbf{f_{j-1/2}} + 6\mathbf{f_{j+1/2}} - 4\mathbf{f_{j+3/2}} + \mathbf{f_{j+5/2}} \end{aligned} \tag{3.46}$$

are numerical estimates of second and fourth derivative, respectively, of the flux at $x_{j+1/2}$.

The coefficients of the combination d_0, d_2 and d_4, listed in Table 3.4 (panel c), can be then easily obtained by expanding in Taylor series the left-hand-side of equation (3.43), where the values $\hat{\mathbf{f}}_{\mathbf{j+1/2}}$ and $\hat{\mathbf{f}}_{\mathbf{j-1/2}}$ are given by equation (3.44) with the appropriate indexes, and by matching that expansion with the requested approximation of order r of the flux derivative (see Del Zanna et al. 2007, Appendix A.3 for details). The derivation of

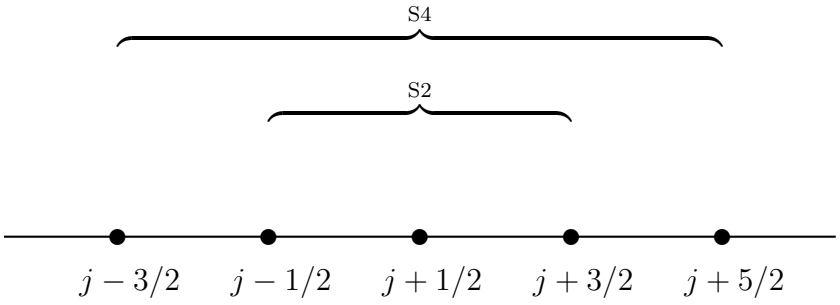

Figure 3.7: Central stencils used for high-order flux corrections. The stencil S2 is used in third order scheme, while WENO5 scheme employs both S2 and S4.

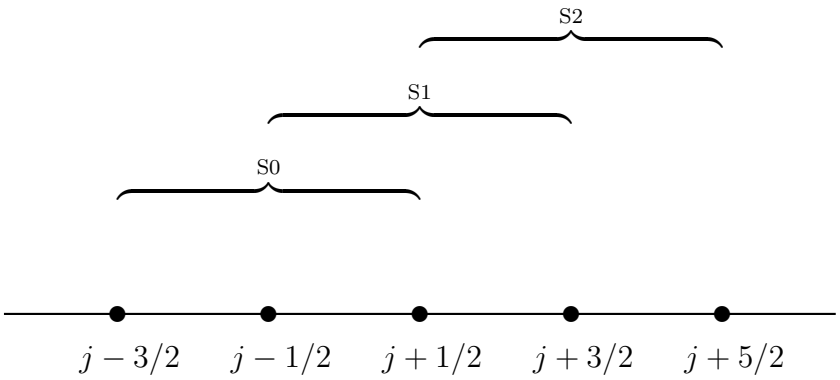

Figure 3.8: The three stencils used for non-oscillatory, high-order flux corrections in CENO3 and WENO3 schemes.

these coefficients shows that in third order schemes only correction of the form (3.45) are needed, while in the WENO5 case both (3.45) and (3.46) must be employed.

It should be noticed that in the procedure just presented for the high-order corrections of the flux derivative, only symmetric stencils (i.e. stencil centered at $x_{j+1/2}$) have been considered. However, non-oscillatory correction algorithms may be also employed, in a way similar to what has been done in Section 3.4.1. In the current version of the code, non-

oscillatory methods are implemented only for third order schemes (WENO3 and CENO3) as follows. Three approximation for the second derivative of the form (3.45) are computed in the stencils shown in Figure 3.8. Successively, a CENO-based selection technique (see Section 3.4.1) is applied between these approximations and the linear interpolant $\bar{L} = 0$. In this way, in the regions where the approximations of the second derivative have the same sign the smoothest, in the CENO sense, is selected and the correction applied following equation (3.44) (with $d_4 = 0$, since the schemes are third order), while in the other regions the linear interpolant is selected and thus the correction is not applied at all (see Del Zanna & Bucciantini 2002).

3.5 Gas cooling

This Section describes the implementation of the radiative cooling module in ECHO++. This module was not originally included in the code, and its implementation represents the most important part of the programming work carried out in the present PhD project.

Radiative cooling of the gas introduces in the energy conservation equation (3.3) the source term

$$S_E = -n_e n_i \Lambda(T, Z), \tag{3.47}$$

where n_e and $n_t = \sum n_i$ are the number density of electrons and ions (summed over all the chemical species n_i), respectively, and $\Lambda(T, Z)$ is the so-called cooling function depending on both temperature T and metallicity Z. S_E is the rate of energy lost by the fluid per unit volume as a consequence of the emission of radiation. In our implementation, the collisional ionization equilibrium cooling function of Sutherland & Dopita (1993) was adopted. Two examples of this cooling function, normalised to a hydrogen number density of $n_{\mathrm{H}} = 1\,\mathrm{cm}^{-3}$, for two different values of Z are presented in Figure 3.9. In particular, from the figure it can be appreciated the strong impact of the metal content of the gas on its cooling rate.

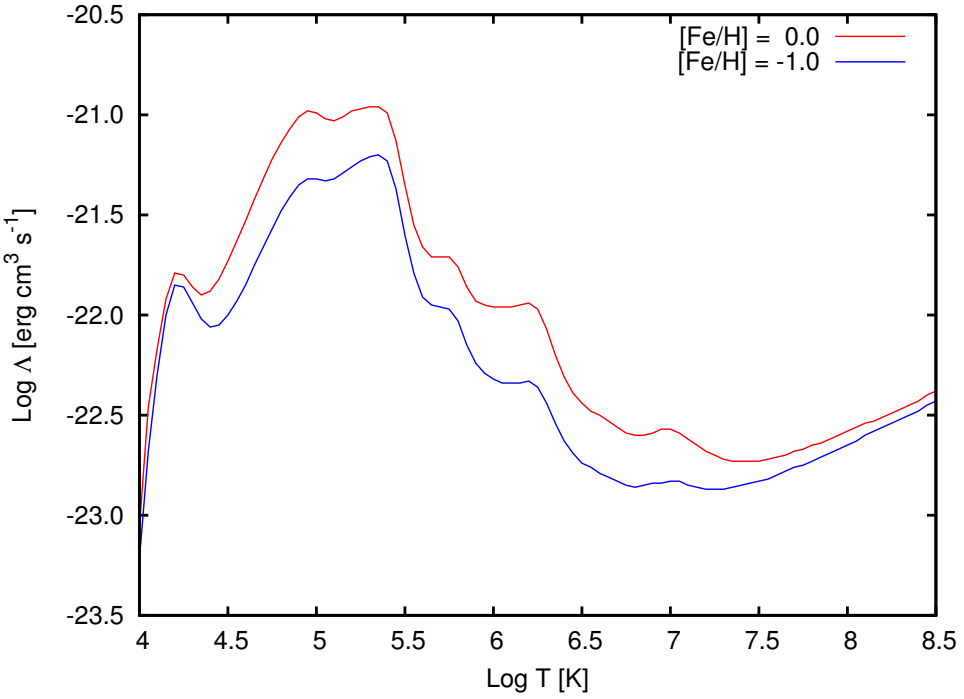

Figure 3.9: Examples of cooling functions with different metal contents (from Sutherland & Dopita 1993). The curves are normalised to a hydrogen number density of $n_{\rm H} = 1\,{\rm cm}^{-3}$. The metallicity of the gas is indicated as [Fe/H] $\equiv$ Log$(Z/Z_\odot)$, that is the logarithm of gas metallicity in solar units.

In the current version of the code the cooling term (3.47) is directly added to the energy flux, so that the time integration schemes (3.9) and (3.10) can be reused. The explicit (time integration) treatment of the cooling allows a simpler and straightforward implementation of the module, but it is not necessarily the most efficient strategy for all the problems. In fact, radiative cooling is a *stiff* source term, in the sense that the cooling timescale can be much different from the timescale associated to hydrodynamic processes. This can cause problems in regions in which cooling is particularly effective, because the cooling time of the gas

$$t_{\rm cool} = \frac{P}{(\gamma - 1) n_e n_t \Lambda(T, Z)}, \tag{3.48}$$

that is the ratio between the internal energy of the gas and its cooling rate,

is much smaller than hydrodynamic time-step (3.11), and the value of the latter must be limited to a fraction of $t_{\rm cool}$ (in the code fixed to 10%) for stability reasons. In particular, the values of the time-step required for stability can be so small that their use is not practical. However, this is not the case of the investigations presented in Chapters 4 and 5, where gas at very low densities is studied and, therefore, an explicit time-integration scheme for the cooling is viable. To extend the domain of applicability of the code, other integration strategies for the radiative cooling will be considered for future implementations.

To determine the values of the cooling rate at the cell centers, needed by the TVD-RK schemes (3.9) and (3.10), the following procedure was adopted. As a preliminary step, since the code works with the mass density of the fluid ρ, rather than the number densities of electrons and ions, equation (3.47) was recast as

$$n_e n_t \Lambda(T,Z) = \rho^2 \frac{x(T,Z)}{[1+x(T,Z)]^2 \mu(T,Z)^2} \Lambda(T,Z). \tag{3.49}$$

In the previous equation $x(T,Z) \equiv n_t/n_e$ and the mean molecular weight of the gas $\mu(T,Z)$ is given by

$$\mu(T,Z) = \sum_{i}^{species} \frac{n_i m_i}{n_t + n_e}, \tag{3.50}$$

where n_i is the number density of the species i, m_i its mass and the sum is taken over all the species, electrons included. Successively, the expression

$$\tilde{\Lambda}(T,Z) \equiv \frac{x(T,Z)}{[1+x(T,Z)]^2 \mu(T,Z)^2} \Lambda(T,Z) \tag{3.51}$$

was interpolated (linearly in logarithmic scale) on a grid, consisting of N_T+1 equally spaced points in the temperature interval $\mathrm{Log}\, T \in [4, 8.5]$ and N_Z+1 equally spaced points in the metallicity interval $\mathrm{Log}(Z/Z_\odot) \in [-3.0, 0.0]$, in the logarithmic temperature-metallicity plane ($Z_\odot$ is the value of the solar metallicity). The temperature and metallicity intervals over which equation (3.51) is interpolated are those treated in Sutherland & Dopita

(1993). The peculiar case of a plasma that does not contain metals is treated separately. We fixed $N_T = 10^4$ and $N_Z = 50$ to have a good coverage of the $\mathrm{Log}\, T - \mathrm{Log}(Z/Z_\odot)$ plane. The two grids are constructed as

$$\mathrm{Log}\, T_i = \mathrm{Log}\, T_{\mathrm{min}} + i \times \Delta\mathrm{Log}\, T, \qquad i = 0, \ldots, N_T, \tag{3.52}$$

$$\mathrm{Log}\, Z_s = \mathrm{Log}\, Z_{\mathrm{min}} + s \times \Delta\mathrm{Log}\, Z, \qquad s = 0, \ldots, N_Z, \tag{3.53}$$

where $\mathrm{Log}\, T_i$ is the value of the temperature on the grid point i, $\mathrm{Log}\, T_{\mathrm{min}}$ is the lower end of the temperature interval, $\Delta\mathrm{Log}\, T = (\mathrm{Log}\, T_{N_T} - \mathrm{Log}\, T_{\mathrm{min}})/N_T$ and the same applies, with the due changes of notation, to the case of the metallicity. All the quantities on the right-hand-side of equation (3.51) are known and tabulated in Sutherland & Dopita (1993). After the construction of this grid of interpolated values for $\tilde{\Lambda}(T, Z)$, the gas cooling rate at any given cell center is computed as follows.

(i) The point value of the gas metallicity at the cell center is determined (see Section 3.6 for the treatment of a gas with metallicity varying with the position). This value is indicated as $\tilde{Z}$.

(ii) The index $\tilde{s}$ corresponding to $\tilde{Z}$ in the interpolation grid of the metallicity is computed as

$$\tilde{s} = \mathrm{floor}\left(\frac{\mathrm{Log}\, \tilde{Z} - \mathrm{Log}\, Z_{\mathrm{min}}}{\Delta\mathrm{Log}\, Z}\right), \tag{3.54}$$

(see equation [3.53]), where $\mathrm{floor}(x) = \max\{m \in \mathrm{N} \mid m \leq x\}$

(iii) The temperature of the gas is computed. However, since the mean molecular weight of the gas depends on the temperature, its value $\tilde{T}$ is the solution of the following equation

$$\frac{P}{\rho} - \frac{kT}{\mu(T, Z_{\tilde{s}})} = 0. \tag{3.55}$$

In equation (3.55), which is the equation of state for an ideal gas, the function $\mu(T, Z)$ is interpolated on the same grid used for $\tilde{\Lambda}(T, Z)$, k

is the Boltzmann constant and ρ and P are the values of the density and pressure at the cell center, respectively. The root $\tilde{T}$ is obtained by the application of the secant method.

(iv) An operation analogous to that at point (ii) is carried out for $\tilde{T}$. In this way the index $\tilde{i}$ is determined.

(v) With the values of the metallicity and temperatures computed above, the gas cooling rate $-\rho^2\tilde{\Lambda}(T_{\tilde{i}}, Z_{\tilde{s}})$ is obtained and added to the energy flux. ρ represents, again, the value of the density at the cell center.

3.6 Advection of passive scalars

Any scalar field α advected by the fluid flow, that does not influence evolution of this latter from a dynamical point of view, is called passive scalar. Their primary use in the context of hydrodynamic simulations is to trace how peculiar properties of the fluid, such as (chemical) composition, are redistributed by the dynamics of the flow. In the code, advection of passive scalar fields is introduced to treat the case of two gas phases at different metallicities. This feature is rather important in the simulations, that will be presented in the next Chapters, of the interaction between fountain clouds and cosmological hot coronae.

To see how the advection of passive scalars is implemented into the code, consider the case of a scalar field α, representing, for instance, the metallicity of the gas Z in solar units as in the simulations in Chapter 4 and 5, that obeys the advection equation

$$\frac{D\alpha}{Dt} = 0 \tag{3.56}$$

where

$$\frac{D}{Dt} \equiv \frac{\partial}{\partial t} + \mathbf{v} \cdot \nabla \tag{3.57}$$

is called *lagrangian* or material derivative. It is possible to recast equation (3.56) in conservative form, by using the equation of the conservation

of mass (3.1), as

$$\frac{\partial \rho\alpha}{\partial t} + \nabla \cdot \rho\alpha\mathbf{v} = 0. \tag{3.58}$$

In the form (3.58), the advection equation can be integrated, together with the equation of hydrodynamics (3.1), (3.2) and (3.3), in a straightforward way with the methods that were illustrated in Section 3.4. Moreover, to make the code as general as possible, the implementation of passive scalars advection is able to deal with an arbitrary number of scalar fields.

3.7 Code testing

In this Section, to show the ability of the code to deal with discontinuous initial data and to capture and resolve discontinuities, three tests problems are presented. The first two are classical one-dimensional tests for hydrodynamical codes, namely the Sod shock tube problem (Sod 1978) and the Lax problem (Lax 1954), while the third is a two-dimensional test concerning the development of the Kelvin-Helmholtz instability (Helmholtz 1868; Kelvin 1871). For each test the WENO3 scheme is used as a spatial reconstruction algorithm, coupled with the third order RK-TVD scheme for the temporal evolution. All the tests are simulated with both the Riemann solvers presented in Section 3.4.2 at two different resolutions, in order to compare their performances as this latter varies.

The first test that we present is the Sod (1978) shock tube problem. It is a one-dimensional Riemann problem for the Euler equations in the computational domain $x \in [0, 1]$, whose initial conditions are given by

$$\begin{pmatrix} \rho_L \\ v_L \\ P_L \end{pmatrix} = \begin{pmatrix} 1.0 \\ 0.0 \\ 1.0 \end{pmatrix} \quad x \leq 0.5; \qquad \begin{pmatrix} \rho_R \\ v_R \\ P_R \end{pmatrix} = \begin{pmatrix} 0.125 \\ 0.0 \\ 0.1 \end{pmatrix} \quad x > 0.5, \tag{3.59}$$

and the adiabatic index γ is fixed to 1.4. The solution of this problem after $t = 0.2$ is presented in Figures 3.10 (density), 3.11 (pressure) and 3.12 (velocity). In each figure top panels show the low-resolution run (100 grid points), whilst in bottom panels the number of grid points is doubled.

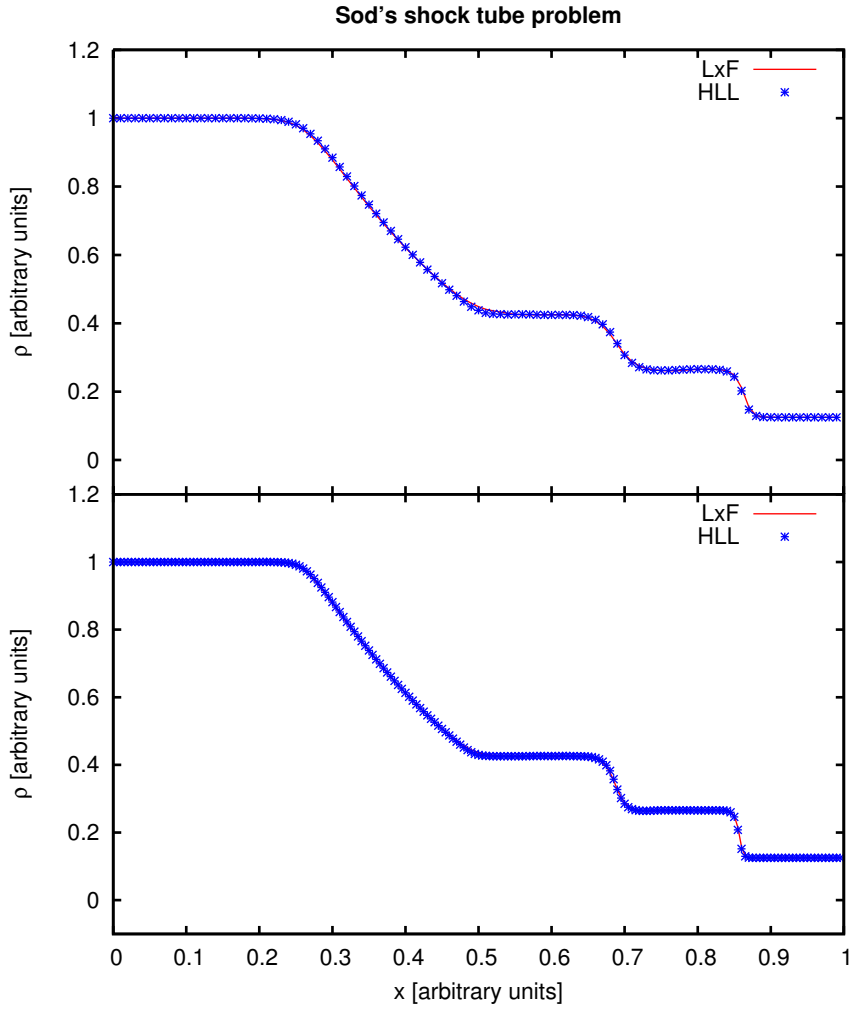

Figure 3.10: Comparison of the performances of the two Riemann solvers implemented in the code for the Sod's shock tube problem problem. The gas density at $t = 0.2$ is shown for 100 (top panel) and 200 grid points (bottom panel). For the spatial reconstruction the WENO3 scheme was used, coupled with the third order TVD-RK scheme for the temporal evolution.

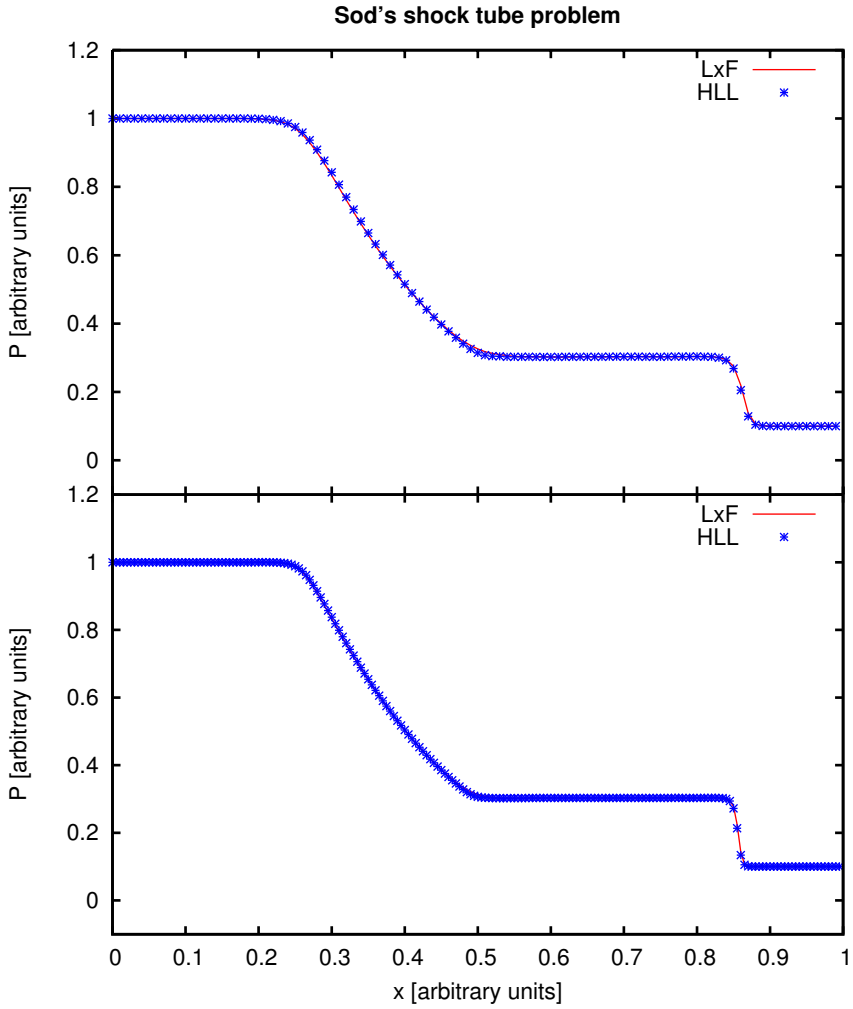

Figure 3.11: The same as in Figure 3.10 but for the pressure.

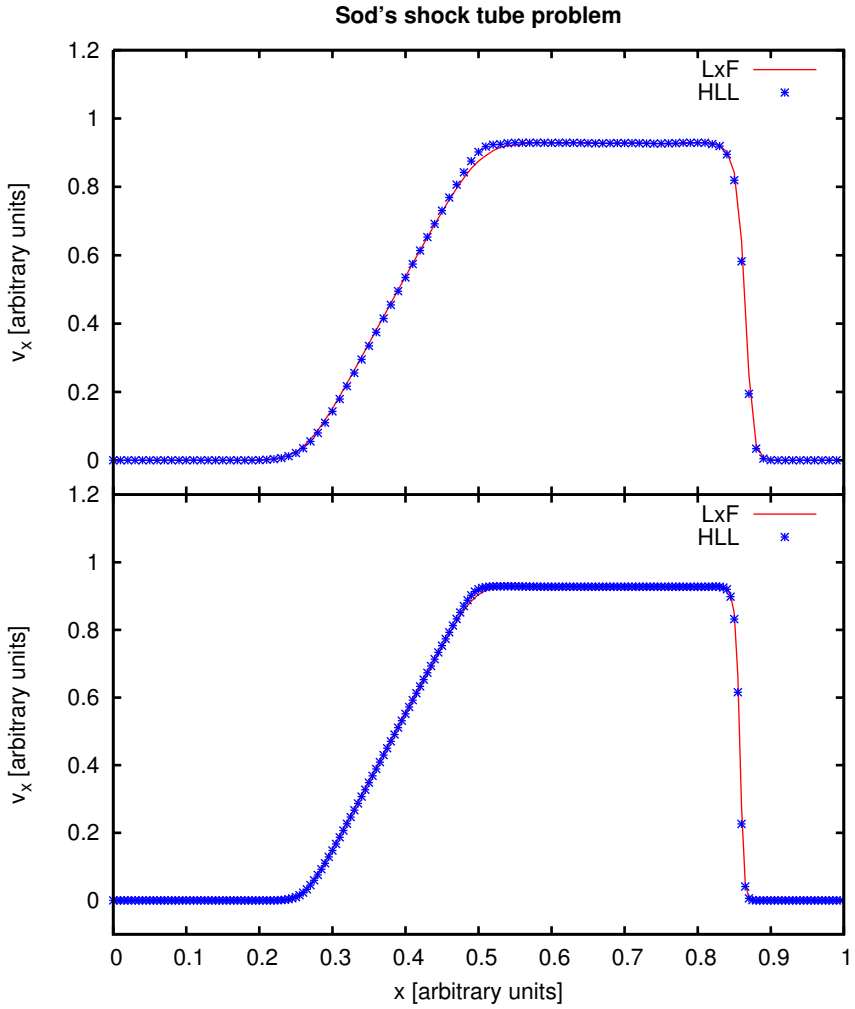

Figure 3.12: The same as in Figure 3.10 but for the velocity along the x axis.

The solution of the Sod test (3.59) is composed by three constant states connected by, starting from left in each figure, a rarefaction wave[5], a contact discontinuity (characterised by the fact that the jump is present in the density only, see Figure 3.10) and a (weak) shock. By comparing the results obtained with the LxF solver (red line in the figures) and the HLL (blue stars) solver, it can be seen that, as expected, the LxF solver is slightly more diffusive – meaning that the discontinuities are more smeared – than the HLL solver at low resolution. If the number of grid points is increased, the two solvers achieve comparable performances and, from the figures, no appreciable differences in the smearing of the discontinuities is detected.

The other test that we discuss is the Lax problem (Lax 1954). This test is again a one-dimensional Riemann problem for the Euler equations, in the computational domain $x \in [0, 1]$ and for $\gamma = 1.4$, with initial conditions given by

$$\begin{pmatrix} \rho_L \\ v_L \\ P_L \end{pmatrix} = \begin{pmatrix} 0.5 \\ 0.0 \\ 0.571 \end{pmatrix} \quad x \leq 0.5; \qquad \begin{pmatrix} \rho_R \\ v_R \\ P_R \end{pmatrix} = \begin{pmatrix} 0.445 \\ -0.698 \\ 3.528 \end{pmatrix} \quad x > 0.5. \tag{3.60}$$

The density after $t = 0.2$ for this problem is presented in Figure 3.13 in the low-resolution (top panel, 100 grid points) and in the high-resolution case (bottom panel, 200 grid points). The structure of the solution is similar to the Sod problem: there are three constant states connected by a shock (at $x \sim 0.1$), a contact discontinuity (at $x \sim 0.3$) and a rarefaction wave (in the region $0.75 \lesssim x \lesssim 0.9$). The shock present in the solution is rather strong and, for this reason, this test case is quite demanding for numerical schemes, as oscillations can easily form. Figure 3.13 show, however, that the code is able to resolve (and no spurious oscillations are detected) all the features of the solution independently from the solver used. Again the LxF solver is slightly more diffusive than the HLL solver (especially in the contact discontinuity), but in the high-resolution run the results obtained

[5] A rarefaction wave is a smooth (i.e. *continuous*) transition between two constant states, see Toro (1999) pag. 73

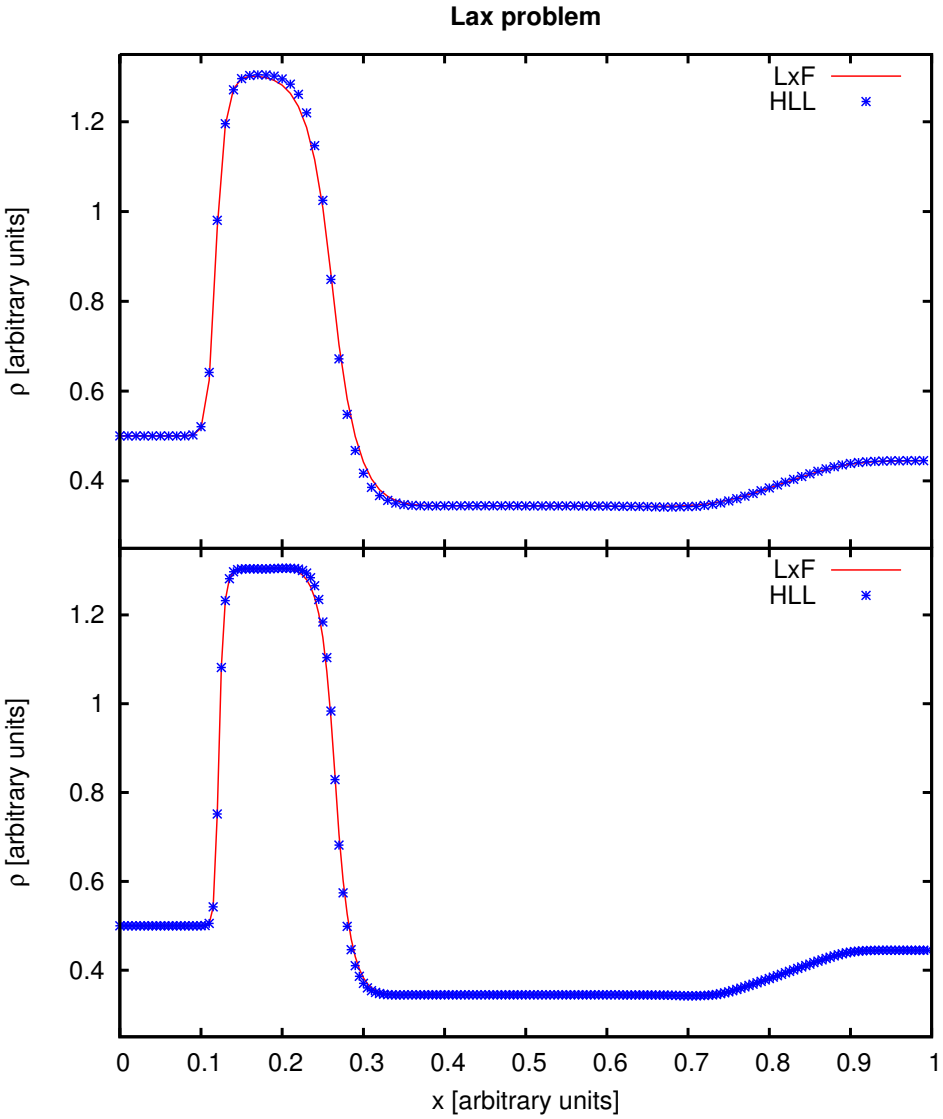

Figure 3.13: Comparison of the performances of the two Riemann solvers implemented in the code for the Lax problem. The gas density at $t = 0.2$ is shown for 100 (top panel) and 200 grid points (bottom panel). For the spatial reconstruction the WENO3 scheme was used, coupled with the third order TVD-RK scheme for the temporal evolution.

with both solvers agree remarkably well.

As a final test a two-dimensional problem, the development of Kelvin-Helmholtz instability (Helmholtz 1868; Kelvin 1871), is presented. This fluid instability appears whenever a perturbation is introduced at the interface between two shearing fluids (i.e. in a tangential discontinuity). To simulate this process, in the computational domain $(x, y) \in [0, 1] \times [0, 1]$ the following initial set up was adopted

$$\begin{pmatrix} \rho \\ v_x \\ v_y \\ P \end{pmatrix} = \begin{pmatrix} 2.0 \\ 0.5 \\ 0.0 \\ 2.5 \end{pmatrix} \quad |y| \leq 0.25; \qquad \begin{pmatrix} \rho \\ v_x \\ v_y \\ P \end{pmatrix} = \begin{pmatrix} 1.0 \\ -0.5 \\ 0.0 \\ 2.5 \end{pmatrix} \quad |y| > 0.25, \tag{3.61}$$

with γ again fixed at 1.4. At the two tangential discontinuities, located at $y = \pm 0.25$, v_y is perturbed as

$$\delta v_y = \pm 0.025 \sin\left[4\pi(x + 0.5)\right], \tag{3.62}$$

(the sign refers to the location of the interfaces between the two fluids) on a stripe centered at the discontinuity and large 0.0125. Due to the instability of this configuration, ripples at the interfaces between the fluids appear. In particular, the sinusoidal form of equation (3.62), with period 1/2, excite the formation of two vortices in the solution. The density map for this test after $t = 2.0$ is shown in Figure 3.14 for the LxF (upper panels) and the HLL (lower panels) solvers. For each Riemann solver two runs were performed: a low-resolution run on a grid of 200x200 grid points (left panel) and a high-resolution run with twice the grid point in both the spatial directions (right panel). The code, even in the low-resolution run, is able to capture the formation and the development of the two vortices. Again, in the low-resolution run, the HLL solver is slightly less diffusive than the LxF solver – small-scale structures in the solution, and in particular, at the centre of the vortices are more defined. In the simulations at the highest resolution no appreciable differences are seen in the solution by changing the Riemann solver. The fact that the code is able to correctly model the development

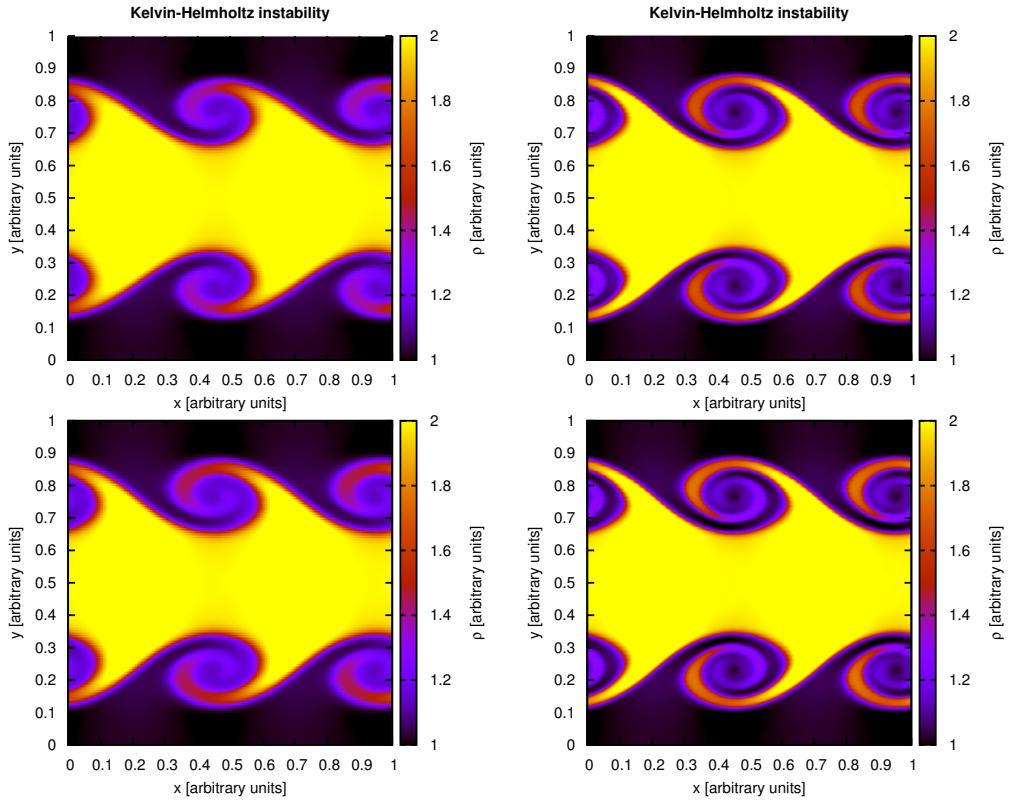

Figure 3.14: Resolution study for the Kelvin-Helmholtz instability simulated with the LxF (top panels) and the HLL (bottom panels) approximate Riemann solvers. Low-resolution simulations (left column) were carried out on a grid of 200x200 points, while in high-resolution simulations (right column) the number of grid point in each spatial direction was doubled. All the snapshots were taken at $t = 2.0$. The WENO3 scheme, coupled again with the third order TVD-RK scheme for the temporal evolution, was used for the spatial reconstruction.

of the Kelvin-Helmholtz instability is crucial for the topic of this Thesis, because this instability plays an important role in the process of mass and momentum exchange, between the cold extra-planar gas clouds and the hot cosmological corona, which is discussed in Chapters 4 and 5.

4

Cooling of the hot corona

4.1 Introduction

As we have already seen in Chapter 2, the dynamical state of the cold extra-planar gas, and in particular its vertical velocity gradient, cannot be reproduced by stationary (Jeans) models that assume that the particles (clouds) of this gas move on almost ballistic trajectories in the halo region. This result is also found if one considers purely ballistic galactic fountain models (e.g. Fraternali & Binney 2006), and seems to suggest that fountain clouds must interact with an ambient medium in order to lose part of their angular momentum. For instance, Fraternali & Binney (2008) have shown that the kinematics of the neutral extra-planar gas can be accounted for if fountain clouds accrete gas from an ambient medium, which must have a low specific angular momentum with respect to the galaxy spin axis, at a rate close to the star formation rate of the galaxy.

Next question is represented by the nature of the ambient medium the fountain is supposed to interact with. Cosmology strongly suggests, on the basis of a combination of big-bang nucleosynthesis theory and observations of the cosmic microwave background (e.g. Fukugita & Peebles 2004;

Komatsu et al. 2009), that galaxies should be embedded in extended virial-temperature atmospheres called coronae. These coronae are thought to contain most ($\gtrsim 50\%$) of the baryons originally associated with the galaxy's dark matter halo. So far, a direct detection in the soft X-ray band of this hot ($T \gtrsim 10^6\,\mathrm{K}$) gas phase in low density environment has proven to be elusive and this is probably due to the fact that galactic coronae are characterised by an X-ray surface brightness below the sensitivity of the current instrumentation (Rasmussen et al. 2009). However, in our Galaxy there is plenty of (indirect) evidence for the existence hot coronal gas such as, for instance, the presence of highly ionised material detected in UV absorption spectroscopy (Spitzer & Jenkins 1975; Sembach et al. 2003) and the head-tail morphology of individual high-velocity clouds (Brüns et al. 2001; Westmeier et al. 2005). Unfortunately, it is extremely difficult to extract from the available data reliable information about important properties of the corona, such as density distribution and kinematics (Anderson & Bregman 2010).

In the region within a few kiloparsecs from the galactic disc, where most of H I extra-planar gas is located, the fountain clouds should be travelling through the ubiquitous coronal gas, and thus an interaction between the two phases, which affects the kinematics of both, is inevitable. An interesting aspect of this interaction process is represented by the possibility of mass and momentum exchange between the two phases. In this Chapter the exchange of mass between the fountain clouds and the corona is investigated, while the momentum transfer is the topic of Chapter 5.

The importance of the exchange of mass between the cold fountain clouds and the corona is represented by the fact that star-forming disc galaxies, such as the Milky-Way, need to accrete $\sim 1\,\mathrm{M}_\odot$ of gas each year (e.g. Pagel 1997; Chiappini et al. 2001; Sancisi et al. 2008, and references therein), in order to sustain their star formation. There is much debate about the reservoir from which this gas is drawn, but the persistent failure of 21-cm surveys to identify significant bodies of intergalactic H I in

the nearby Universe (Lo & Sargent 1979; Pisano et al. 2004; Kovač et al. 2009) suggests that most of the accretion comes in a hidden form (Fraternali 2010). Our premise in this Chapter is that the gas, which is needed to sustain star formation in the disc, must be drawn from the corona at virial temperature that surrounds the galaxy. This premise is justified by the fact that coronae are the only cosmologically significant reservoir of gas capable of sustaining an accretion rate of $\sim 1\,\mathrm{M}_\odot\,\mathrm{yr}^{-1}$ for a Hubble time.

In the present Chapter we discuss the results of hydrodynamical simulations of a cold cloud travelling, with an assigned initial velocity, through a homogeneous hot medium representing the hot corona. The simulations are performed with the hydrodynamical code described in Chapter 3. The most important result is that, for densities and metallicities that may be considered typical of disc galaxies, coronal gas can efficiently condense in the turbulent cloud wake, which forms as a consequence of the interaction. The rate at which coronal gas condenses, extrapolated to the whole halo of a typical star-forming galaxy, is close to that required to sustain star formation. Thus, we argue that it is likely that this cooled coronal gas is shortly thereafter accreted by the disc, becoming the fuel out of which disc galaxies form stars.

The results of this Chapter have been published in paper form in Marinacci et al. (2010a).

4.2 Analytic arguments

Before presenting the main results of the simulations, in the subsections that follow we give a series of analytical arguments, supporting the scenario that cloud-corona interaction must ultimately lead to cooling of the coronal gas rather than evaporation of H I clouds.

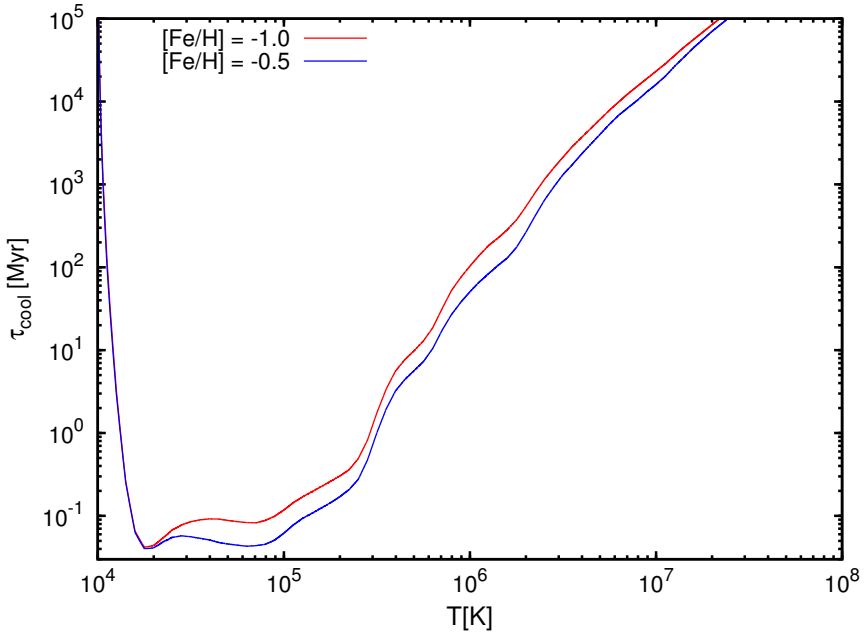

Figure 4.1: Cooling time using Sutherland & Dopita (1993) cooling curve for [Fe/H] $= -1$ and -0.5 for material in pressure equilibrium with coronal gas with $T = 1.8 \times 10^6$ K and $n_e = 2.6 \times 10^{-3}\,\mathrm{cm}^{-3}$.

4.2.1 Cooling rates

As was mentioned above, with the current available data it is not possible to accurately determine the density distribution of the corona. However, there are indications that density of galactic coronae are in a range such that their local cooling time is of the order of a gigayear in regions near the star-forming disc (Anderson & Bregman 2010). The orbital time of the fountain clouds is ~ 100 Myr (e.g. Fraternali & Binney 2006), and therefore, if coronal gas is to be accreted by the disc due to the interaction with the fountain, the cooling time of the corona has to be lowered to values close to the orbital time of the clouds.

Fukugita & Peebles (2006) have developed models for massive coronae around spiral galaxies by assuming that these coronae have a baryon mass fraction close to the cosmic mean. In their model 2 the density of the corona decreases with radius as $r^{-3/2}$ and at 10 kpc has electron density

$n_{\rm e} = 2.6 \times 10^{-3}\,{\rm cm}^{-3}$. The corona is isothermal with $T_{\rm cor} = 1.8 \times 10^6\,{\rm K}$. Figure 4.2 shows the cooling time of gas with metallicities [Fe/H][1] $= -1$ and -0.5 that is in pressure equilibrium with plasma of this temperature and the mean density of this corona between 8 and 12 kpc. At $T \sim 2 \times 10^6\,{\rm K}$, the cooling time is $\sim 300\,{\rm Myr}$. Once the temperature has fallen to $5 \times 10^5\,{\rm K}$, the cooling time has dropped by nearly forty to $\sim 8\,{\rm Myr}$, which is less than the dynamical time at the solar galactocentric radius, R_0. By the time the temperature has dropped by a further factor of two to $2.5 \times 10^5\,{\rm K}$, the cooling time has fallen by more than a further order of magnitude and is a mere 0.4 Myr. Thus although the cooling time of ambient gas in the lower corona is long, any diminution in temperature will dramatically shorten it.

The mass of the H I halo is rather ill-defined: in external galaxies it is not clear at what value of $|z|$ the boundary between disc and halo H I should be placed, and in the Galaxy there is a similar ambiguity in the line-of-sight velocity that divides halo from disc H I. In NGC 891 if the disc-halo boundary is conservatively placed at 1.3 kpc, the mass of the H I halo is $\sim 6 \times 10^8\,{\rm M}_\odot$ (Fraternali & Binney 2006). Kalberla & Dedes (2008) conclude that ~ 10 per cent of the Galaxy's H I is halo gas, and that the total H I mass within $R = 12\,{\rm kpc}$ (the region within which most star formation occurs) is $4.5 \times 10^9\,{\rm M}_\odot$, so the mass of the H I halo within 12 kpc is $\sim 4.5 \times 10^8\,{\rm M}_\odot$, a value consistent with more recent determinations (Marasco & Fraternali 2011).

The H I halo is largely confined to the region $|z| < 5\,{\rm kpc}$, so the mass of the H I halo at $R < 12\,{\rm kpc}$ must be compared to the mass of coronal gas in the cylindrical annulus $4\,{\rm kpc} \leq R \leq 12\,{\rm kpc}$, $|z| < 5\,{\rm kpc}$. The coronal mass, assuming a mean density of $10^{-3}\,{\rm cm}^{-3}$ (see Section 4.3.1), is $\sim 2 \times 10^8\,{\rm M}_\odot$, so within this volume there is over twice as much H I as coronal gas. The H I is likely distributed in clouds or filaments (small filling factor f) while the coronal gas will occupy nearly all the space ($f \sim 1$).

[1]Recall that [Fe/H] $\equiv {\rm Log}(Z/Z_\odot)$, that is the logarithm of gas metallicity in solar units.

The clouds that make up the H I halo typically take 100 Myr to travel from their launch point in the plane through the halo and back to the plane. Consequently, in one gigayear $\sim 4.5 \times 10^9$ of H I passes through the $2 \times 10^8\,\mathrm{M}_\odot$ of gas in the lower corona. Hence the temperature of the coronal gas would be halved if just 4.5 per cent of the gas that passes through the corona in 1 Gyr were to mix with the coronal gas. This drop in temperature would bring the cooling time of the coronal gas down to ~ 0.1 Gyr, the local orbital time.

4.2.2 Implications of momentum

The H I clouds of the halo plough through the corona at speeds v that are less than but comparable to the sound speed of the coronal gas. Consequently the flow around these clouds is likely to be in a high Reynolds number regime, and each cloud must be decelerated by ram pressure of order $\rho_{\rm cor}v^2$, where $\rho_{\rm cor}$ is the coronal density. In these circumstances the cloud loses its momentum on a timescale equal to $\rho_{\rm cl}/\rho_{\rm cor}$ times the time $t_{\rm cl}$ for the cloud to move its own length (Fraternali & Binney 2008). Clouds have diameters of a few tens of parsecs and travel a few kiloparsecs, while $\rho_{\rm cl}/\rho_{\rm cor} \simeq 200$. Hence clouds must surrender a significant fraction of their momentum to coronal gas (Benjamin 2002). Above it was shown that in a gigayear $\sim 4.5\times10^9\,\mathrm{M}_\odot$ of H I passes through the $2\times10^8\,\mathrm{M}_\odot$ of the lower corona. Clearly the coronal gas cannot absorb a significant fraction of the momentum of more than 20 times its mass of H I (Fraternali & Binney 2008). Moreover, if the H I disc were losing angular momentum to the corona at the rate this calculation implies, it would be contracting on a gigayear timescale. The natural resolution of these problems is that the disc *accretes* most of the coronal gas that H I clouds encounter. Then the momentum lost by H I clouds would be returned to the disc, and it would not build up in the corona. All the aspects concerning the momentum transfer between the galactic fountain clouds and the corona and their implications for the dynamics of both phases will be the topic of the next Chapter.

4.2.3 The wake of a typical cloud

As a cloud moves through the ambient coronal gas, turbulence in the boundary layer at the interface of the hot and cold fluids must cause gas to be stripped from the cloud at some rate. To calculate this rate from ab-initio physics is extremely difficult because plasma instabilities would have to be considered in addition to hydrodynamical ones, such as the Kelvin-Helmholtz instability. In view of these difficulties, the problem can be simplified by hypothesising that mass is stripped from the a cloud of mass $M_{\rm cl}$ at a rate $\alpha M_{\rm cl}$.

A turbulent wake of stripped gas will run back through the corona from the moving cloud. In this wake turbulence will mix the stripped gas with ambient gas. A key quantity is the cooling time of the plasma that results from this mixing. This quantity can be estimated under the assumption that cloud and coronal gases mix so quickly that radiative losses during mixing can be neglected.

Let s be a short length of the wake, which has cross-sectional area $A_{\rm w}$ and originally contained a mass $A_{\rm w} s \rho_{\rm cor}$ of coronal gas. In the time s/v that it took the cloud to pass through the length, a mass $\alpha M_{\rm cl} s/v$ of gas was stripped from it. After the cold gas has mixed and come into thermal equilibrium with the coronal gas, the temperature of the resulting fluid is

$$T_{\rm m} = \frac{A_{\rm w}\rho_{\rm cor}T_{\rm cor} + \alpha M_{\rm cl}T_{\rm cl}/v}{A_{\rm w}\rho_{\rm cor} + \alpha M_{\rm cl}/v}, \tag{4.1}$$

where $T_{\rm cor}$ and $T_{\rm cl}$ are the coronal and cloud temperatures, respectively.

The natural unit for the cross-sectional area of the wake is the characteristic cross section $(M_{\rm cl}/\rho_{\rm cl})^{2/3}$ of the cloud that can be written as $A_{\rm w} = \beta(M_{\rm cl}/\rho_{\rm cl})^{2/3}$, where $\beta \sim 1$. Thus

$$T_{\rm m} = \frac{\beta(M_{\rm cl}/\rho_{\rm cl})^{2/3}\rho_{\rm cor}T_{\rm cor} + \alpha M_{\rm cl}T_{\rm cl}/v}{\beta(M_{\rm cl}/\rho_{\rm cl})^{2/3}\rho_{\rm cor} + \alpha M_{\rm cl}/v}. \tag{4.2}$$

This expression may be simplified under the assumption that the cloud is in approximate pressure equilibrium with the corona, so $\rho_{\rm cor}T_{\rm cor} \simeq \rho_{\rm cl}T_{\rm cl}$,

obtaining

$$T_{\rm m} = \frac{1 + (M_{\rm cl}/\rho_{\rm cl})^{1/3}\alpha/\beta v}{1 + (M_{\rm cl}/\rho_{\rm cl})^{1/3}(T_{\rm cor}/T_{\rm cl})\alpha/\beta v}\, T_{\rm cor}. \tag{4.3}$$

Since $(M_{\rm cl}/\rho_{\rm cl})^{1/3}\alpha/v$ is the fraction of the cloud's mass that is stripped in the time taken for the cloud to travel its own length, and $\beta \sim 1$, the second term in the numerator of equation (4.3) must be small compared to unity and may be neglected. The second term in the denominator is larger by a factor $T_{\rm cor}/T_{\rm cl} \gtrsim 200$, so $T_{\rm m}$ may be significantly lower than $T_{\rm cor}$. On account of the steepness of the cooling-time curve plotted in Figure 4.2, this result implies that the cooling time in the wake may fall below the ambient cooling time by a factor of several.

From this back-of-envelope calculation some interesting facts follow.

- Material in the wake will become H I on the timescale that it takes the parent H I cloud to fly its trajectory if the mass-loss rate α exceeds the critical value

$$\alpha_{\rm crit} \equiv \frac{\beta v}{(M_{\rm cl}/\rho_{\rm cl})^{1/3}}\,\frac{T_{\rm cl}}{T_{\rm cor}}. \tag{4.4}$$

  For $\beta = 1$ this condition is that in the time taken to travel its own length the cloud lose at least a fraction $T_{\rm cl}/T_{\rm cor}$ of its mass or, in other words, since $T_{\rm cl}/T_{\rm cor} = \rho_{\rm cor}/\rho_{\rm cl}$ if pressure equilibrium is assumed, the mass lost by the cloud in the time taken to travel its own length equals the coronal mass contained in a volume of the wake equal to the cloud's volume.

- If the mass-loss rate of clouds falls below this critical value, the mass of gas that is stripped from the cloud will be integrated into the corona. This will lower the cooling time of the ambient corona, but not lead to prompt cooling of the wake. This drop in the temperature of the corona near the disc may lower the critical mass-loss rate required for subsequent wakes to cool promptly.

- $\alpha_{\rm crit}$ was obtained by neglecting radiative cooling during mixing. Although the mixing process is likely to be fast, the cooling rate is

extremely large at temperatures that lie within a factor 30 of the cloud's temperature. Hence, it is likely that a more exact calculation would produce a lower estimate of $\alpha_{\rm crit}$. Compression of the coronal gas as it flows around the cloud was also neglected since only clouds moving through the corona at subsonic speeds were considered in the simulations (the sound speed of the corona is $\sim 230\,{\rm km\,s^{-1}}$ while the initial cloud speed is always fixed at $75\,{\rm km\,s^{-1}}$, see Section 4.3.1).

- The effective value of β is uncertain. On one hand, as the simulations will show, the cloud flattens in its direction of motion, making $\beta > 1$. On the other hand, the distribution of cloud material is likely to be concentrated in a network of thin sheets (see the wake of the cloud in Figure 4.2). The effective value of β for an individual sheet could be small.

- Dimensional analysis indicates that α will lie near $\alpha_{\rm crit}$: the rate of stripping is essentially determined by the rate at which coronal gas hits the leading surface of the cloud and strips a comparable mass from the cloud. Quantitatively, $\alpha M_{\rm cl} \equiv \dot{M}_{\rm cl} = -b\pi r_{\rm cl}^2 \rho_{\rm cor} v$, where $b \sim 1$ and $r_{\rm cl}$ is the cloud radius. By eliminating $r_{\rm cl}$ and $\rho_{\rm cor}$ in favour of $M_{\rm cl}$ and $T_{\rm cor}$, the characteristic mass-loss parameter is

$$\alpha = \left(\frac{9\pi}{16}\right)^{1/3} \frac{b}{\beta}\, \alpha_{\rm crit}. \tag{4.5}$$

- If the mass-loss rate is given by the previous item, then the mass of a cloud that will completely mix with the corona after travelling the distance L

$$L = \left(\frac{16}{9\pi b^3}\frac{M_{\rm crit}}{\rho_{\rm cl}}\right)^{1/3} \frac{T_{\rm cor}}{T_{\rm cl}}. \tag{4.6}$$

  Equivalently, the distance travelled prior to destruction is predicted to be $\sim T_{\rm cor}/T_{\rm cl}$ times the size of the cloud.

4.3 Numerical simulations

Numerical simulations of a cloud of gas at $T \sim 10^4\,\mathrm{K}$ moving through coronal gas at an initial speed $v_0 \sim 75\,\mathrm{km\,s^{-1}}$ will illustrate these points and give insight into both typical mass-loss rates and the critical mass-loss rate required for prompt cooling of the wake. The simulations are idealised in that they neglect gravitational acceleration and the variation of the coronal density along the cloud's trajectory. However, galactic fountain models (Fraternali & Binney 2006, 2008) have shown that the galactocentric radius of the clouds varies by $\lesssim 30$ per cent, so the density variation is not extreme. The range of relevant velocities depends on the extent to which the corona corotates with the disc. The velocity explored by the simulations presented in this Chapter ($75\,\mathrm{km\,s^{-1}}$) is at the low end of the relevant range because, as it will be shown in Chapter 5, this is the expected difference in rotational velocity between the fountain clouds and the coronal gas.

It is important to be clear about what can and cannot be learnt from the simulations. First any simulation incorporates limited physics and limited spatial resolution. In the real world the fluid is a magnetised and almost perfectly conducting plasma. The shear flow at the cloud-corona interface will draw out and strengthen the field lines originally in the plasma. This drawing out will make the velocity distribution of particles anisotropic, which will excite plasma instabilities. These instabilities will both heat and mix the plasma. By contrast the tendency of the field lines to follow stream lines will strongly inhibit mixing. None of this complex physics is included in the present simulations.

Instead, in the simulations ablation and mixing are driven by the Kelvin-Helmholtz instability, which gives rise to ripples in the fluid interface. These ripples develop into vortices, which shed smaller vortices, which themselves shed vortices. In a numerical simulation numerical viscosity prematurely truncates this hierarchy of vortices on a scale of a few times the grid spacing Δ. On scales finer than Δ, the fluid is represented as perfectly mixed,

whereas it is in reality a roughly fractal foam of high- and low-density regions. The condition for the simulations to be a reliable guide to the large-scale structure of the flow is that the large-scale dynamics of this foam is equivalent to the dynamics of the locally homogeneous fluid that is actually represented. This is a reasonable proposition, but it should be expected that the values of the flow's macroscopic parameters, such as ambient pressure and cooling rate, at which a simulation of given resolution most closely approximates reality are likely to vary with resolution.

The simulations do not include thermal conduction. On the smallest scales conduction must play an important role in homogenising a mixture of cloud and coronal gas, and in the simulations this role is effectively covered by numerical mixing and diffusion. For what concerns conduction on intermediate and larger scales, it should be recalled that in a magnetised plasma heat is largely conducted along field lines. The field lines in upstream ambient gas are inevitably disconnected from field lines in the cloud. Any connection between these sets of field lines must occur in the turbulent wake, and this fact is likely to severely limit the effectiveness of thermal conduction.

In addition, the physical properties of the clouds and the corona considered here are such that the clouds would be stable against conductively-driven evaporation if they were stationary (see Nipoti & Binney 2007), so it is very unlikely that conduction plays an important role in the energetics of the problem. In principle conduction lowers the rate at which a moving cloud is ablated, by damping the Kelvin-Helmholtz instability (Vieser & Hensler 2007a,b), but this effect will be unimportant if conduction is magnetically suppressed to values small compared to the Spitzer or saturated values.

In light of these remarks, the simulations have two principal aims.

(i) To estimate the mass-loss rate α for comparison with $\alpha_{\rm crit}$. It is advantageous to do this in the absence of radiative cooling for then one can identify the cloud with gas at $T \lesssim 10^5\,{\rm K}$ since any ablated mate-

rial will be heated to and remain at higher temperatures. Simulations show that the mass-loss rate is reasonably independent of Δ.

(ii) To show that for any given metallicity of the gas, there is a critical ambient pressure $P_{\rm crit}$ above which the mass of cool gas increases with time through condensation in the wake and below which the wake tends to evaporate. Although the values of $P_{\rm crit}$ vary with both metallicity and Δ, they lie within the range of values that occur in practical cases. Hence, it is plausible that the true value of $P_{\rm crit}$ lies below the actual ambient pressures, so real wakes give rise to condensation and accretion.

4.3.1 The simulations

The parameters of the simulations are listed in Table 4.1. In all simulations the initial cloud velocity v_0 was $75\,{\rm km\,s^{-1}}$ and the initial radius $r_{\rm cl}$ was 100 pc. The temperature of the corona is restricted to a narrow range around $2 \times 10^6\,{\rm K}$ by the requirement that the corona be bound to the Galaxy and yet be extensive enough to contain a cosmologically significant mass (e.g. Fukugita & Peebles 2006), so in all simulations the corona's temperature $T_{\rm cor}$ was fixed to $2 \times 10^6\,{\rm K}$. In simulations of the low-pressure sequence the total particle density of the corona $n_{\rm cor}$ was $10^{-3}\,{\rm cm^{-3}}$ (except in the Z–0–L simulation in which it was reduced to $4 \times 10^{-4}\,{\rm cm^{-3}}$), implying $n_{\rm e} \simeq 0.5 \times 10^{-3}$, while in the high-pressure simulations it was twice as great. These values are both lower than the density $n_{\rm e} = 2.6 \times 10^{-3}\,{\rm cm^{-3}}$ at $r = 10\,{\rm kpc}$ in model 2 of Fukugita & Peebles (2006), and may be compared with the total particle density $n = 4 \times 10^{-4}$ at 10 kpc above the plane adopted by Heitsch & Putman (2009) or the mean electron density $\langle n_e \rangle \simeq 5 \times 10^{-4}\,{\rm cm^{-3}}$ within 50 kpc from the Milky-Way disc estimated by Anderson & Bregman (2010). In all but two simulations the initial cloud temperature $T_{\rm cl}$ was $10^4\,{\rm K}$; in the last two (high-pressure) simulations the cloud temperature was lowered to $5 \times 10^3\,{\rm K}$ since at the higher temperature (and therefore

Simulation	time (Myr)	[Fe/H]	$n_{\rm cor}$ ($\rm cm^{-3}$)	$T_{\rm cl}$ (K)	$M_{\rm cl}$ ($10^4\,\rm M_\odot$)	grid size
Low-pressure simulations						
Z–no–L	25	no met.	10^{-3}	10^4	1.1	c,m,f
Z–3–L	25	-3.0	10^{-3}	10^4	1.1	c,m,f
Z–2–L	25	-2.0	10^{-3}	10^4	1.1	c,m,f
Z–1.5–L	25	-1.5	10^{-3}	10^4	1.1	c,m,f
Z–1–L	25	-1.0	10^{-3}	10^4	1.1	c,m,f
Z–0.5–L	25	-0.5	10^{-3}	10^4	1.1	m,f
Z–0–L	25	0.0	4×10^{-4}	10^4	0.44	m
High-pressure simulations						
Z–1.5–H	25	-1.5	2×10^{-3}	10^4	2.2	m
Z–1–H	50	-1.0	2×10^{-3}	10^4	2.2	m
Z–1–H–LowT	50	-1.0	2×10^{-3}	5×10^3	4.4	m

Table 4.1: Parameters of the simulations. The grids sizes are coarse (c) 768×384, medium (m) 1024×512 or 1536×512 for simulations evolved up to 50 Myr, and fine (f) 1536×768. The corresponding spatial resolutions are $\sim3\times3$ pc, $\sim2\times2$ pc and $\sim1.5\times1.5$ pc, respectively. Each configuration is simulated both with and without radiative cooling.

lower density contrast) the cloud was totally disrupted after 50 Myr[2]. The cloud mass ranged from 0.44 to $4.4\times10^4\,\rm M_\odot$ depending on the pressure of the corona and the temperature of the cloud. The Jeans mass of the standard cloud ($r_{\rm cl}=100$ pc, $T_{\rm cl}=10^4$ K) is $1.6\times10^8\,\rm M_\odot$ so neglecting the cloud's self gravity is amply justified.

The calculations were performed using the ECHO++ code (Chapter 3), on two-dimensional, Cartesian grids of three sizes: coarse (c) 768×384, medium (m) 1024×512 or 1536×512 for simulations run to 50 Myr, and fine (f) 1536×768. The corresponding spatial resolutions are $\sim3\times3$ pc, $\sim2\times2$ pc and $\sim1.5\times1.5$ pc, respectively. Open boundary conditions are imposed to all the sides of the computational domain. Every configuration was simulated twice, once with cooling on and once with cooling off. When

[2]We recall that the Kelvin-Helmholtz characteristic timescale is given by $t_{\rm KH}=\chi^{1/2}t_{\rm flow}$, where $\chi=\rho_{\rm cl}/\rho_{\rm cor}$ and $t_{\rm flow}=r_{\rm cl}/v_0$ (e.g. Murray et al. 1993). For the standard clouds of this Chapter $t_{\rm KH}\sim20$ Myr.

radiative cooling is permitted, it follows the prescription of Sutherland & Dopita (1993) (see Section 3.5). In the simulations presented in this Chapter the metallicity of the cloud is always the same as that of the ambient medium, and is varied from zero up to solar. This is, of course, an approximation of what happens in the reality because fountain clouds, which are composed by gas coming from the star-forming disc may have a metallicity more than 10 times larger than that of the coronal gas. At the time that this investigation was carried out, the numerical code did not include support for multiple metallicities of the gas (see Section 3.6). However, the results obtained here are similar to those obtained in simulations with two different metallicities for the two phases presented in Chapter 5. Indeed, the use two different metallicity for the cloud and the corona favours condensation of the coronal gas into the turbulent cloud's wake (see Section 4.4.2).

Since one of the dimensions perpendicular to the cloud's velocity has been suppressed, we are simulating a flow around an infinite cylindrical cloud that is moving perpendicular to its long axis. The cylinder initially has a circular cross section of radius $r_{\rm cl}$ and thus, from the simulations, quantities per unit length of the cylinder are obtained. These latter are related to the corresponding quantities for an initially spherical cloud of radius $r_{\rm cl}$ by multiplying the cylindrical results by the length $\frac{4}{3}r_{\rm cl}$ within which the mass of the cylinder equals the mass of the spherical cloud.

4.3.2 Flows without radiative cooling

In this Section, flows in the absence of radiative cooling are studied, in order to assess the importance of the limited resolution of the simulations.

Figure 4.2 shows the temperature distribution on the grid after 25 Myr and 50 Myr for the simulation Z–1–H–LowT with radiative cooling turned off. The cloud has been flattened into a pancake by ram pressure from the medium it is moving into. The shear flow over the leading face of the pancake is causing vortices to be shed from the pancake's edges that are analogous to the vortices shed by an aeroplane wing. In the highly turbulent

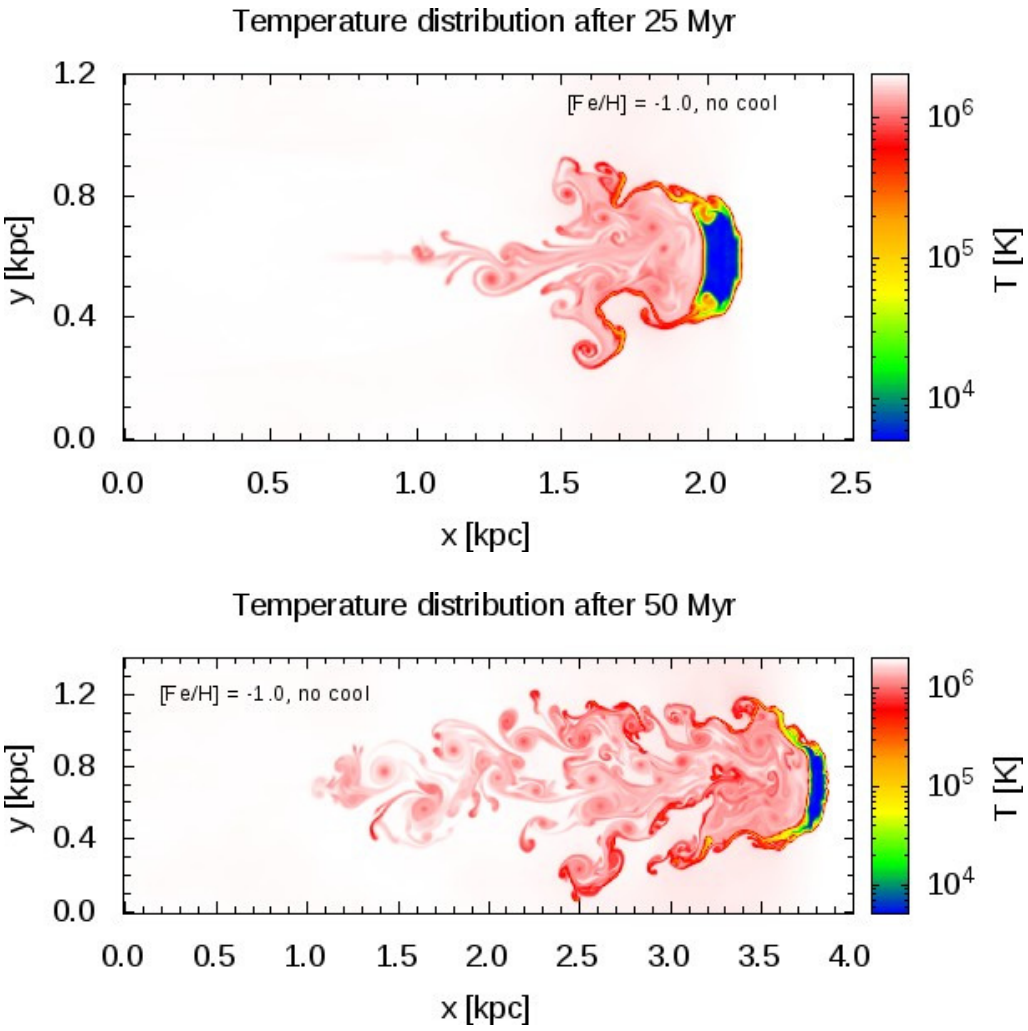

Figure 4.2: The temperature distribution after 25 and 50 Myr when radiative cooling is switched off for the simulation Z–1–H–LowT (see Table 4.1). The computational grid has medium resolution, the initial cloud temperature was 5×10^3 K and the coronal density was 2×10^{-3} cm^{-3}.

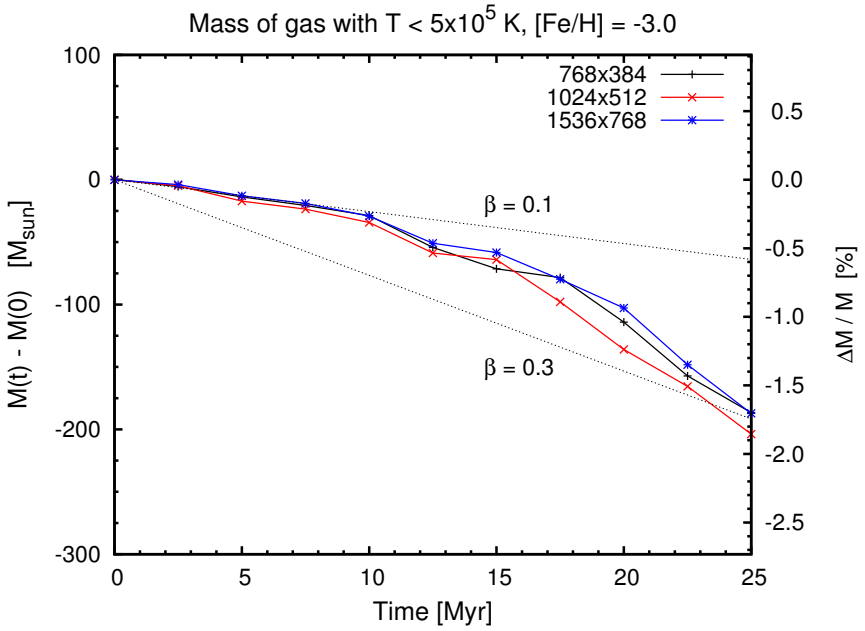

Figure 4.3: The evolution of the mass of gas at $T < 5 \times 10^5$ K for the simulation Z–3–L when the cooling is switched off. All the different resolutions at which the simulation is run are shown. The dotted straight lines show the critical mass-loss rate $\alpha_{\rm crit}$ for two values of β. The particle density of the corona is $10^{-3}\,{\rm cm}^{-3}$.

wake behind the cloud, the temperature fluctuates around 10^6 K depending on the fraction of the gas in each cell that comes from the cloud rather than the corona.

Figure 4.3 quantifies the speed at which ablation reduces the cloud's mass by plotting the mass of gas below 5×10^5 K versus time for the simulation Z–3–L at three different resolutions. Over the simulated 25 Myr $\sim 200\,{\rm M}_\odot$ of gas ($\sim$ 2 per cent of the cloud's mass) are heated to above 5×10^5 K, regardless of the grid resolution; it seems that even the coarsest grid has sufficient resolution to model satisfactorily the stripping of gas from the leading edge of the cloud. In the absence of radiative cooling, any gas that is stripped from the cloud will eventually be heated to above 5×10^5 K as it mixes with coronal gas. The details of the smallest vortices involved in the mixing process are resolution-dependent in the sense that at higher resolutions some gas remains cold for slightly longer

before numerical mixing on the grid scale eliminates it. The cloud's mass-loss rate is resolution-independent because all stripped gas will be heated within a couple of large-scale eddy-turnover times, regardless of resolution. The mass-loss rate increases gently with time because it depends on the area of the cloud's leading face, which increases with time as the cloud is squashed into a thinner and thinner pancake, a process that is apparent in Figure 4.2. The dotted straight lines in Figure 4.3 show the critical mass-loss rate defined by equation (4.4) for $\beta = 0.1$ and 0.3. As predicted above on dimensional grounds, the measured mass-loss rate lies near $\alpha_{\rm crit}$.

The cut in temperature chosen to discriminate between cold gas and coronal gas may appear quite high. In the simulations without cooling the stripping rate of the gas does not significantly depend on the adopted choice of the temperature cut. On the other hand, this choice can be important in the presence of cooling for the determination of the pressure and the metallicity of the corona at which condensation in the wake occurs. However, material at $T < 5 \times 10^5\,{\rm K}$ should cool quite rapidly to lower temperatures (see Figure 4.2) and thus we do not expect that the results derived from simulations that include radiative cooling are significantly affected by the adoption of a lower temperature cut.

4.3.3 Flows with radiative cooling

When radiative cooling is switched on, the strength of the dependence of the cooling rate upon T that is apparent in Figure 4.2, substantially increases the difficulty of predicting the outcome of the simulations and the uncertainties surrounding their results because now the structure of the turbulent wake is crucial. Indeed, evaporation is favoured over cooling by more effective dispersal of stripped material through a large volume of the corona. The higher the resolution delivered by the code, the greater the dynamic range of the hierarchy of vortices, and the more effective is the dispersal of stripped material, with the consequence that increased resolution favours evaporation over condensation.

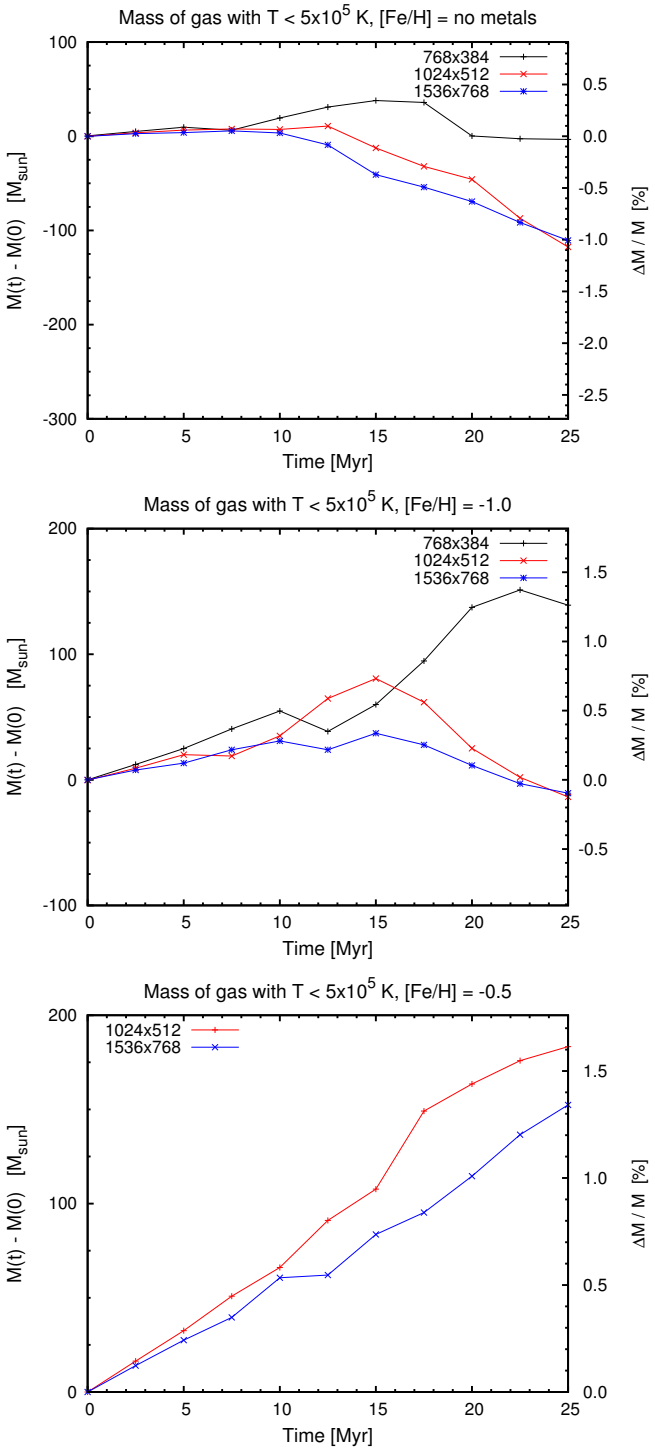

Figure 4.4: The same as Figure 4.3 but with radiative cooling turned on. In the top panel the plasma has primordial abundances, while in the middle and bottom panels [Fe/H] $= -1$ and -0.5, respectively. In all three panels the corona had particle density $10^{-3}\,\mathrm{cm}^{-3}$.

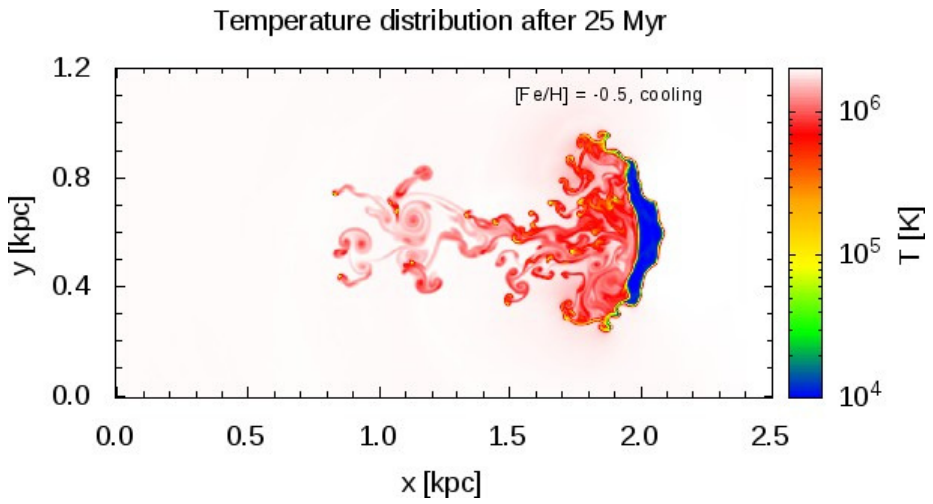

Figure 4.5: Temperature distribution after 25 Myr for the simulation Z–0.5–L with radiative cooling turned on. The metallicity is [Fe/H] = −0.5 and the coronal density $10^{-3}\,\mathrm{cm}^{-3}$.

Each panel of Figure 4.4 is the analogue of Figure 4.3 but with radiative cooling turned on; in the three panels the metallicity increases from zero (top panel) through [Fe/H] = −1 (middle panel) to −0.5 (bottom panel). The simulations with [Fe/H] < −1 do not differ significantly from that at zero metallicity. In all three panels the mass of cool gas (i.e. gas at $T < 5 \times 10^5\,\mathrm{K}$) starts by increasing rather than decreasing, and the rate at which this happens naturally increases with metallicity. When [Fe/H] = −0.5, the increase continues throughout the 25 Myr simulated, but at lower metallicities the mass of cool gas eventually starts to decrease. As anticipated, the results are unfortunately dependent on numerical resolution: in general there is a tendency for the mass of cold gas to decrease as the resolution increases, although the medium and high-resolution simulations give rather similar results.

Figure 4.5 shows the temperature distribution at $t = 25\,\mathrm{Myr}$ in a simulation with cooling of plasma with [Fe/H] = −0.5 and ambient particle density $10^{-3}\,\mathrm{cm}^{-3}$. Comparing this figure with the upper panel of Figure 4.2 it can be see that cooling makes the wake longer and less laterally

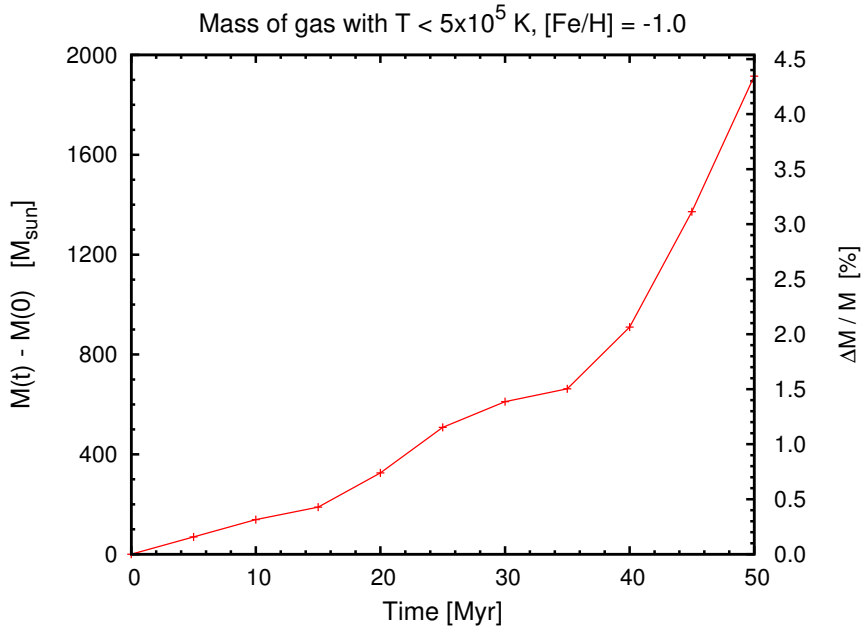

Figure 4.6: The evolution of the mass of gas at $T < 5 \times 10^5$ K in the Z–1–H–LowT simulation.

extended. Condensation of coronal gas occurs in the turbulent wake of the cloud and, as a consequence of this process, knots of cold material, that trail behind the cloud itself, form.

Figure 4.6 shows the effect of doubling the particle density of the corona to $2 \times 10^{-3}\,\mathrm{cm}^{-3}$: even at metallicity $[\mathrm{Fe/H}] = -1$ the mass of cool gas now increases throughout the 50 Myr simulated, and in fact in the latter half of the simulation cold gas accumulates at an accelerating rate. This result should be contrasted with that shown by the middle panel of Figure 4.4, which shows that at the same metallicity but half the density, the mass of cool gas starts to decrease after $\sim$ 15 Myr. If the behaviour shown in Figure 4.6 is extrapolated to the whole Milky Way halo, assuming as its total mass the value $\sim 4.5 \times 10^8\,\mathrm{M}_\odot$ (see Section 4.2.1), a global accretion rate of $\approx 0.5\,M_\odot\,\mathrm{yr}^{-1}$ is obtained. This accretion rate is half of that required to match the observed star formation rate in spirals. However, it is likely that the derived value of the accretion rate is underestimated by the simulation.

First of all the metallicity of the cooling gas is roughly a factor 3 less than that expected from the mixing of coronal gas with [Fe/H] = −1.0 and gas stripped from fountain clouds with [Fe/H] = 0 (see Section 4.4.2). Moreover, the estimate of the accretion rate assumes that condensation of the corona proceeds at a constant rate while, as mentioned above, Figure 4.6 clearly shows that the condensation rate increases with time. Given these uncertainties in the estimate, we can conclude that the global accretion rate is consistent with star formation requirements.

Figure 4.7 shows for the high-pressure simulation Z–1–H–LowT the distribution of cool gas along the cloud's direction of travel (top panel) and its distribution in velocity along the same direction (bottom panel) at the start of the simulation (black curve) and after 50 Myr when radiative cooling is (blue curve) or is not (red curve) included. From the upper panel the effectiveness of cooling in enhancing the mass of cool gas can be clearly seen. Less than 1 percent of the cold gas lies more that 1 kpc behind the cloud. In the lower panel around $75\,\mathrm{km\,s^{-1}}$ the deceleration of the main body of the cloud is clearly detected, but more striking is the width of the velocity range over which small amounts of cool gas are distributed. A few times $100\,\mathrm{M_\odot}$ is accelerated to higher velocities than the cloud's. A slightly larger mass of gas is decelerated to negative velocities. This velocity distribution implies that gas circulates around vortices at speeds that are comparable to the speed of the cloud's forward motion.

Figure 4.8 shows the distribution of cold gas in x, the direction of travel, and in v_x for the high-pressure simulation Z–1–H–LowT with and without cooling. Turning on cooling greatly broadens the extent in both x and v_x of low-density cool gas. In both simulations, the region of highest gas density runs from $70\,\mathrm{km\,s^{-1}}$ at the cloud's location down to $\sim 20\,\mathrm{km\,s^{-1}}$ 0.5 kpc behind the cloud. Thus hydrodynamics leads to a steep velocity gradient, $\sim 80\,\mathrm{km\,s^{-1}\,kpc^{-1}}$ in the part of the wake that will dominate 21-cm emission.

The lower panel of Figure 4.8 shows that the velocity width of the wake

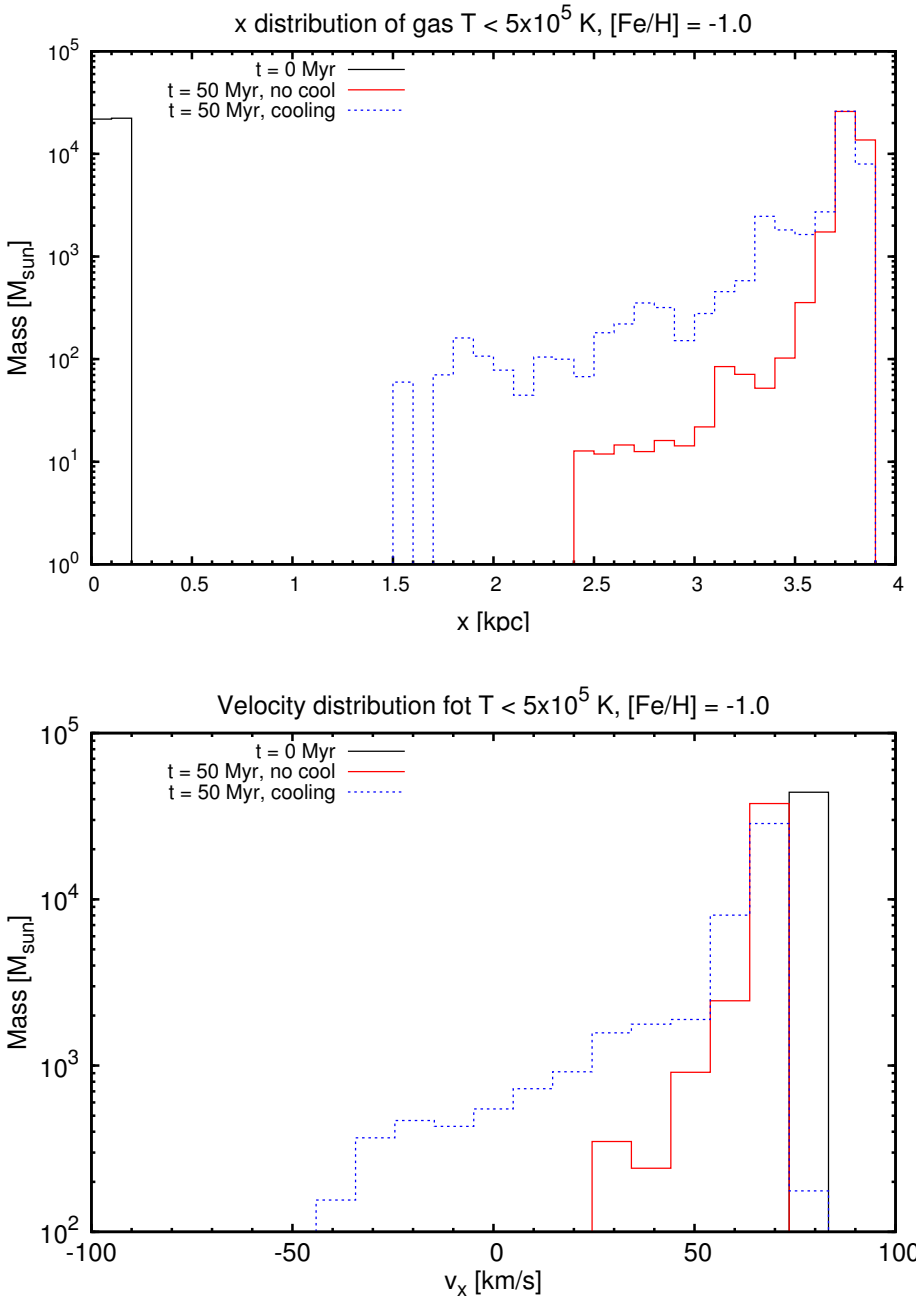

Figure 4.7: Upper panel: distribution of cool gas along the cloud's direction of travel for the simulation Z–1–H–LowT. The black curve shows the initial distribution while the blue dotted curve and red solid curve show the distributions at $t = 50\,\mathrm{Myr}$ with and without radiative cooling, respectively. Lower panel: distribution of cool gas as a function of the velocity along the direction of travel for the same simulation.

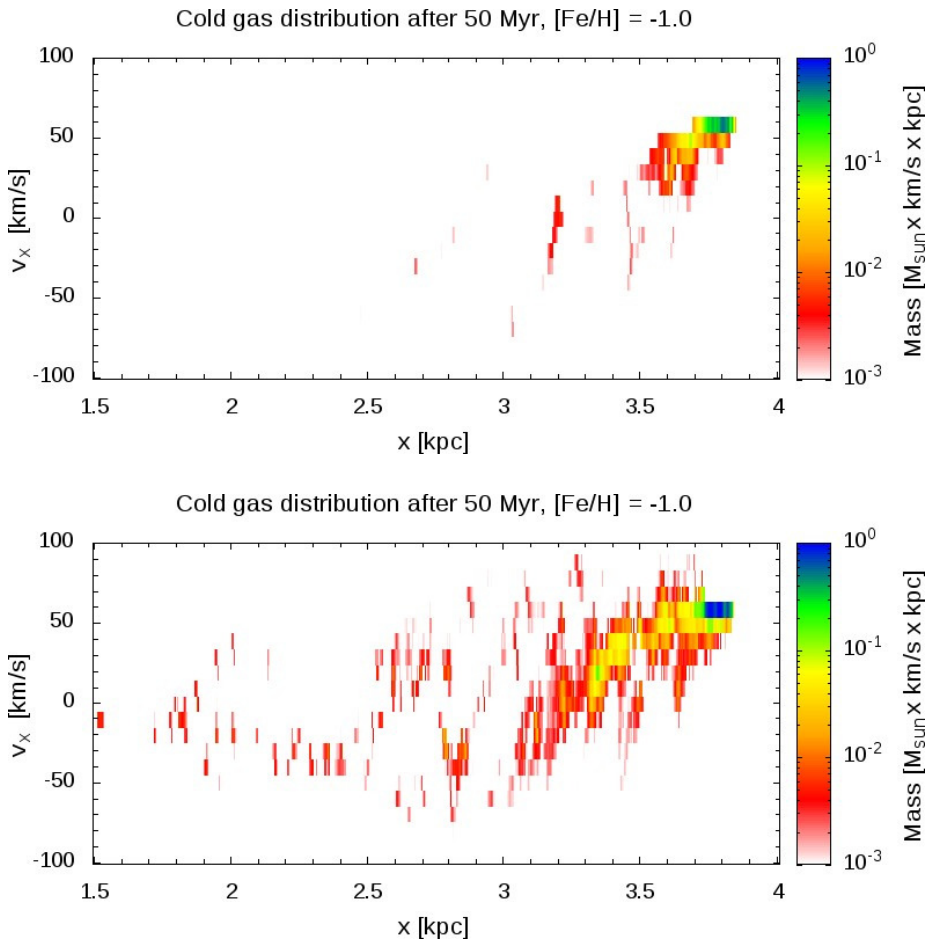

Figure 4.8: Distribution of velocities as a function of distance down the wake in Z–1–H–LowT at 50 Myr when cooling is switched off (upper panel) and on (lower panel)

.

increases with distance from the cloud for $\sim 800\,\mathrm{pc}$ from the cloud as a result of the lower envelope (velocities in the opposite direction to the cloud's motion) moving downward towards $-100\,\mathrm{km\,s^{-1}}$, while the upper boundary remains at $\sim 90\,\mathrm{km\,s^{-1}}$. This is further evidence that turbulent eddies impart peculiar velocities comparable to the cloud's velocity. Just behind the cloud material has to flow faster than the cloud in order to flow into the space vacated as the cloud moves on. Further back similar vortices carry cold gas away from the cloud with similar velocities. In the region from 1 to 2 kpc behind the cloud, the turbulence damps quite rapidly.

4.4 Discussion

Notwithstanding all the limitations incorporated in the simulations that we have presented in this Chapter, a number of interesting results can be derived from their analysis. The most important are listed below.

(i) There is clear evidence that the simulations' limited resolution is adequate for determining the rate at which gas is stripped from a cloud.

(ii) The stripping rate tends to increase with time as a result of the cloud being flattened by ram pressure.

(iii) The stripping rate is best determined from simulations in which cooling is turned off, and it is found to lie close to the rate expected on dimensional grounds. In Section 4.2 it was shown that this rate is very similar to the critical rate at which condensation of coronal gas takes over from evaporation of the H I cloud.

(iv) Whether stripped gas is evaporated or leads to the condensation of coronal gas depends on the structure of the turbulent wake. Consequently the finite spatial resolution of the simulations makes it impossible to determine with confidence the combinations of pressure and metallicity which divide evaporation from condensation. However simulations suggest, in agreement with analytic arguments, that

the typical pressures and metallicities of galactic coronae are in the range where condensation of the coronal gas in the wakes of fountain clouds occurs.

(v) The global accretion rate estimated from the simulations is consistent with the value required to sustain star formation in galaxies like the Milky-Way.

(vi) The neutral gas that trails the cloud is strongly influenced by hydrodynamics forces and cannot be considered to be on an orbit. There is a large velocity gradient along its high-density ridge in velocity-position space. Within $\sim 2\,\mathrm{kpc}$ from the cloud the velocity width of the stream is of order of the cloud's velocity.

4.4.1 Comparison with the observations

If the picture developed here is correct, the emission of each cloud is extended in velocity and is elongated on the sky due to the formation of the turbulent wake. Very sensitive 21-cm data would be required to see the full extent of the trail of an individual cloud. However, the integrated emission from many individually undetectable trails must contribute to the H I "beards" of nearby galaxies (Fraternali et al. 2002; Sancisi et al. 2008).

Clearly it is to surveys of our own Galaxy that one must turn for evidence that clouds have H I-rich wakes. Maps of the 21-cm emission of individual high-velocity clouds generally display a head-tail morphology: the cloud is elongated and the point of highest surface brightness lies towards one end (e.g. Brüns et al. 2001; Westmeier et al. 2005). In the scenario proposed here, head-tail morphologies can be explained by the interaction between the cloud and the ambient (coronal) medium. This interaction leads to the formation of trailing material behind the cloud.

Even in our Galaxy most emission from extra-planar gas is unresolved in the sense that along any direction in the Leiden-Argentina-Bonn (LAB) survey (Kalberla et al. 2005), emission is detected over a wide band in ve-

locity around zero. However, a scan through the data cube, one heliocentric velocity at a time, reveals numerous elongated structures along which there is a systematic trend in velocity. These could well be the wakes of relatively massive clouds.

Clouds with masses well below the threshold for detection of their 21-cm emission can be detected through the absorption lines to which they give rise in the ultraviolet spectra of background sources. Absorption-line studies suggest that large H I complexes are associated with numerous small H I clouds (Richter et al. 2005). Could these small clouds be the knots of cold gas visible in the wake of Figure 4.5? If this interpretation is correct, the small clouds would be found only on one side of the large complex, and they would have a mass spectrum that was restricted to masses very much smaller than that of the complex. Finally, recent observations of low ionised silicon absorption lines around high- and intermediate-velocity clouds indicate that a significant amount of gas is cooling in the halo of our Galaxy at a rate of $\sim 1\,\mathrm{M}_\odot\,\mathrm{yr}^{-1}$ (Shull et al. 2009). Condensation of the corona naturally produces gas at $T < 5 \times 10^5\,\mathrm{K}$. Therefore the detection of silicon ions, and also of other elements in a higher ionization state (e.g Sembach et al. 2003), potentially provides observational support to the scenario presented in this Chapter.

4.4.2 Effect of different metallicities

In the simulations the metallicity of the cloud is the same as that of the corona, whereas real-world clouds will be more metal-rich than the corona by a factor 10 or more. Whether gas condenses or evaporates depends on the cooling rate of gas that is roughly a 50–50 mixture of gas stripped from the cloud and coronal gas, so the most realistic simulations are those in which the universal metallicity is about half that of real clouds; that is the simulations with [Fe/H] ~ -0.5.

Figure 4.9 shows the evolution of the mass of gas below $5 \times 10^5\,\mathrm{K}$ for the simulation Z–0.5–L compared to that of the v75 simulation of Chapter 5.

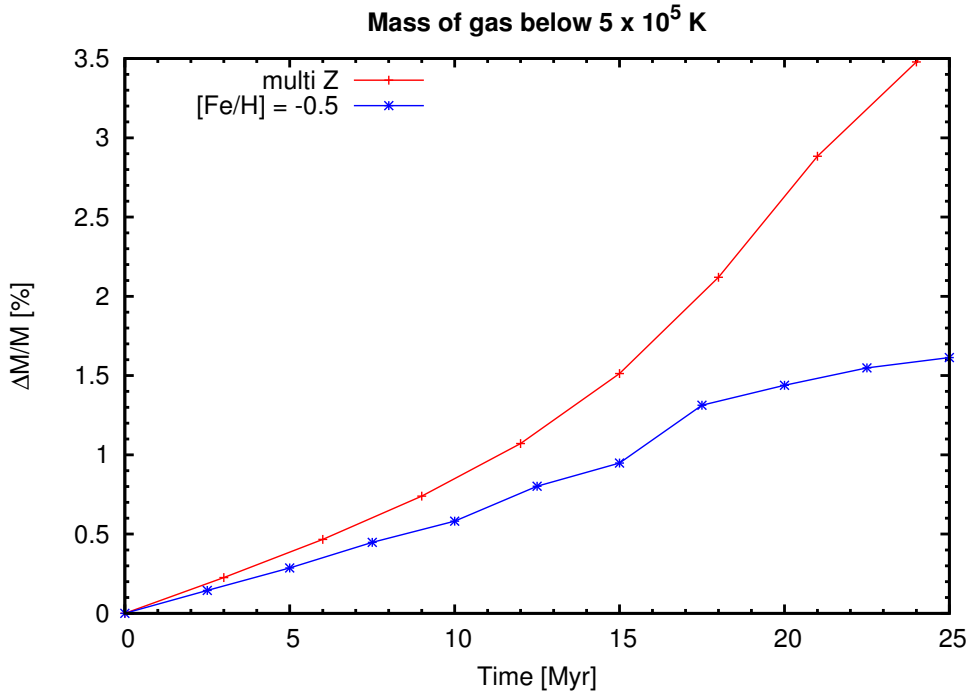

Figure 4.9: Evolution of the mass of gas below 5×10^5 K for the simulations Z–0.5–L (blue) compared to that of the v75 simulation of Chapter 5 (blue). The two simulations differ in the treatment of gas metallicity: in the former [Fe/H] $= -0.5$ everywhere, while in the latter [Fe/H] $= 0$ for the cloud and [Fe/H] $= -1$ for the corona.

The two simulations have the same coronal density and cloud initial speed but differ in the treatment of gas metallicity. In fact, in the former case the metallicity of the gas is *uniform* and fixed to [Fe/H] $= -0.5$, while in the latter the cloud has [Fe/H] $= 0$ and the corona [Fe/H] $= -1.0$. It is apparent that the mass of gas below 5×10^5 K increases, in both simulations, throughout the 25 Myr displayed in the figure. The discrepancy in the accumulation of the mass of the gas below the adopted temperature cut (a factor ~ 2 at 25 Myr) is due to the fact that a slightly more metal-rich wake forms ([Fe/H] $\gtrsim -0.4$, see also Figure 5.3) if the different metallicity of the two phases is considered. Therefore, the results of the present Chapter are confirmed, indeed strengthened, by including the more realistic treatment of gas metallicity used in Chapter 5.

4.4.3 Relation to cooling flows

Coronal gas in dark-matter haloes more massive than those of spiral galaxies has been extensively studied for decades (Sarazin 2009). Cooling within these haloes shows no tendency to produce a cold stellar disc – the coldest gas is near the centre, where the cooling time is shortest, and whatever gas cools out of the corona feeds the central black hole rather than forming a star-forming disc. The arguments presented so far may provide clues to understand why in less massive dark haloes cooling coronal gas flows into the disc rather than on to a central black hole: so long as the halo has a star-forming disc, that disc sustains its star formation by reaching up and grabbing coronal gas.

Discs are disrupted by major mergers, which may occur rather frequently. Analytic arguments and hydrodynamical simulations of cosmological clustering suggest that when the disc of a relatively low-mass galaxy is disrupted by a major merger, it will quickly re-form from filaments of cold inflowing gas (e.g. Governato et al. 2007). Thereafter it will sustain itself by grabbing coronal gas. When a more massive galaxy experiences a major merger, the disrupted star-forming disc is less likely to re-form. If it does not form from cold inflowing gas, it will not form from coronal gas, because in the absence of a star-forming disc, catastrophically cooling coronal gas will feed the central black hole and reheat the corona.

4.4.4 Relation to prior work

The ablation of clouds that move through a low-density medium has been discussed by, among others, Murray et al. (1993), Dinge (1997), Vieser & Hensler (2007a) and Heitsch & Putman (2009). In addition to studying the ablation of pressure-bounded clouds as here, some of these authors have considered also gravitationally bound clouds and included thermal conduction in addition to radiative cooling. Vieser & Hensler (2007a) found that thermal conduction stabilises a moving cloud by reducing the magnitude

of the velocity gradient in the boundary layer where the cloud meets the ambient medium; a smaller velocity gradient leads to slower growth of the Kelvin-Helmholtz instability.

Most previous simulations assume the flow to be axisymmetric around the velocity of the cloud's motion. In such simulations material becomes trapped on the assumed symmetry axis, where the radial velocity must vanish by symmetry. Murray et al. (1993) also simulated clouds with the symmetry assumed here and found that the main results were independent of the adopted geometry.

Murray et al. (1993) found ablation to proceed faster than in the cases studied here and interpreted their ablation timescale as the inverse of the Kelvin-Helmholtz growth rate, which is larger than $\alpha_{\rm crit}$ by $\sim (T_{\rm cor}/T_{\rm cl})^{1/2}$. This difference in the ablation rates arises from the use of a different criterion for identifying cloud gas: Murray et al. (1993) took this to be the mass within an appropriate sphere, whereas in the present approach cloud gas is defined as to be cool gas, regardless of where it resides. In other respects the results of this Chapter are in accordance with earlier findings.

The simulations most comparable to those discussed here are those of Heitsch & Putman (2009), who simulated the ablation of cool clouds that fall towards the disc through the corona. Consequently, their characteristic coronal density, $n_{\rm cor} \simeq 10^{-4}\,{\rm cm}^{-3}$, was a factor 2 to 4 lower than that considered here. Heitsch & Putman (2009) simulations used a three-dimensional grid, so their grid spacing was coarser and they could not provide evidence of numerical convergence. Their clouds, which had initial masses similar to those presented here, fragmented in a similar fashion. In most simulations the total mass of H I in the computational volume declined with time, although in some simulations an upturn in the H I mass is evident at late times as the cloud approaches the plane. The numerical results of this Chapter are entirely consistent with Heitsch & Putman (2009) findings, although the physical motivation is different and, crucially, the coronal density regime investigated here extends to the higher values which are expected near the

plane.

Recent attempts to model extra-planar H I include those of Barnabè et al. (2006) and Fraternali & Binney (2008). Barnabè et al. (2006) investigated the equilibria of differentially rotating distributions of gas in flattened gravitational potentials. They showed that by making the specific entropy and angular momentum of the gas vary appropriately within the meridional plane, the kinematics of the gas can be made consistent with the data for H I around NGC 891. They noted that dynamical equilibrium required the gas to be too hot to be neutral, so the gas within their model could not be the observed as H I itself, but suggested it might be coronal gas within which H I clouds were embedded as almost stationary structures. In Chapter 2 of this Thesis we saw that, in principle, it is possible to solve the problem of the high temperature in the models of Barnabè et al. (2006) by resorting to a stationary Jeans description of the system. However, we found that Jeans models are not able to reproduce the observed kinematics of the extra-planar H I gas in detail.

Fraternali & Binney (2008) fitted 21-cm data cubes for NGC 891 and NGC 2403 with fountain models that include accretion from an ambient medium. However, the picture of the connection between the galactic fountain and accretion on to the star-forming disc developed above differs materially from that proposed by Fraternali & Binney (2008): in that approach H I clouds grew in mass as they moved through the corona; here each cloud loses mass, but the mass of cold gas in a cloud and its wake taken together increases with time. Thus a natural question is whether the present picture predicts a similar overall picture of 21-cm emission to that proposed by Fraternali & Binney (2008). Individual clouds are for the most part not resolved in the data of NGC 891 and NGC 2403, so the observed emission is due to many superposed clouds. In the Fraternali & Binney (2008) model, each cloud places a blob of emission in the model cube, centred on its sky-position and line-of-sight velocity, and smeared by the angular and velocity resolution of the survey. We suspect that, if the model cubes of NGC 891

and NGC 2403 are modified to include the extended emission coming from the wakes of the clouds, their observable properties will be similar to Fraternali & Binney (2008) cubes because the sky-position and the velocity centroid of each cloud's total emission will be unchanged.

4.5 Summary

There is abundant evidence that in galaxies like ours, star-formation powers a fountain that each gigayear carries $\gtrsim 5 \times 10^9\,\mathrm{M}_\odot$ of H I to heights in excess of 1 kpc above the plane. Several lines of argument strongly suggest that galaxies like ours are surrounded by gas at the virial temperature – coronae. The density of the corona, which must vary with position, is very uncertain, especially in the region above the star-forming disc. However, there are indications that this density is such that the local coronal cooling time is of order a gigayear. At least half of the baryons in the Universe are believed to reside in coronae and their extensions to intergalactic space.

Models of the chemistry and stellar content of the Galactic disc require the disc to accrete $\sim 1\,\mathrm{M}_\odot\,\mathrm{yr}^{-1}$ of low-metallicity gas. The corona is the only reservoir of baryons that is capable of sustaining an infall rate of this order for a Hubble time. Therefore there is a strong prima-facie case that star formation in the disc is sustained by cooling of coronal gas.

The dynamical interaction of H I clouds of the fountain with coronal gas is inevitable. For any plausible coronal density, the ram pressure arising from motion through the corona leads to non-negligible loss of momentum by fountain clouds. If this momentum were retained by the corona rather than returned to the disc, the corona would rapidly become rotation-dominated. This possibility was not pursued here because, as it will be shown in the next Chapter, radiative cooling of the gas strongly influences the momentum transfer from the clouds to the corona, the net effect being a substantial reduction of the momentum acquired by the coronal gas. In particular, most of the coronal gas that absorbs momentum from fountain

clouds cools effectively into the clouds' wakes, returning the associated momentum to the cold gas. In addition, it is likely that this cooled coronal gas is shortly thereafter accreted by the disc to become the fuel with which disc galaxies sustain star formation. The absorption process proceeds as follows: (i) coronal gas strips gas from the leading edge of the cloud as a result of Kelvin-Helmholtz instability; (ii) in the turbulent wake of the cloud, the stripped gas mixes with a comparable mass of coronal gas; (iii) as a result of this mixing the cooling time becomes shorter than the cloud's flight time and coronal and stripped gas together form knots of H I that trail behind the cloud and fall on to the disc within a dynamical time. This scenario is suggested by a combination of analytic and observational arguments, and supported by hydrodynamical simulations.

Analytic arguments imply that for a given coronal pressure and metallicity there is a critical rate of mass loss by a cloud, $\alpha_{\rm crit}$, such that at lower mass-loss rates, stripped gas will be evaporated by the corona, and the total mass of H I will decrease during a cloud's flight. By contrast, when the mass-loss rate exceeds $\alpha_{\rm crit}$, stripped gas will lead to condensation of coronal gas, so the mass of H I increases over time. Dimensional arguments suggest that the actual mass-loss rate must lie close to $\alpha_{\rm crit}$.

Grid-based hydrodynamical simulations of the flight of a cloud were used to check the analytic arguments. Any hydrodynamical simulation is severely limited by its finite spatial resolution. However, there is evidence, from computations in which radiative cooling has been switched off, that simulations presented in this Chapter have sufficient resolution to provide reliable estimates of the mass-loss rate.

Simulations that include radiative cooling confirm the existence of a critical mass-loss rate $\alpha_{\rm crit}$ that depends on coronal pressure and metallicity in the expected manner. On account of the restricted resolution of the presented simulations, a definitive value for $\alpha_{\rm crit}$ within the local corona cannot be given. However, it can be argued that if the critical mass-loss rate lay above the actual mass-loss rates, the coronal density and metallicity would

rise secularly at the expense of the star-forming disc. As a consequence, the $\alpha_{\rm crit}$ would decrease until it fell below the actual mass-loss rate. That is, the conditions at the base of the corona have a tendency to adjust until they lead to accretion by the disc. The global accretion rate of the coronal gas estimated from the simulations is of the same order of that required to sustain star formation in discs.

The simulations make detailed predictions for what should be seen in studies of the high-latitude H I distribution in the Galaxy. Trails behind clouds should show large gradients in mean velocity that are dominated by hydrodynamical rather than gravitational forces. High-sensitivity data should reveal small quantities of gas distributed around the mean velocity by of order the cloud's velocity. The trail should be studded by knots of cold gas. The condensing coronal material can be also detected in absorption in the UV spectra of background sources. Indeed, a recently detected population of low ionised silicon absorbers shows that $\sim 1\,{\rm M}_\odot\,{\rm yr}^{-1}$ of gas is cooling in the halo of the Milky-Way.

5

Momentum transfer between fountain clouds and the hot corona

5.1 Introduction

In this Chapter we discuss the process of momentum transfer between the cold galactic fountain clouds and the hot cosmological corona, arising from their mutual interaction in the halo region of disc galaxies. We investigate this process, which has important consequences for the dynamical state of the two phases, by resorting to hydrodynamical simulations of cold clouds travelling through a hot medium at different relative velocities.

The simulations are similar to those presented in Chapter 4 but at least three significant improvements were added: (i) the metallicity of the gas is treated as a dynamical variable to take into account the fact that fountain clouds are more metal-rich than the corona by an order of magnitude or more (see next Section); (ii) the evolution of the system is followed for 60 Myr, to be compared with the 25 Myr of most of the simulations presented in the previous Chapter; and (iii) a wider range for the cloud-corona

relative velocity (between 50 and 200 $\mathrm{km\,s^{-1}}$) was studied. For what concerns the latter point, it should be pointed out that throughout this Chapter the cloud-corona relative velocity must be interpreted as difference in the *rotational* velocity between the two phases. Since from the current available data it is not possible to extract reliable kinematic information for the coronal gas, we do not known whether the corona rotates significantly. It follows that the cloud-corona relative velocity is not determined and all the range mentioned above, corresponding to the case of a corona that nearly corotates with the disc and that of a nearly static corona must be considered in the present investigation. In the current version of the code not only the metallicity evolves, but also the fluid's molecular weight μ is a function of temperature. Their variation is accounted for in the implementation of radiative cooling (see Sections 3.5 and 3.6), which is modelled according to the prescription of Sutherland & Dopita (1993).

Our major finding is that there is a velocity threshold between cloud and corona below which the corona does not absorb momentum from the cloud (see Section 5.3). We argue that the corona must be spinning fast enough for most clouds to move through it at a speed smaller than this velocity threshold. This prediction, and in particular its effects on the morphology of galactic coronae (see Section 5.4.1), will be tested by future soft X-ray observations. We also discuss, in Section 5.4.2, the implications of the existence of this velocity threshold for the kinematics of the cold extra-planar gas.

This Chapter is based on the results of the forthcoming paper Marinacci et al. (2011).

5.2 Set up of the hydrodynamical simulations

The initial conditions of the simulations are similar to those of Chapter 4 and consist in a cloud at $T_{\rm cl} = 10^4\,\mathrm{K}$ and radius $r_{\rm cl} = 100\,\mathrm{pc}$ that moves

Simulation	v_0 ($\mathrm{km\,s^{-1}}$)	$n_{\rm cor}$ ($\mathrm{cm^{-3}}$)	$M_{\rm cl}$ ($10^4\,\mathrm{M_\odot}$)
Standard simulations			
v200	200	10^{-3}	2.4
v150	150	10^{-3}	2.4
v100	100	10^{-3}	2.4
v75	75	10^{-3}	2.4
High-density simulations			
v100–H	100	2×10^{-3}	4.8
v75–H	75	2×10^{-3}	4.8
Low-density simulations			
v100–L	100	5×10^{-4}	1.2
v75–L	75	5×10^{-4}	1.2
v50–L	50	5×10^{-4}	1.2

Table 5.1: Parameters of the simulations. The initial temperature and metallicity of the corona are $T_{\rm cor} = 2 \times 10^6\,\mathrm{K}$ and $[\mathrm{Fe/H}] = -1$, respectively, while for the cloud $T_{\rm cl} = 10^4\,\mathrm{K}$ and $[\mathrm{Fe/H}] = 0$. All models are evolved up to 60 Myr. The grid size is 6114x1024 with spatial resolution $\sim 2 \times 2$ pc for all the simulations. In the case of v100 an additional run, with the same spatial resolution and grid size 6144x2048, was performed.

at a speed v_0 through a stationary and homogeneous background at $T_{\rm cor} = 2 \times 10^6\,\mathrm{K}$, which represents the corona. While in the previous Chapter the *relative* speed between the cloud and the corona was fixed at $v_0 = 75\,\mathrm{km\,s^{-1}}$, here different relative speeds in the range $50 \leq v_0 \leq 200\,\mathrm{km\,s^{-1}}$ are explored. If these relative speeds are interpreted as differences in rotational velocities, then two extreme possibilities are encompassed by the simulations: (i) the case of a non-rotating corona ($v_0 = 200\,\mathrm{km\,s^{-1}}$) and (ii) a corona which is rotating with a speed close to that of the disc ($v_0 = 50\,\mathrm{km\,s^{-1}}$). As on ballistic trajectories the galactocentric radii of the clouds would vary by less than 30%, and the clouds would reach heights above the galactic plane of a few kiloparsecs (see Fraternali & Binney 2006), the expected density variations of the coronal gas are not strong. Thus, as in Chapter 4, a homogeneous corona is assumed and the effect of the gravitational field

of the galaxy has not been considered. Moreover, the self gravity of the gas is also neglected because the cloud masses are much smaller than their Jeans mass. At the beginning of each simulation the cloud is in pressure equilibrium with its surroundings and the evolution of the system is followed for 60 Myr (significantly longer than the 25 Myr spanned by most runs in Chapter 4). In the standard simulations (see Table 5.1) the density of the background is $n_{\rm cor} = 10^{-3}$ cm^{-3}. For each value of v_0, two simulations were run: one (dissipative) in which the gas is allowed to cool radiatively, another (adiabatic) without radiative cooling. The more realistic cases are those in which the gas is allowed to cool, but the adiabatic runs enable us to distinguish the effect of cooling (strongly dependent on the density, temperature and metallicity of the gas) from non-dissipative effects like mixing and hydrodynamical instabilities. Two additional sets of dissipative simulations have been run with half (low-density simulations in Table 5.1) or twice (high-density simulations in Table 5.1) the coronal density to assess the influence of this latter on the results. In all initial conditions the cloud's metallicity takes the solar value (i.e. [Fe/H] = 0) and the coronal metallicity is [Fe/H] = −1 (see, e.g. Sembach et al. 2003; Shull et al. 2009). The metallicity of the fluid is allowed to vary from the initial conditions: in this respect the present simulations differ from those of Chapter 4, in which the metallicity was constant. This upgrade is important since the metallicity of a cloud ejected from the disc and that of the corona can differ by one order of magnitude or more, and the cooling rate of the gas critically depends on its metal content.

The simulations are performed with the code ECHO++ presented in Chapter 3. The calculations are performed on a two-dimensional Cartesian grid with open boundary conditions imposed to all the sides of the computational domain. Therefore, one of the dimensions perpendicular to the cloud's velocity has been suppressed, and in effect a flow around an infinite cylindrical cloud is simulated. As in the previous Chapter quantities per unit length of the cylinder are obtained and related to the corresponding

quantities for an initially spherical cloud of radius $r_{\rm cl}$ by multiplying the cylindrical results by $\frac{4}{3}r_{\rm cl}$. This correction is included in the values of the cloud mass $M_{\rm cl}$ quoted in Table 5.1. It should be noted that, due to pressure equilibrium in the initial conditions, for the same gas number density, temperature and cloud size $M_{\rm cl}$ is higher here than in the previous Chapter, because here the fact that μ depends on temperature is accounted for, while in Chapter 4 μ is fixed at the coronal value.

5.3 Results of the simulations

The results of the hydrodynamical simulations, with emphasis on the momentum transfer between the cloud and the ambient gas, are now described. While the two phases are unambiguously separated in the initial conditions (the cloud gas is at $T_{\rm cl} = 10^4\,{\rm K}$ and the coronal gas is at $T_{\rm cor} = 2 \times 10^6\,{\rm K}$), at later times, as a consequence of turbulent mixing and radiative cooling, a significant amount of gas is expected to be at intermediate temperatures . Therefore, at all times in the simulations, gas is defined as "hot" if $T > 10^6\,{\rm K}$ and as "cold" if gas at $T < 3 \times 10^4\,{\rm K}$. The hot phase was identified with the corona while the cold phase comprises gas originally belonging to the cloud plus gas which is condensing out of the corona. In any case, it was verified that the results derived from the simulations do not significantly depend on the specific choice of these temperature cuts.

5.3.1 Interaction between the cloud and the ambient medium

Qualitatively, the evolution of the cloud in the present simulations is similar to that observed in the simulations of Chapter 4. Due to the ram pressure arising from the motion, the cloud feels a drag which causes it to decelerate while the background gains momentum. The body of the cloud is squashed, and behind it a wide turbulent wake forms, in which the coronal and cloud gas mix efficiently and radiative cooling is particularly effective, with the

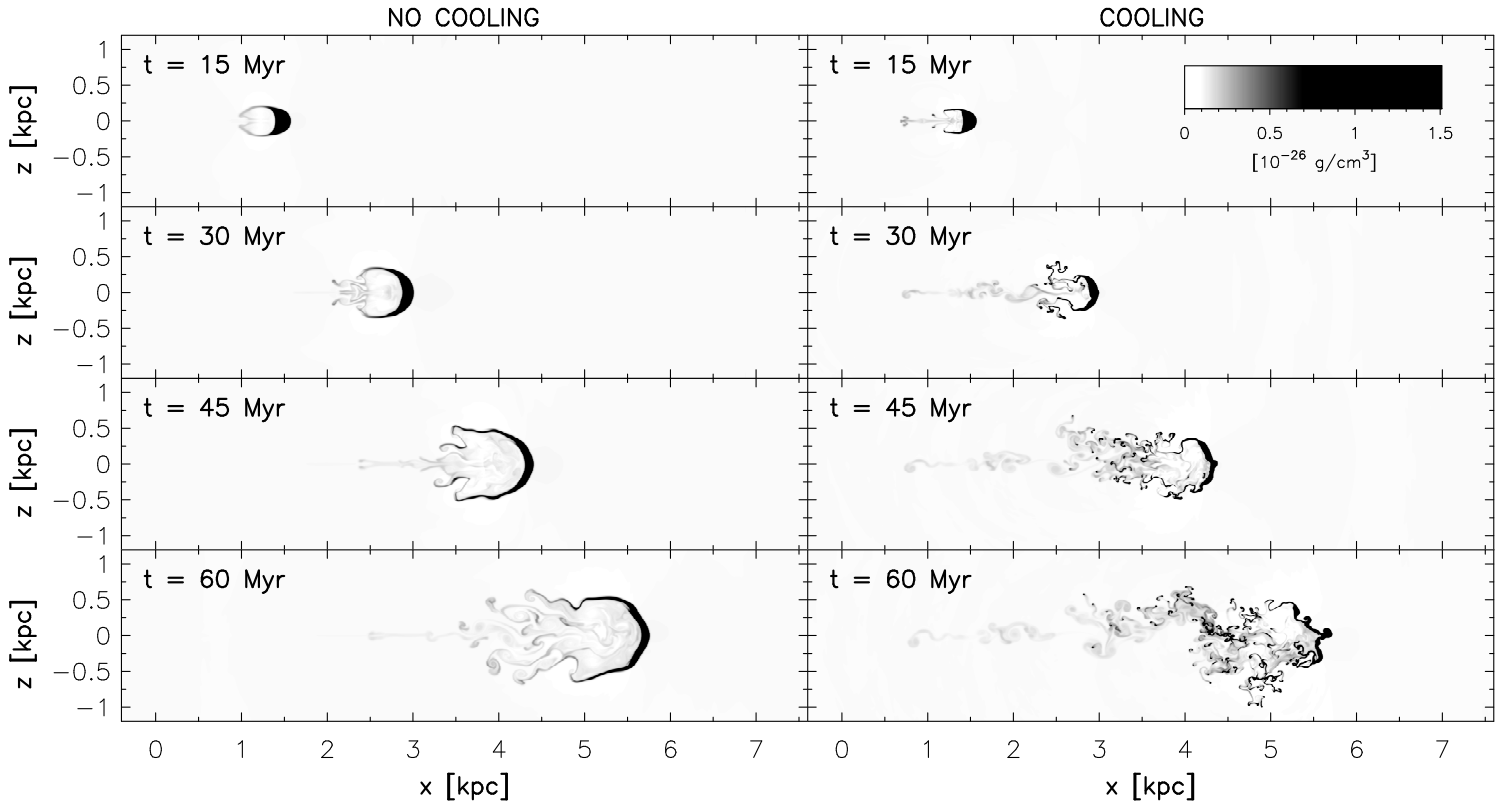

Figure 5.1: Density snapshots of the adiabatic (left panels) and dissipative (right panels) standard simulations with $v_0 = 100\,\mathrm{km\,s^{-1}}$ (v100 in Table 5.1). The time at which the snapshot has been taken is indicated in each panel. The initial position of the cloud centre is $x = 0$.

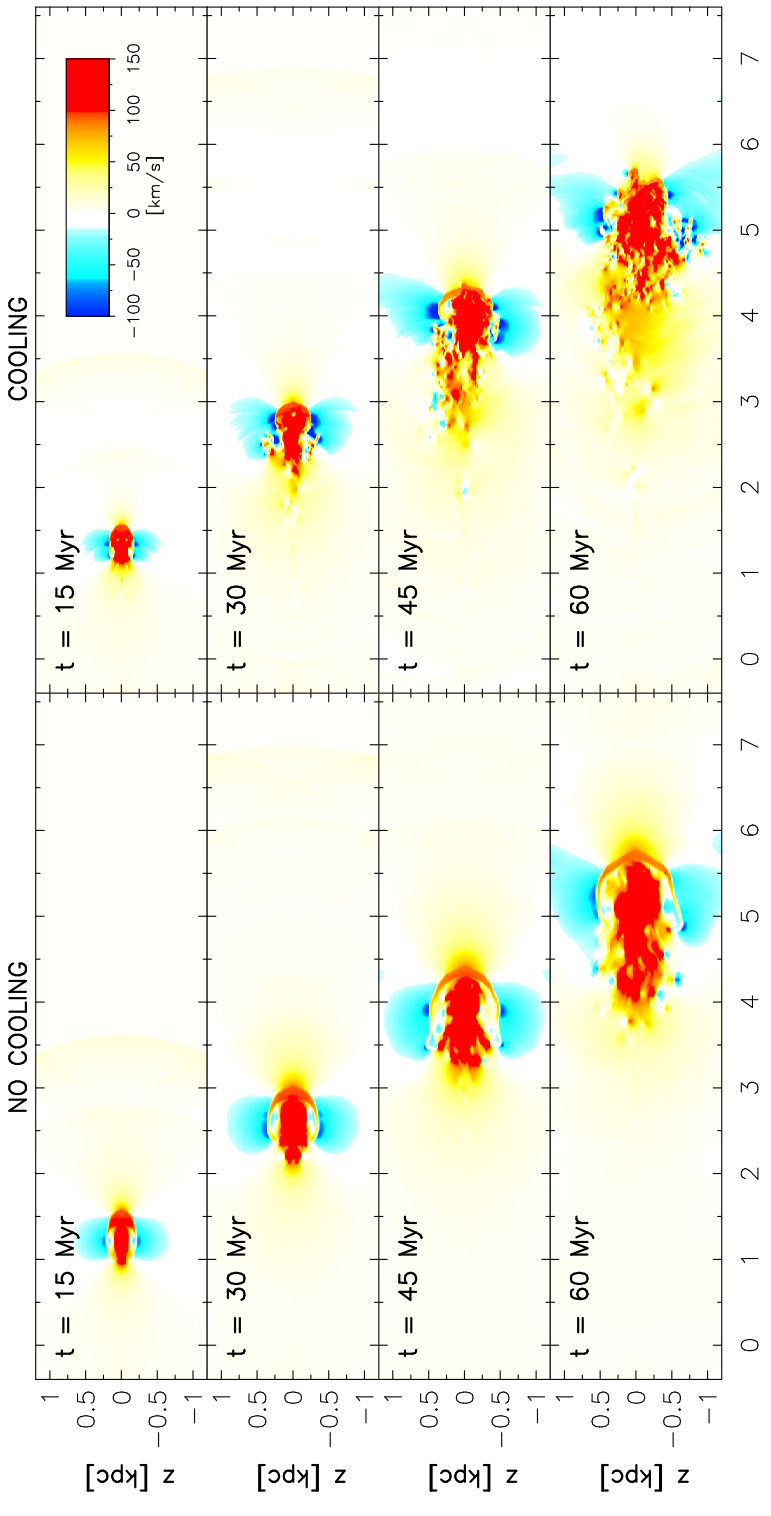

Figure 5.2: Snapshots of the velocity along the cloud's direction of motion (v_x) of the adiabatic (left panels) and dissipative (right panels) standard simulations with $v_0 = 100\,\mathrm{km\,s^{-1}}$. The time at which the snapshot has been taken is indicated in each panel. The initial position of the cloud centre is $x = 0$.

consequence that the mass of cold gas tend to increase with time. The wake has a complex velocity structure, with some fluid elements moving faster and other slower than the body of the cloud.

This behaviour is apparent from Figures 5.1 and 5.2, showing, respectively, density and velocity snapshots, at four different times, of the dissipative standard simulation with $v_0 = 100\,\mathrm{km\,s^{-1}}$ (right panels) and, for comparison, of the corresponding adiabatic simulation (left panels). The diagrams in the bottom panels clearly show that the cloud is decelerated by drag: at $100\,\mathrm{km\,s^{-1}} \simeq 0.1\ \mathrm{kpc\,Myr^{-1}}$ the cloud would travel, with no drag, a distance of about 6 kpc in 60 Myr, but neither in the presence nor in the absence of radiative cooling does the main body of the cloud reach that distance. The structure of the body of the cloud and of the wake is strongly influenced by the presence of radiative cooling: the wake appears more elongated and less laterally extended (except perhaps in the 60 Myr panel) when the radiative cooling of the gas is permitted. The extent of the velocity structure of the wake is greater, both laterally and in elongation, in the dissipative than in the adiabatic case at late times (see Figure 5.2). Just behind the cloud there is a region in which the velocities reach their maximum values and this region is more compact (less elongated) when cooling occurs. In front of the cloud the coronal gas is pushed by the cloud and therefore also in this region the gas has positive velocities. However, in contrast to what happens behind the main body of the cloud, this region is more extended in the absence of cooling.

Figure 5.3 shows temperature (left panels) and metallicity (right panels) snapshots of the dissipative standard simulation with $v_0 = 100\,\mathrm{km\,s^{-1}}$. The times at which these snapshots are taken are the same of Figures 5.1 and 5.2 described above. It is evident from the temperature panels that cooling is very effective in the turbulent wake of the cloud, where mixing between cloud and coronal gas occurs. In particular, at late times, several regions at low temperature, (indicated in blue in the color scale of the figure) in which coronal gas is actually condensing, appear in the wake. The low

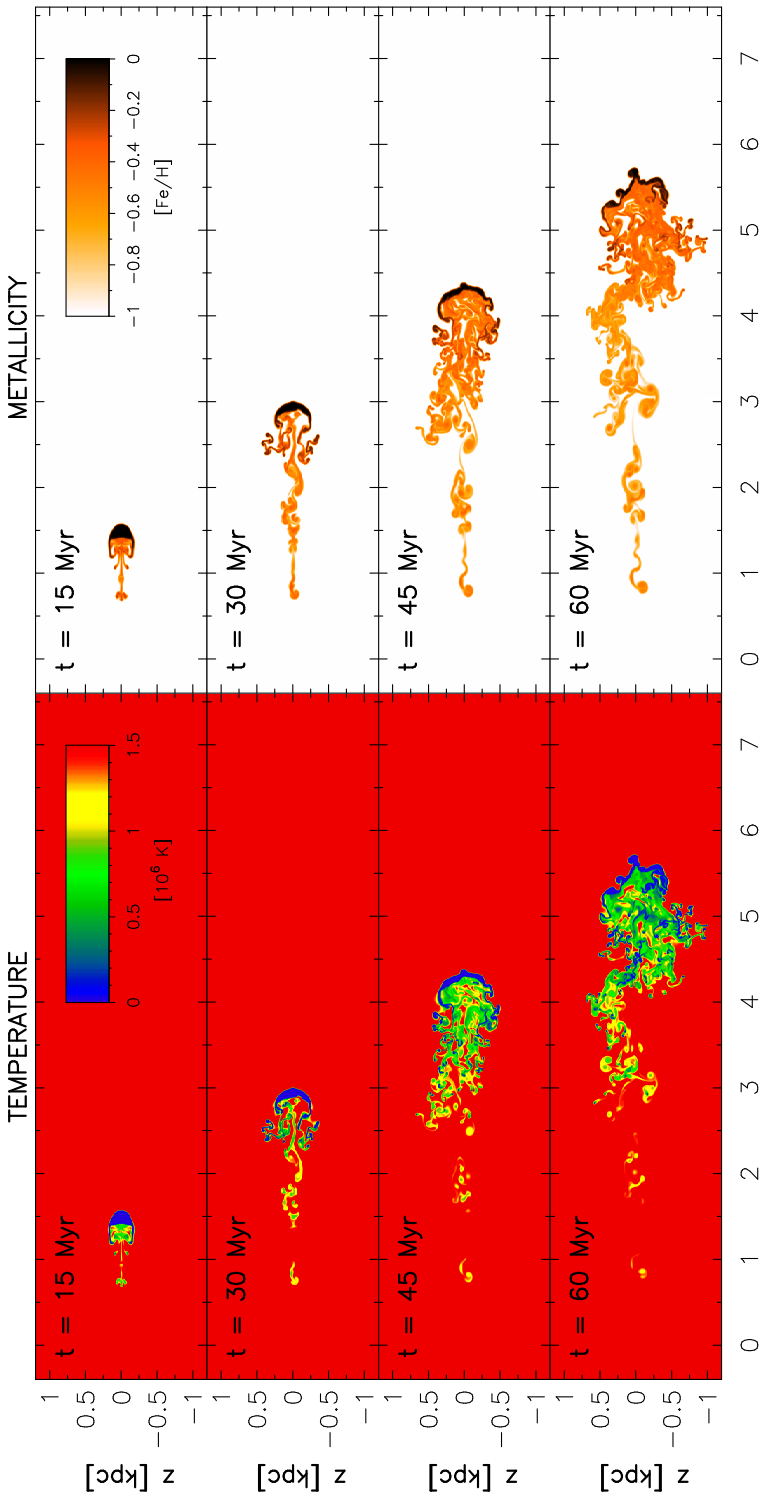

Figure 5.3: Temperature (left panels) and metallicity (right panels) snapshots of the dissipative standard simulation v100 (see Table 5.1). The time at which the snapshot has been taken is indicated in each panel. The initial position of the cloud centre is $x = 0$.

temperature regions appear to be confined to $\lesssim 1.5\,\mathrm{kpc}$ from the far front of the cloud, and this could imply that the coronal gas that is condensing in the wake can follow the cloud back to the disc, providing fresh material to sustain star formation. As we shall see below (but see also Section 5.3.3), this is a very likely scenario because most of the momentum lost by the cloud is absorbed by this condensing material.

The fact that efficient mixing is present in the cloud's wake can be seen in the metallicity panels: gas at intermediate metallicity, of which the wake is composed, must result from the mixing of high-metallicity cloud material with the low-metallicity corona. Regions of low temperature (i.e. where the cooling is particularly intense) are mostly found in correspondence of regions of high ($[\mathrm{Fe/H}] \gtrsim -0.4$) gas metallicity.

Comparing the final configuration with the initial conditions, it is found that the cold phase has increased its mass and that the corona has gained momentum. Quantitatively, the amount of mass and momentum transfer depends critically on radiative cooling. This can be seen in Figure 5.4, which shows the distributions of mass (upper panel) and momentum (lower panel) as functions of temperature after 50 Myr for the standard simulation with $v_0 = 100\,\mathrm{km\,s^{-1}}$ and, for comparison, for its adiabatic counterpart. In both panels the histograms peak around the temperatures of the coronal gas and the initial cloud temperature ($T_{\mathrm{cor}} = 2 \times 10^6\,\mathrm{K}$ and $T_{\mathrm{cl}} = 10^4\,\mathrm{K}$, respectively), and the distribution around these peaks is rather narrow. From the bottom panel of Figure 5.4 it is clear that there is an exchange of momentum between the cloud and the corona, but the corona acquires *less* momentum when the gas is allowed to cool, as can be inferred from the heights of the peaks at $T > 10^6\,\mathrm{K}$. This can be better understood if the mass distribution of the gas among the various phases is recalled. At the beginning, most of the gas is at the cloud and the corona initial temperatures, and only a small fraction of the total mass is at intermediate temperatures. The momentum of the cloud is mostly transferred to this intermediate temperature component as a result of the mixing. Because

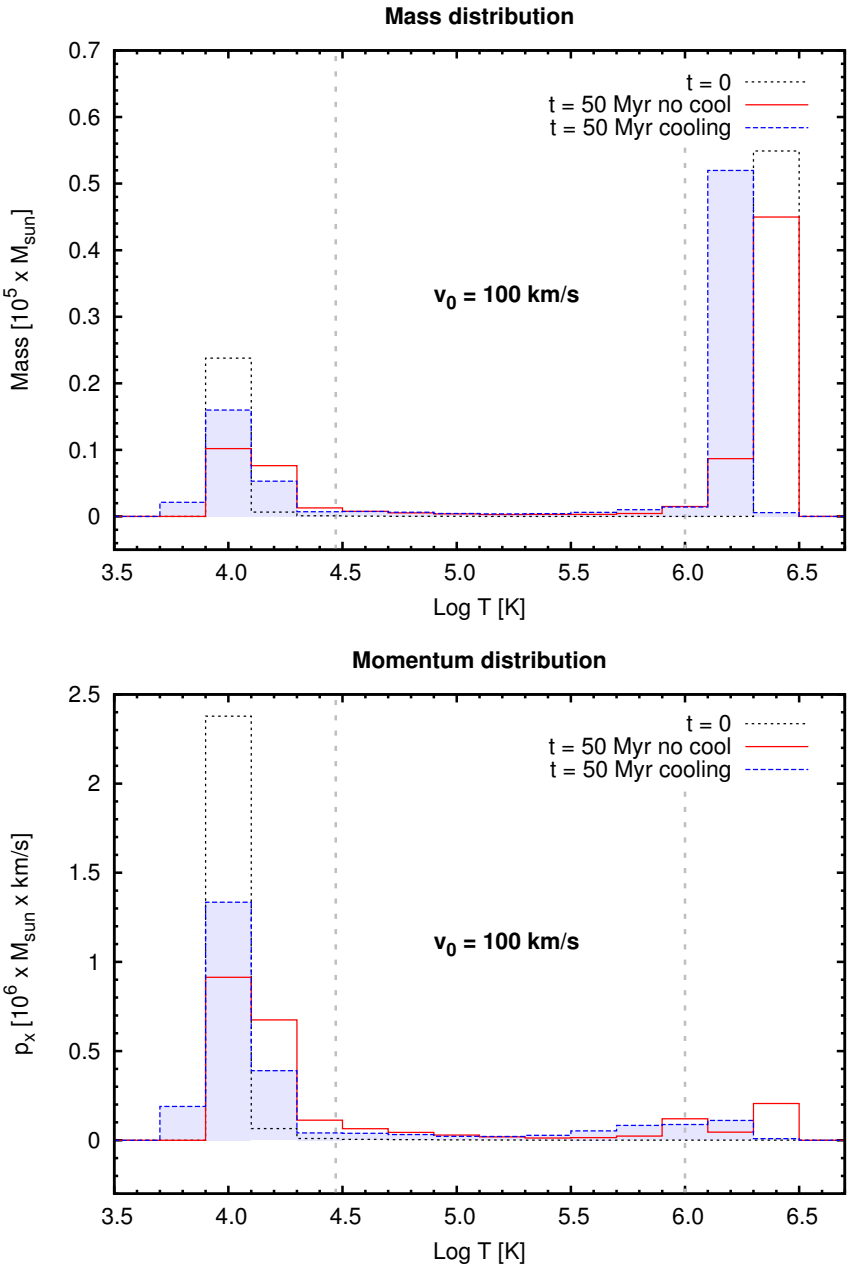

Figure 5.4: Distributions of mass (upper panel) and momentum (lower panel) as functions of the gas temperature after 50 Myr of evolution of the the adiabatic (solid line) and dissipative (shaded) standard simulations with $v_0 = 100\,\mathrm{km\,s^{-1}}$; the black short-dashed line is the initial mass or momentum distribution. The vertical grey dashed lines represent the temperature cuts used to define cold and hot gas phases.

this gas is in the temperature range $T \simeq 1 - 5 \times 10^5\,\mathrm{K}$ in which the cooling function reaches its maximum, it can cool very effectively. The consequence of this cooling is a mass transfer from the corona towards the cold gas. The momentum removed from the cold cloud is thus retained by the cooling gas and never transferred to the coronal gas. If the cooling is not present, the process of condensation of the mixed gas cannot occur and therefore the cloud continues to transfer its momentum to the mixed gas and thus to the corona.

5.3.2 Motion of the cold gas

To quantify the deceleration of the cloud, as a consequence of the momentum that the latter transfers to the background, we monitor, in the simulations, the evolution of the cloud's centroid velocity, defined as the total momentum of the cold gas along the cloud's direction of motion x divided by the total mass of the cold gas. The centroid velocity is then compared to the analytic estimate derived in Fraternali & Binney (2008)

$$v(t) = \frac{v_0}{1 + t/t_{\mathrm{drag}}}, \tag{5.1}$$

where the characteristic drag time is given in terms of the cloud's initial mass M_{cl}, geometrical cross section σ, and coronal density ρ_{cor}, by

$$t_{\mathrm{drag}} = \frac{M_{\mathrm{cl}}}{v_0 \sigma \rho_{\mathrm{cor}}}. \tag{5.2}$$

Figure 5.5 shows the centroid velocity for the dissipative (stars) and adiabatic (plus signs) standard simulations with $v_0 = 200\,\mathrm{km\,s^{-1}}$ (top), $v_0 = 100\,\mathrm{km\,s^{-1}}$ (centre) and $v_0 = 75\,\mathrm{km\,s^{-1}}$ (bottom). In the right and upper axes of the diagrams normalised units (v_0 for velocities and r_{cl}/v_0 for times) are displayed to allow an easier comparison for simulations with different initial cloud velocities. It is clear that the analytic formula (solid black line in each diagram) is a good description of the general behaviour of cold gas motion over $\sim 60\,\mathrm{Myr}$ only when the cooling is not allowed and the initial relative speed is sufficiently low (see bottom panel in the figure).

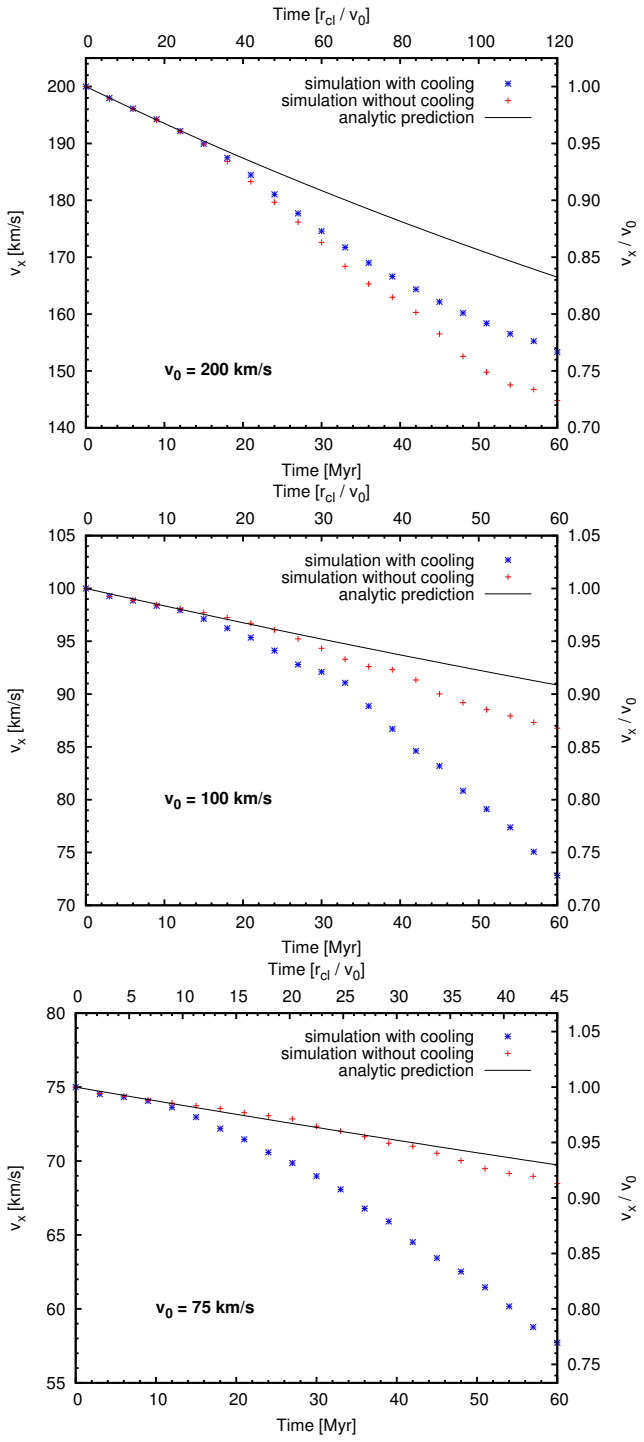

Figure 5.5: Evolution of the centroid velocity, along the cloud's direction of motion, of cold gas in the dissipative (stars) and adiabatic (plus signs) standard simulations with $v_0 = 200\,\mathrm{km\,s^{-1}}$ (top panel), $v_0 = 100\,\mathrm{km\,s^{-1}}$ (central panel) and $v_0 = 75\,\mathrm{km\,s^{-1}}$ (bottom panel). The solid lines are the theoretical predictions in the case of a quadratic drag (equation 5.1).

When these conditions are not satisfied, the analytic formula fails after some time, mainly because the Kelvin-Helmholtz instability strips some cold gas and the ram pressure progressively squashes the cloud increasing its cross section. The net effect is an enhancement of drag effectiveness (see equation 5.2). In all the dissipative standard simulations, independently of the initial speed v_0, after 60 Myr the centroid velocity is $\sim 0.75\ v_0$, significantly lower than the values predicted by equation (5.1), which treats the cloud as a rigid body. This discrepancy is due to a combination of cloud deformation, hydrodynamical instabilities and condensation of cooling gas.

For what concerns the evolution of the centroid velocity in the presence and in the absence of cooling, it must be noticed that in normalised units the evolution of the centroid velocity is basically the same in all the adiabatic simulations (in the overlapping normalised time intervals). In particular, the deviation from the analytic estimate becomes apparent at roughly the same normalised time and it can be ascribed mainly to the flattening of the main body of the cloud. In the presence of cooling, the deviation of the cloud speed from the analytic estimate is remarkably insensitive to the initial speed, but if anything it decreases as the initial speed increases, at least at the highest speeds. In these dissipative cases the amount of gas that transfers from the hot to the cold phase has an appreciable impact on the centroid velocity, so the simulations are no longer merely looking at the slowing of the original cloud, and the deceleration is dominated by condensation of cooling material that was originally at rest.

5.3.3 Momentum of the hot gas

The total momentum transferred to the hot gas by the interaction with the cold cloud is computed by summing, over the whole computational domain, the momentum of the cells containing gas at $T > 10^6$ K. Figure 5.6 shows the amount of momentum, along the cloud's direction of motion x, acquired by the hot gas as a function of time for the dissipative (stars) and adiabatic (plus signs) standard simulations with $v_0 = 200,\ 100,\ 75\,\mathrm{km\,s^{-1}}$. From

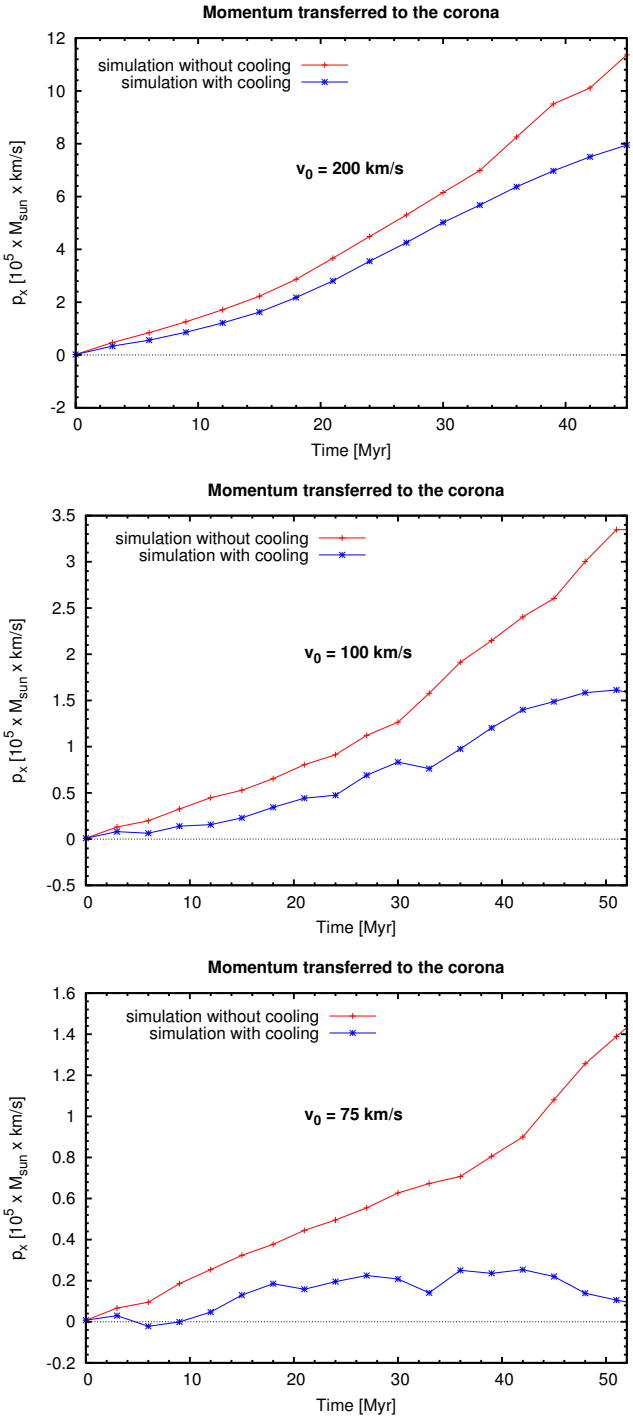

Figure 5.6: Evolution of momentum acquired by the corona as a function of time in the dissipative (stars) and adiabatic (plus signs) standard simulations with $v_0 = 200,\ 100,\ 75\ \mathrm{km\,s^{-1}}$ (from top to bottom). For comparison, it should be noted that the total initial momentum of the cloud is $2.4\times10^6\ (v_0/100\,\mathrm{km\,s^{-1}})$.

these diagrams it is apparent that the hot gas gains less momentum in the presence than in the absence of radiative cooling. The ratio between the final coronal momentum in the dissipative and in the adiabatic simulations is ~ 0.8 when $v_0 = 200\,\mathrm{km\,s^{-1}}$ (top panel), ~ 0.5 when $v_0 = 100\,\mathrm{km\,s^{-1}}$ (middle panel), and $\lesssim 0.1$ when $v_0 = 75\,\mathrm{km\,s^{-1}}$ (bottom panel). In particular, when $v_0 = 75\,\mathrm{km\,s^{-1}}$ the momentum transferred from the cold gas to the corona, after an initial phase of growth lasting for $\sim 20\,\mathrm{Myr}$, settles to a nearly constant value: from that moment onwards, the momentum transferred to the corona is consistent with zero. Thus, the simulations indicate the existence of a *velocity threshold* v_{th} below which the transfer of momentum from the cold clouds to the corona is suppressed. Given that the cloud keeps losing momentum (Figure 5.5) and the total momentum is conserved, it follows that the momentum lost by the cloud is retained by the coronal gas, which is progressively cooling in the cloud's wake.

The measure of the momentum transferred from the cold to the hot gas can be affected by the flow of coronal gas (and associated momentum) through the open boundaries of the computational domain. This effect becomes non-negligible only in the last $\sim 10\,\mathrm{Myr}$ of the simulations, so $\sim 50\,\mathrm{Myr}$ is taken as final time, as far as the measure of the coronal momentum is concerned (see also Figure 5.4). As an additional test we ran a simulation with the same initial condition as the standard simulation with $v_0 = 100\ \mathrm{km\,s^{-1}}$, but with twice the number of grid points in the direction perpendicular to the cloud's direction of motion (keeping the resolution fixed and thus effectively doubling the size of the domain), and we found relative differences in the actual value of the momentum transferred to the corona within 8%.

Since the density of the corona strongly influences the cooling rate of the gas, two additional sets of simulations with half and twice the above coronal density were run, to assess the influence of this parameter on the velocity threshold. In particular two simulations with higher density ($v_0 = 75, 100\,\mathrm{km\,s^{-1}}$) and three simulations with lower density ($v_0 = 50$,

75, $100\,\mathrm{km\,s^{-1}}$; see Table 5.1) were performed. In a denser corona, due to the increased cooling rate, the value of the velocity threshold rises to $\approx 85\,\mathrm{km\,s^{-1}}$. In the case of the less dense corona, momentum is transferred significantly also when $v_0 = 75\,\mathrm{km\,s^{-1}}$, but when $v_0 = 50\,\mathrm{km\,s^{-1}}$ the momentum transfer is consistent with zero, so $v_{\mathrm{th}} \approx 50\,\mathrm{km\,s^{-1}}$. This means that the actual value of the velocity threshold v_{th} is sensitive to the coronal density, and therefore uncertain. However, $v_{\mathrm{th}} \approx 50 - 85\,\mathrm{km\,s^{-1}}$ may be considered as a fiducial range for the velocity threshold, provided that in Milky-Way like galaxies the actual average coronal density within a few kiloparsecs above the plane is in the explored interval $0.5 - 2 \times 10^{-3}\,\mathrm{cm^{-3}}$.

5.4 Implications for galactic coronae and cold extra-planar gas

5.4.1 Rotating coronae

Fraternali & Binney (2008) showed that if a significant part of the momentum lost by H I clouds through ram-pressure drag is absorbed by the corona, the spin of the latter will increase on a timescale that is short even compared to the orbital time ($\sim 100\,\mathrm{Myr}$) of an individual cloud. If the corona did not rotate, the velocity differences between it and individual clouds would be dominated by the cloud's azimuthal motion, and being $\gtrsim 200\,\mathrm{km\,s^{-1}}$ would exceed the velocity threshold v_{th}. Consequently, the corona would gain a significant fraction of the momentum lost by clouds, acquiring substantial angular momentum on a short timescale. Hence the rotation rate of the corona must be determined by the condition that the relative velocity of a typical cloud and the corona is $\lesssim v_{\mathrm{th}}$. Since clouds are travelling with an average vertical velocity $\langle v_z \rangle \sim 40\,\mathrm{km\,s^{-1}}$ (Marasco & Fraternali 2011), the rotational lag required for this condition to be satisfied is $v_{\mathrm{lag}} \sim \sqrt{v_{\mathrm{th}}^2 - \langle v_z \rangle^2}$. For the estimate of $v_{\mathrm{th}} \approx 75\,\mathrm{km\,s^{-1}}$ given above, one obtains $v_{\mathrm{lag}} \sim 65\,\mathrm{km\,s^{-1}}$. Thus, coronae of galaxies like the Milky Way are expected to be quite rapidly rotating.

To compute the difference in rotation velocity between the corona and the disc at a given height, one must subtract the value for $v_{\rm lag}$ determined above to the value of the rotation velocity of the H I at that height. In the Milky Way this difference is $\approx 95\,{\rm km\,s^{-1}}$ at $z \simeq 2\,{\rm kpc}$, assuming a vertical gradient for the H I of $\simeq -15\,{\rm km\,s^{-1}\,kpc^{-1}}$ (Marasco & Fraternali 2011), and corresponds to a coronal rotation velocity of $\approx 125\,{\rm km\,s^{-1}}$ for $v_\odot = 220\,{\rm km\,s^{-1}}$.

The fact that the corona is rotating, even at speeds lower than that of the galactic disc, has important consequences for its morphology. In general, the azimuthal velocity v_φ of the corona can depend on both distance from the centre R and height above the plane z, as is the case of baroclinic distributions (Poincaré-Wavre theorem; Lebovitz 1967; Tassoul 1978; Barnabè et al. 2006). The z dependence might be expected in analogy with the observed kinematics of the cold extra-planar gas, and also as a consequence of the momentum transfer between fountain clouds and hot gas. By recalling the procedure outlined above, the lag of the corona with respect to the disc should vary from ≈ 70 to $120\,{\rm km\,s^{-1}}$ going from $z = 0.5\,{\rm kpc}$ to $z = 4\,{\rm kpc}$, which is the typical region where fountain clouds are located. This corresponds to a rotational velocity of $\approx 150 - 100\,{\rm km\,s^{-1}}$, assuming again $v_\odot = 220\,{\rm km\,s^{-1}}$. However, given the large uncertainty on the properties of the corona, much simpler (barotropic) models of coronae, in which $v_\varphi = v_\varphi(R)$, are considered here. We built isothermal ($T = 2 \times 10^6\,{\rm K}$) models of coronae in equilibrium in the axisymmetric gravitational potential of the Milky Way, as given by Binney & Tremaine (2008), with rotation law

$$v_\varphi(R) = v_{\rm s} \frac{R}{R + R_{\rm s}}. \tag{5.3}$$

The rotation is null at the centre and raises up to the terminal value $v_{\rm s}$: the rise of the rotation velocity is steeper for smaller values of $R_{\rm s}$. To match the expected rotational velocity range, in Figure 5.7 the meridional isodensity contours of two models with $v_{\rm s} = 100\,{\rm km\,s^{-1}}$ (upper panel) and $v_{\rm s} = 150\,{\rm km\,s^{-1}}$ (lower panel) are presented. In both cases $R_{\rm s} = 1\,{\rm kpc}$. The

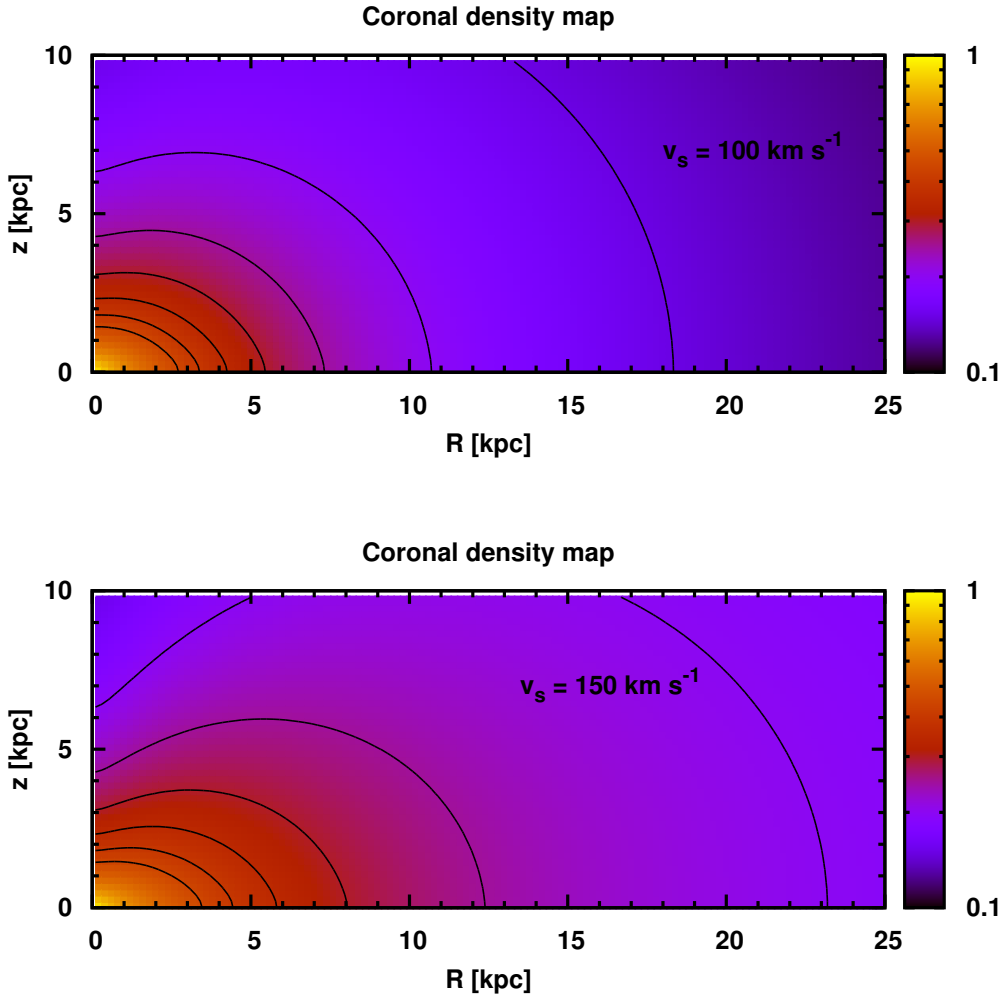

Figure 5.7: Meridional density distribution of a rotating isothermal ($T = 2 \times 10^6$ K) corona in the Milky-Way potential for two asymptotic values of the rotational velocity v_s (see equation 5.3). The density is normalised to the central ($R = z = 0$) value and the values on the contours are 0.45, 0.4, 0.35, 0.3, 0.25, 0.2, 0.15 (the lowest contour is not visible in the bottom panel).

resulting gas distributions are peanut-shaped, with axis ratio of the isodensity surfaces in the range $0.5-0.7$. Therefore, if galactic coronae rotate with speeds of the order of those predicted by the simulations presented in this Chapter, they will appear significantly flattened when detected in future X-ray observations. It should be noted that this peanut-shaped structure is also predicted in the general baroclinic case (Barnabè et al. 2006).

5.4.2 Vertical velocity gradient of the cold extra-planar gas

The simulations presented here clearly indicate that clouds of cold gas ejected above the disc plane can lose angular momentum via interaction with the hot medium. This mechanism appears as a natural explanation for the observed vertical gradient in the rotation velocity of the extra-planar gas of disc galaxies. Unfortunately, a comparison between the results of the simulations and the observations is not straightforward, mainly because of the idealised nature of the simulations, in which the galaxy's gravitational field is not included and thus the cloud's orbit above the plane cannot be followed. However, the results obtained from the simulations presented in this Chapter can be used to obtain a rough estimate of the expected vertical rotational gradient of the extra-planar gas, by using the following argument. To simplify the treatment let us hypothesise that a cloud, ejected with a velocity orthogonal to the disc plane at some radius R, falls back on to the plane, after a time of the order of 100 Myr, at about the same radius R. Assuming a mean velocity for the ascending part of the orbit $\langle v_z \rangle = 40\,\mathrm{km\,s^{-1}}$ (Marasco & Fraternali 2011) and a mean maximum height above the disc for the cold clouds $\langle z_{\mathrm{max}} \rangle = 2\,\mathrm{kpc}$, the time to reach the maximum height is

$$t_{\mathrm{orb}} = \frac{\langle z_{\mathrm{max}} \rangle}{\langle v_z \rangle} \approx 50\,\mathrm{Myr}\,. \tag{5.4}$$

Thus, neglecting for the moment any change in R along the orbit, the rotational-velocity gradient of the cold gas can be estimated as

$$\frac{\Delta v_\varphi}{\Delta z} = \frac{\Delta v}{\langle z_{\rm max} \rangle}\,, \tag{5.5}$$

where $\Delta v \equiv v(t_{\rm orb}) - v_0$ is the difference between the centroid velocity of the cold gas after $t_{\rm orb}$ and its initial velocity. In the hypothetical case of a static corona ($v_0 = 200\,{\rm km\,s^{-1}}$) $\Delta v \approx 40\,{\rm km\,s^{-1}}$ (see Figure 5.5), so

$$\frac{\Delta v_\varphi}{\Delta z} \approx -20\,{\rm km\,s^{-1}\,kpc^{-1}}\,, \tag{5.6}$$

while in the case of a spinning corona (such that $v_0 = 75\,{\rm km\,s^{-1}}$)

$$\frac{\Delta v_\varphi}{\Delta z} \approx -7\,{\rm km\,s^{-1}\,kpc^{-1}}\,, \tag{5.7}$$

based on the results of the dissipative simulation v75. The effect of radiative cooling is crucial for the estimate of the gradient: using the adiabatic $v_0 = 75\,{\rm km\,s^{-1}}$ simulation one would get instead

$$\frac{\Delta v_\varphi}{\Delta z} \approx -3\,{\rm km\,s^{-1}\,kpc^{-1}}. \tag{5.8}$$

In the Milky Way the observed gradient is $\simeq -15\,{\rm km\,s^{-1}\,kpc^{-1}}$ (Marasco & Fraternali 2011), and similar values have been determined in external nearby galaxies. As mentioned, the above estimates neglect the variation of R along the orbit, which by conservation of angular momentum induces a variation in v_φ. Fraternali & Binney (2008) showed that this effect alone accounts for $\approx 50\%$ of the rotational gradient of the extra-planar gas. Thus, by adding this latter contribution to the estimate in equation (5.7), one obtains values that are remarkably close to the observed gradients.

On the basis of the discussion illustrated above the following points should be remarked: (i) larger velocity gradients are expected with increasing differences in rotational velocity between the clouds and the corona, (ii) as the relative velocity decreases, the drag becomes an inefficient process to decelerate the clouds, (iii) the radiative cooling of the gas has the effect of

increasing the gradient to values which are very close to those required by the observations, and therefore (iv) the observed gradient can be explained only by a combination of cooling and drag. Overall, the obtained results are consistent with the scenario developed in Fraternali & Binney (2008), in which the accretion of gas by fountain clouds is the cause of the lagging kinematics of extra-planar gas in disc galaxies.

5.5 Summary and conclusions

In this Chapter we studied the process of the momentum transfer between cold clouds ejected from the disc and the corona of disc galaxies like the Milky Way, which has a significant impact on the kinematics of both the coronal and the cold extra-planar gas. In particular, we presented two-dimensional hydrodynamical simulations of cloud-corona interaction. In the more realistic simulations the gas is allowed to cool radiatively, but, for comparison, the corresponding adiabatic cases were also considered. The simulations are similar, but with several important improvements, with respect to those presented in Chapter 4: here a wider range of relative speeds between the cloud and the hot medium ($50 - 200\,\mathrm{km\,s^{-1}}$) was explored, the evolution of the system was followed for longer time (60 Myr), the metallicity was treated as a dynamical variable (assigning initially to the cloud a metallicity ten times higher than that of the ambient gas) and the variation with temperature of the fluid's molecular weight μ was accounted for.

The main results of the simulations are the following.

(i) There is a relative velocity threshold of about $75\,\mathrm{km\,s^{-1}}$ between the cloud and the ambient medium, below which the corona stops absorbing momentum.

(ii) Radiative cooling is crucial for the existence of this velocity threshold: in adiabatic simulations the momentum transfer from the cloud to the hot gas is quite efficient at all explored relative speeds.

(iii) The actual value of the velocity threshold for Milky-Way like galaxies depends on the coronal density: *less dense coronae have a lower velocity threshold*. In particular, in the interval of coronal densities explored by the simulations $v_{\rm th} \approx 50 - 85\,{\rm km\,s^{-1}}$.

The momentum transfer between the fountain clouds and the corona has important consequences on the kinematics of the latter. The corona cannot be static, otherwise the momentum transfer from the cold clouds would be very effective, but it cannot be rotating at a speed close to the rotation speed of the disc, because at low relative disc-corona (and thus cloud-corona) velocity the cooling hampers any momentum transfer. In a galaxy like the Milky Way the corona is expected to lag, in the inner regions, by $\approx 100\,{\rm km\,s^{-1}}$ with respect to the cold disc at $z \simeq 2\,{\rm kpc}$ and thus to rotate at a speed of $100 - 150\,{\rm km\,s^{-1}}$ within 4 kpc from the disc. Such a spinning corona must be characterised by a significantly flattened density distribution: based on simple isothermal models, values of the axis ratios of the isodensity surfaces in the range $0.5 - 0.7$ can be estimated.

Due to interaction with the corona, fountain clouds gain mass and decelerate: based on the calculations carried out in Section 5.4.2, this effect can account for $\approx -7\,{\rm km\,s^{-1}\,kpc^{-1}}$ of the vertical gradient in rotational speed of the extra-planar gas in galaxies like the Milky Way. Such a value can be sufficient to reconcile purely ballistic fountain models with the observed kinematics of the H I extra-planar gas, giving further support to the "fountain plus accretion" model of Fraternali & Binney (2008).

In conclusion, the presented results contribute quantitatively to refine an emerging consistent scenario in which galactic fountains, cold extra-planar gas and galactic coronae are strictly interlaced. This scenario makes specific predictions that can be tested in the future with soft X-ray observations detecting the elusive galactic coronae and with H I measures of cold extra-planar gas in a large sample of galaxies.

6

Concluding remarks

6.1 Thesis summary

In this Thesis we have studied the dynamics of the hot and cold gas outside the plane in disc galaxies (extra-planar gas) and investigated the interaction between disc and halo material. This study has the final goal of furthering our understanding of the evolution of star-forming galaxies like the Milky-Way.

Extra-planar gas is detected in emission in several nearby spiral galaxies at different wavelengths. These observations have shown that the extra-planar gas is a multiphase medium, composed by a cold neutral H I phase (Fraternali et al. 2002; Marasco & Fraternali 2011), a warm ionised component detected in Hα and optical emission lines (Rand 2000; Rossa et al. 2004; Heald et al. 2007), and a hot X-ray emitting phase (Strickland et al. 2004). In edge-on galaxies, such as NGC 891, neutral H I extra-planar emission has been traced up to $10-20$ kiloparsecs form the disc (Oosterloo et al. 2007). The origin of the extra-planar gas is still debated. However, there are strong indications that most of it is ejected from the star-forming disc by stellar activity (i.e. supernova explosions and galactic winds) through

the so-called galactic fountain mechanism (Bregman 1980), and only a minor fraction of its mass is likely to be material of extra-galactic origin that is accreting on to the galaxy (Sancisi et al. 2008; Fraternali 2010).

In Chapter 2 of this Thesis we presented stationary models for the cold phase of the extra-planar gas. Their main aim was to reproduce the peculiar kinematics of this gas, which is characterised by a regular decrease in the rotation velocity with increasing distances from the mid-plane (vertical gradient). In this approach, the (cold) extra-planar gas is modeled as a system of non-interacting clouds in permanent rotation that obey the stationary Jeans equations. In particular, we have computed several models for the well studied case of the disc galaxy NGC 891, changing the form of the velocity dispersion tensor, and we have compared our results with the available H I observations. The comparison was made by constructing an artificial cube for each model with the same resolution and total flux as the H I data cube of the galaxy. In this way a complete control of resolution and projection effects was possible. We found that none of the models investigated can reproduce the kinematics of the extra-planar gas in detail as they systematically predict: (i) high values of the velocity dispersion along the line-of-sight and/or (ii) a too shallow vertical gradient (see Section 2.4). This fact suggests that, in agreement with previous studies (e.g. Fraternali & Binney 2006, 2008), interactions with the ambient medium, by which H I clouds are pressure confined, cannot be neglected and play, indeed, an important dynamical role.

Thus, the main part of this work was devoted to the study of this interaction between fountain clouds and the ambient medium, which we assumed to be the cosmological corona of gas at virial temperature that surrounds galaxies like the Milky-Way. In the region close to the galactic disc (cold) fountain clouds should travel through the ubiquitous gas of the corona, and an interaction between the two phases is inevitable.

In Chapters 4 and 5 of this Thesis we simulated the mass and momentum exchange between these two phases. To understand this process we have

carried out a set of two-dimensional hydrodynamical simulations to study the evolution of a cloud of cool gas travelling through a more tenuous and hotter medium representing the galactic corona. To perform these simulations we have implemented a novel hydrodynamical code, called ECHO++, based on the high-order algorithms in Del Zanna et al. (2007). Details of the implementation are presented in Chapter 3.

Simulations have shown that the condensation of the coronal gas prevails over the evaporation of the clouds if the metallicity and the pressure of the corona are high enough (see Chapter 4). The process can be described as follows. The cloud, moving through the corona, is stripped of some of its gas due to Kelvin-Helmholtz instability. In the turbulent wake that forms behind the cloud, the stripped gas mixes with a comparable amount of hot coronal gas, lowering its temperature, increasing its metallicity and decreasing its cooling time. As a result, the coronal gas condenses in the turbulent wake of the cloud. So there is a net transfer of mass from the hot corona to the cold phase. The extrapolated rate at which the gas condenses out of the corona is remarkably close to the value of ~ 1 $\mathrm{M}_{\odot}$ yr^{-1}, which is necessary to feed star formation in a galaxy like the Milky-Way (Sancisi et al. 2008). In particular, if the cold clouds were able to accrete or transfer some of the coronal gas on to the disc, we would have a promising mechanism to feed star formation in star-forming galaxies. In fact, it has been estimated that, in absence of any fresh supply of gas, star-forming galaxies should exhaust the available fuel in a few gigayears.

The transfer of momentum between the clouds and the corona is discussed in Chapter 5. We found that this process is strongly influenced by the radiative cooling of the gas, the net effect being a reduction of the transferred momentum from the cold to the hot gas when the cooling is switched on. Moreover, there appears to be a velocity threshold between the two phases of about $75\,\mathrm{km\,s^{-1}}$, below which the hot gas does not absorb any more momentum from the cold clouds. Below this threshold the momentum lost by the cold phase is transferred to the gas that promptly

cools (in the cloud's wake) from the virial temperature down to $T \lesssim 10^5\,\mathrm{K}$. If the relative velocity between the cold and the hot gas is dominated by the azimuthal component (i.e. by the difference in rotation velocity), we predict that coronae of disc galaxies should lag with respect to the cold disc by $80 - 120\,\mathrm{km\,s^{-1}}$ in a region within 4 kpc from it. This has a significant impact on the morphology of these structures, because a spinning corona flattens to a toroidal configuration in which some of the gas is removed from the central regions and redistributed outwards. This prediction will be tested by future X-ray observations. Finally, by studying the deceleration of the cloud centroid, we can also estimate the expected vertical velocity gradient of the cold extra-planar gas. The value that we found is remarkably close to the gradients observed in nearby disc galaxies.

Implications and possible future developments of these results for the evolution of galaxies and for the large-scale dynamics of galactic coronae will be briefly outlined in the next Sections.

6.2 Evolution of galactic discs

Star-forming galaxies like the Milky-Way have formed stars at a fairly constant rate during their life time (Twarog 1980; Cignoni et al. 2006). In addition, it appears that the gas content of these galaxies has remained approximately unchanged throughout the Hubble time (Hopkins et al. 2008; Bauermeister et al. 2010). Typically, the mass of gas contained in the thin disc can sustain the process of star formation for a few gigayears only and thus, at any given cosmic epoch, Milky-Way type galaxies need some supply of external gas to be brought into the disc, at a rate of $\sim 1\ \mathrm{M_\odot\,yr^{-1}}$, that compensates the conversion of gas into stars (Sancisi et al. 2008). To sustain such an accretion rate for a Hubble time a cosmologically significant reservoir of gas is needed. There are strong indications from cosmological arguments that the gas accreted by galaxies to form stars must ultimately come from the intergalactic medium, which accumulates around galaxies

like our own in the form of a virial-temperature corona (see Section 6.3). Hence, in this scenario, the evolution of a star-forming disc is strongly influenced by the circulation of gas between the galaxy and its environment.

Simulations described in Chapters 4 and 5 have shown that the hot ($\sim 10^6\,\mathrm{K}$) coronal gas can be efficiently cooled by the interaction with colder ($\sim 10^4\,\mathrm{K}$) fountain gas in regions within a few kiloparsecs from the galactic disc. Thus, coronal gas condenses into the clouds wakes becoming the material by which star-forming galaxies may sustain star formation at the current observed rates ($\sim 1\ \mathrm{M_\odot\,yr^{-1}}$). For this process to work it is necessary that the cold gas in the wake is brought into the thin disc in a cloud dynamical time ($\sim 100\,\mathrm{Myr}$). Although the cold gas in the wake is relatively close (within 1.5 kpc, see Chapter 5.3.1) to the main body of the cloud, it is not completely clear whether it can follow this latter on its orbit down to the star-forming disc, because the simulations presented so far neglect the gravitational field of the galaxy. Therefore, further investigations are required to test this scenario.

In Figure 6.1 we present temperature snapshots, coming from a preliminary analysis of two-dimensional simulations of cloud-corona interaction that include the vertical gravitational field of the galaxy. These simulations investigate the evolution of a cloud of cold ($T_{\mathrm{cl}} = 10^4\,\mathrm{K}$) gas and radius $r_{\mathrm{cl}} = 100\,\mathrm{pc}$ that is shot upwards with an angle of 10° with respect to the normal to the plane and a velocity $v_0 = 75\,\mathrm{km\,s^{-1}}$. The cloud is initially in pressure equilibrium with an ambient medium at $T_{\mathrm{cor}} = 2 \times 10^6\,\mathrm{K}$, which represents the hot corona. This hot gas is in hydrostatic equilibrium with the vertical gravitational field of the Milky-Way at the solar circle ($R_\odot = 8.5\,\mathrm{kpc}$) derived from the gravitational potential in Binney & Tremaine (2008). The density of the hot gas at the bottom side of the computational grid is $n_{\mathrm{cor}} = 10^{-3}\,\mathrm{cm^{-3}}$. Simulations are run both with (bottom diagram) and without (top diagram) radiative cooling.

In both simulations the main body of the cold gas returns to the bottom side of the computational domain, where we assume that the star-forming

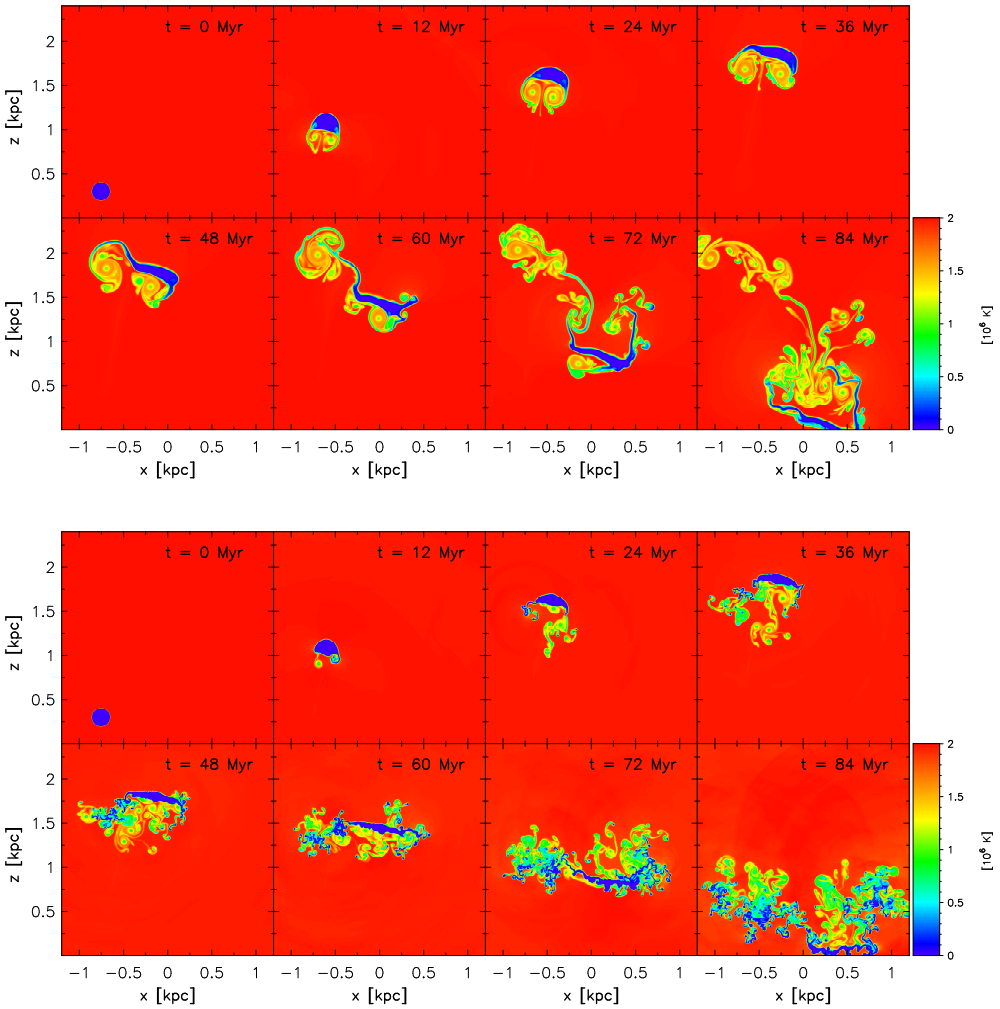

Figure 6.1: Temperature snapshots of two-dimensional simulations of cloud-corona interaction where the vertical gravitational field of the galaxy is taken into account (see text for details). The time at which each snapshot has been taken is indicated in the top right corner. Top diagram: adiabatic simulation. Bottom diagram: simulation that includes radiative cooling.

disc is located, in about 84 Myr. The evolution, however, is markedly different if the simulation is adiabatic or not. In the former case a long wake of intermediate temperature gas around 10^6 K forms, which extends in the vertical direction for approximately the whole computational domain in the 84 Myr panel, whilst in the latter the wake is much more compact in the vertical direction (although more extended along the x axis) and colder ($T \lesssim 5 \times 10^5$ K). Moreover, at $t = 84$ Myr basically all the cold gas is at $z \lesssim 0.75$ kpc. This fact seems to indicate that the gas that is condensing into the wake closely follows the motion of the fountain cloud and is indeed incorporated in the star-forming disc in a cloud dynamical time, as we suggested in Chapter 4. A first line of study opened by the present PhD work would be to run a series hydrodynamical simulations, covering a wider range in ejection velocity and coronal properties, and possibly including a realistic cloud orbit in the halo region, to confirm unambiguously this result. It would be also useful to compare the predictions of these simulations with absorption line data, such as Si II and Si III lines (Shull et al. 2009), that probe cooling material around 3×10^4 K.

It is worth pointing out that coronal gas can only condense on to a disc that is already star-forming. This is so because a spontaneous cooling of patches of the corona, due to thermal instability, has two main difficulties: (i) perturbations, which should lead to instability, are easily suppressed by buoyancy and thermal conduction, unless exceptional conditions are met (Binney et al. 2009) and even if the corona rotates significantly (Nipoti 2010); (ii) state-of-the-art numerical simulations (Kaufmann et al. 2009; Peek et al. 2008) have shown that the predicted accretion rate is only $\approx 0.2 - 0.3$ $M_\odot\,yr^{-1}$ even in the most favourable conditions. Thus, a star-forming disc, or better the cold gas ejected from it by supernova feedback, represents the catalyst that ultimately leads to the accretion of intergalactic material needed to sustain star formation. Without the catalyst the reaction (i.e. the accretion of coronal gas) cannot be initiated and star formation permanently ceases.

Evolution of the hot coronae[1] detected in X-ray around elliptical galaxies (e.g. Irwin & Sarazin 1996; Sarazin et al. 2001) is expected to be quite different from that in disc galaxies, due to the fact that (significant) star formation in ellipticals is absent. Thus, X-ray coronae of ellipticals can cool efficiently only in the central regions, where the gas density is the highest (cooling flow scenario, see Section 4.4.3). This causes a flow of gas towards the centre of the galaxy, which accretes on to the central black hole rather than forming stars. Feedback from central black hole will then reheat the corona stopping the flow.

It is likely that cooling at the centre of the corona of a disc galaxy leads to episodic reheating of the central corona, just as in a classical cooling flow scenario. That is, it is plausible that the corona of a star-forming disc galaxy accretes on to central black hole as well as on to the disc. However, if star formation has to be mantained, the central reheating associated with accretion by the black hole must not undermine the ability of the star-forming disc to grab coronal gas from the part of the corona that lies above it. This condition could be satisfied if the AGN outburst were sufficiently small and sufficiently directed perpendicular to the galactic plane.

6.3 Implications for galactic coronae

In the local Universe, baryons contained in galaxies account only for a small fraction of the cosmological baryon content. This latter value $f_b \equiv \Omega_b/\Omega_m \simeq 0.17$ is known to high precision thanks to a combination of recent studies of big-bang nucleosynthesis and cosmic microwave background (Dunkley et al. 2009). The current census of baryons in the Universe shows that locally at least 60% of the baryons are missing (Bregman 2007). These missing baryons are thought to be in the so-called Warm-Hot Intergalactic Medium (WHIM) at temperatures in the range $10^5 - 10^7$ K. In mas-

[1]The origin of these coronae is somewhat different from those of spirals, as most of the hot gas of which they are composed is originated by stellar mass loss in the galaxy (Sarazin et al. 2001).

sive clusters of galaxies the WHIM is readily detected through its free-free emission (Sarazin 2009), whilst in lower density environment, such as groups of galaxies, the X-ray surface brightness falls below the sensitivity of the current instrumentation (Rasmussen et al. 2009). In this cosmological scenario, galaxies like the Milky-Way are embedded in extended virial-temperature atmospheres, called coronae, that should contain a significant fraction ($\gtrsim 50\%$) of the baryons originally linked to the dark matter halo of the galaxy. In spite of the evidence that accumulates on the existence of the galactic coronae, such as, in our Galaxy, absorption from C IV, O V, O VI ions (Sembach et al. 2003; Fox et al. 2006), their structural and kinematic parameters are largely unknown (Fukugita & Peebles 2006; Anderson & Bregman 2010).

In Chapter 4 of this Thesis, we have hypothesised that cosmological coronae, that surround star-forming galaxies, are the most likely reservoir from which these galaxies draw the gas, at a rate of $\sim 1\,\mathrm{M}_\odot\,\mathrm{yr}^{-1}$, to sustain star formation over a Hubble time. In particular, we have proposed a mechanism to explain how baryons in the corona make the transition between a pressure supported structure to a centrifugally supported disc or, in other words, how they can cool from the virial temperature down to $\sim 10^4\,\mathrm{K}$. This mechanism is based on the idea of an *induced* cooling of the coronal gas. The basic process is that the interaction of the corona with colder and more metal rich fountain gas outside the plane of the galaxy enhances the cooling rate of the coronal gas. In this way, gas accretion from the corona can occur everywhere on top of the star forming disc and at a fast rate. Another important aspect of the interaction between the gas ejected from the disc by supernova feedback and the corona is represented by the exchange of (angular) momentum between the two phases, which was investigated in Chapter 5. In that Chapter we have shown that, as a consequence of this process, coronae are likely to be rotating flattened structures, which lag by $\sim 80 - 120\,\mathrm{km\,s}^{-1}$ with respect to the cold disc.

To better understand the relationships between star-forming galaxies

and the intergalactic environment where they form and evolve, investigations of the large-scale dynamics of galactic coronae, which is induced by the interaction with the galactic fountain, are needed. Of a particular interest is the redistribution of mass and angular momentum from the central region to the outskirts of galactic coronae. In the central region (i.e. the region close to the disc), the supernova feedback transfers angular momentum, as long as the relative velocity between the fountain and the coronal gas reaches a threshold value, and enhances the cooling rate of the coronal gas, possibly removing the condensing gas by accreting it on to the disc. In the investigations described above, the effects of these two processes have been analysed only on a local scale due to the fact that resolution of very small scales (of the order of ~ 1 pc) is necessary to capture all the details of the mixing process.

The consequences of the interaction between the fountain gas and the corona cannot be confined to the region near the disc for a very simple motivation: the fountain gas contained in these regions has a mass which is more than 2 times the mass of the coronal gas in the same region and, in addition, it is continuously cycling through the halo on a timescale of $\sim 100\,\mathrm{Myr}$. This implies that the coronal gas interacts in say 1 Gyr with a mass of fountain gas $\gtrsim 20$ times its own mass, and thus it is very unlikely that the corona is affected by this interaction on a limited spatial extension only. Moreover, assuming for the Milky-Way a fiducial value of $\sim 10^8$ $\mathrm{M}_\odot$ for the mass coronal gas near the disc (see Section 4.2.1), it can be readily seen that this gas must be accreted on a timescale of $\sim 100\,\mathrm{Myr}$ to satisfy star formation requirements. Therefore, almost all the coronal gas is removed from the central regions on a relatively short timescale. This causes a lack of pressure support against gravity which ultimately causes a flow of gas from the external regions of the corona towards the centre that will replenish again the region near the star-forming disc. The flow of gas is complicated by the fact that the fountain gas surrenders a significant fraction of its angular momentum to the coronal gas and thus, at least in

the central region, the corona will be a rotating structure, although with a rotation velocity less than that of the star-forming disc.

Full three-dimensional hydrodynamical simulations are required to study the large-scale dynamics of galactic coronae. However, direct simulations are difficult to undertake because of the large range of scales involved in the problem: galactic coronae should have radii of hundreds of kiloparsecs, while to describe the mixing between the fountain gas and the coronal gas it is necessary to resolve scales of the order of $\sim 1\,\mathrm{pc}$. This large range of physical scales is a serious issue, in three-dimensional simulations, even with state-of-the-art Adaptive Mesh Refinement codes. Thus, a different treatment of the interaction is needed. One possibility is to consider the interaction process between the coronal gas and the fountain as a source of mass, momentum, and cooling term for the corona, and it is possible to include these effects, with a suitable parametrization, as source terms in the Euler equations (3.1), (3.2) and (3.3). Chemical enrichment of the coronal gas (which has primordial metal abundances) due to the mixing with the approximately solar metallicity ([Fe/H] ~ 0) fountain gas can be parametrized in a similar way. This is a critical aspect for the cooling of the coronal gas, given the strong dependence of radiative losses upon metallicity.

The aim of these simulations would be to follow the evolution of a galactic corona, which interacts with the gas produced by supernova feedback and is initially in hydrostatic equilibrium with the dark matter halo of the galaxy. Simulations would have to span a variety of initial conditions: for instance the temperature and density profiles of galactic coronae are virtually unconstrained by observations, and thus it is necessary to investigate the evolution of coronal models with different initial profiles, from isothermal to adiabatic. The crucial point is to determine whether the coronal gas accreted by the disc can be efficiently replaced by that coming from the external regions so that star formation can be sustained for the whole life time of the galaxy. Moreover, by consistently varying the strength of the in-

teraction with supernova feedback, it would be possible to model the effect of different star formation rates (SFR) on the global dynamics of cosmological galactic coronae. To investigate the mutual interaction between star formation and gas accretion, simulations should cover the range from nearly inactive (SFR $\sim 0.1\ \mathrm{M_\odot\,yr^{-1}}$) to active (SFR $\sim 5\ \mathrm{M_\odot\,yr^{-1}}$) star-forming galaxies.

The study of large-scale dynamics of cosmological galactic coronae is a second line of study opened by the results of this PhD work and it would give fundamental clues on the processes of transfer of gas from the intergalactic medium to the galactic discs and its importance in the context of galactic evolution.

References

Anderson M. E., Bregman J. N., 2010, ApJ, 714, 320

Barnabè M., Ciotti L., Fraternali F., Sancisi R., 2006, A&A, 446, 61

Bauermeister A., Blitz L., Ma C., 2010, ApJ, 717, 323

Benjamin R. A., 2002, in A. R. Taylor, T. L. Landecker, & A. G. Willis ed., Seeing Through the Dust: The Detection of HI and the Exploration of the ISM in Galaxies Vol. 276 of Astronomical Society of the Pacific Conference Series, The Interstellar Disk-Halo Connection: The Rotation of Extra-planar Gas. p. 201

Binney J., Nipoti C., Fraternali F., 2009, MNRAS, 397, 1804

Binney J., Tremaine S., 2008, Galactic Dynamics: Second Edition. Princeton University Press

Boomsma R., Oosterloo T. A., Fraternali F., van der Hulst J. M., Sancisi R., 2008, A&A, 490, 555

Bregman J. N., 1980, ApJ, 236, 577

Bregman J. N., 2007, ARA&A, 45, 221

Brüns C., Kerp J., Pagels A., 2001, A&A, 370, L26

References

Bryan G. L., Norman M. L., 1997, in D. A. Clarke & M. J. West ed., Computational Astrophysics; 12th Kingston Meeting on Theoretical Astrophysics Vol. 123 of Astronomical Society of the Pacific Conference Series, Simulating X-Ray Clusters with Adaptive Mesh Refinement. p. 363

Cappellari M., 2008, MNRAS, 390, 71

Chiappini C., Matteucci F., Romano D., 2001, ApJ, 554, 1044

Cignoni M., Degl'Innocenti S., Prada Moroni P. G., Shore S. N., 2006, A&A, 459, 783

Ciotti L., Pellegrini S., 1996, MNRAS, 279, 240

Collins J. A., Benjamin R. A., Rand R. J., 2002, ApJ, 578, 98

Collins J. A., Rand R. J., Duric N., Walterbos R. A. M., 2000, ApJ, 536, 645

Dehnen W., Binney J., 1998, MNRAS, 294, 429

Del Zanna L., Bucciantini N., 2002, A&A, 390, 1177

Del Zanna L., Zanotti O., Bucciantini N., Londrillo P., 2007, A&A, 473, 11

Dinge D., 1997, ApJ, 479, 792

Dunkley J., Komatsu E., Nolta M. R., Spergel D. N., Larson D., Hinshaw G., Page L., Bennett C. L., Gold B., Jarosik N., Weiland J. L., Halpern M., Hill R. S., Kogut A., Limon M., Meyer S. S., Tucker G. S., Wollack E., Wright E. L., 2009, ApJS, 180, 306

Fox A. J., Savage B. D., Wakker B. P., 2006, ApJS, 165, 229

Fraternali F., 2010, in V. P. Debattista & C. C. Popescu ed., American Institute of Physics Conference Series Vol. 1240 of American Institute of Physics Conference Series, Gas Circulation and Galaxy Evolution. pp 135–145

Fraternali F., Binney J., Oosterloo T., Sancisi R., 2007, NewAR, 51, 95

Fraternali F., Binney J. J., 2006, MNRAS, 366, 449 (FB06)

Fraternali F., Binney J. J., 2008, MNRAS, 386, 935 (FB08)

Fraternali F., Oosterloo T., Sancisi R., 2004, A&A, 424, 485

Fraternali F., Oosterloo T., Sancisi R., van Moorsel G., 2001, ApJL, 562, L47

Fraternali F., Oosterloo T. A., Sancisi R., Swaters R., 2005, in R. Braun ed., Extra-Planar Gas Vol. 331 of Astronomical Society of the Pacific Conference Series, The Extra-planar Neutral Gas in the Edge-on Spiral Galaxy NGC 891. p. 239

Fraternali F., van Moorsel G., Sancisi R., Oosterloo T., 2002, AJ, 123, 3124

Fukugita M., Peebles P. J. E., 2004, ApJ, 616, 643

Fukugita M., Peebles P. J. E., 2006, ApJ, 639, 590

Garcia-Burillo S., Guelin M., 1995, A&A, 299, 657

Governato F., Willman B., Mayer L., Brooks A., Stinson G., Valenzuela O., Wadsley J., Quinn T., 2007, MNRAS, 374, 1479

Grcevich J., Putman M. E., 2009, ApJ, 696, 385

Harten A., Lax P. D., van Leer B., 1983, SIAM Rev., 5, 1

Heald G. H., Rand R. J., Benjamin R. A., Bershady M. A., 2006a, ApJ, 647, 1018

Heald G. H., Rand R. J., Benjamin R. A., Bershady M. A., 2007, ApJ, 663, 933

Heald G. H., Rand R. J., Benjamin R. A., Collins J. A., Bland-Hawthorn J., 2006b, ApJ, 636, 181

Heitsch F., Putman M. E., 2009, ApJ, 698, 1485

Helmholtz H. L. F. v., 1868, Monthly Reports of the Royal Prussian Academy of Philosophy in Berlin, 23, 215

Hoopes C. G., Walterbos R. A. M., Rand R. J., 1999, ApJ, 522, 669

Hopkins A. M., McClure-Griffiths N. M., Gaensler B. M., 2008, ApJL, 682, L13

Irwin J. A., Sarazin C. L., 1996, ApJ, 471, 683

Jiang G.-S., Shu C.-W., 1996, Journal of Comp. Phys., 126, 202

Kalberla P. M. W., Burton W. B., Hartmann D., Arnal E. M., Bajaja E., Morras R., Pöppel W. G. L., 2005, A&A, 440, 775

Kalberla P. M. W., Dedes L., 2008, A&A, 487, 951

Kamphuis P., Peletier R. F., Dettmar R., van der Hulst J. M., van der Kruit P. C., Allen R. J., 2007, A&A, 468, 951

Kaufmann T., Bullock J. S., Maller A. H., Fang T., Wadsley J., 2009, MNRAS, 396, 191

Kaufmann T., Mayer L., Wadsley J., Stadel J., Moore B., 2006, MNRAS, 370, 1612

Kelvin L., 1871, Philos. Mag., 42, 362

Kereš D., Katz N., Fardal M., Davé R., Weinberg D. H., 2009, MNRAS, 395, 160

Komatsu E., Dunkley J., Nolta M. R., Bennett C. L., Gold B., Hinshaw G., Jarosik N., Larson D., Limon M., Page L., Spergel D. N., Halpern M., Hill R. S., Kogut A., Meyer S. S., Tucker G. S., Weiland J. L., Wollack E., Wright E. L., 2009, ApJS, 180, 330

Kovač K., Oosterloo T. A., van der Hulst J. M., 2009, MNRAS, 400, 743

Landi S., Londrillo P., Velli M., Bettarini L., 2008, Physics of Plasmas, 15, 012302

Lax P. D., 1954, Comm. Pure Appl. Math., 7, 159

Lebovitz N. R., 1967, ARA&A, 5, 465

Liu X.-D., Osher S., 1998, Journal of Comp. Phys., 142, 304

Lo K. Y., Sargent W. L. W., 1979, ApJ, 227, 756

Mac Low M., McCray R., 1988, ApJ, 324, 776

Marasco A., Fraternali F., 2011, A&A, 525, 134

Marinacci F., Binney J., Fraternali F., Nipoti C., Ciotti L., Londrillo P., 2010a, MNRAS, 404, 1464

Marinacci F., Fraternali F., Ciotti L., Nipoti C., 2010b, MNRAS, 401, 2451

Marinacci F., Fraternali F., Nipoti C., Binney J., Ciotti L., Londrillo P., 2011, submitted to MNRAS

Mignone A., Bodo G., Massaglia S., Matsakos T., Tesileanu O., Zanni C., Ferrari A., 2007, ApJS, 170, 228

Murray S. D., White S. D. M., Blondin J. M., Lin D. N. C., 1993, ApJ, 407, 588

Nipoti C., 2010, MNRAS, 406, 247

Nipoti C., Binney J., 2007, MNRAS, 382, 1481

Oosterloo T., Fraternali F., Sancisi R., 2007, AJ, 134, 1019

Pagel B. E. J., 1997, Nucleosynthesis and Chemical Evolution of Galaxies. Cambridge University Press

Peek J. E. G., Putman M. E., Sommer-Larsen J., 2008, ApJ, 674, 227

Pisano D. J., Barnes D. G., Gibson B. K., Staveley-Smith L., Freeman K. C., Kilborn V. A., 2004, ApJL, 610, L17

Rand R. J., 2000, ApJL, 537, L13

Rand R. J., Wood K., Benjamin R. A., 2008, ApJ, 680, 263

Rasmussen J., Sommer-Larsen J., Pedersen K., Toft S., Benson A., Bower R. G., Grove L. F., 2009, ApJ, 697, 79

Reynolds R. J., 1990, ApJL, 349, L17

Reynolds R. J., 1991, ApJL, 372, L17

Richter P., Westmeier T., Brüns C., 2005, A&A, 442, L49

Roe P. L., 1981, Journal of Comp. Phys., 43, 357

Rossa J., Dettmar R., 2003, A&A, 406, 505

Rossa J., Dettmar R., Walterbos R. A. M., Norman C. A., 2004, AJ, 128, 674

Rusanov V. V., 1961, J. Comput. Math. Phys. USSR, 1, 267

Sancisi R., Allen R. J., 1979, A&A, 74, 73

Sancisi R., Fraternali F., Oosterloo T., van der Hulst T., 2008, A&AR, 15, 189

Sarazin C. L., 2009, X-ray emission from Clusters of Galaxies. Cambridge University Press

Sarazin C. L., Irwin J. A., Bregman J. N., 2001, ApJ, 556, 533

Satoh C., 1980, PASJ, 32, 41

Sembach K. R., Wakker B. P., Savage B. D., Richter P., Meade M., Shull J. M., Jenkins E. B., Sonneborn G., Moos H. W., 2003, ApJS, 146, 165

Shapiro P. R., Field G. B., 1976, ApJ, 205, 762

Shu C.-W., Osher S., 1988, Journal of Comp. Phys., 77, 439

Shull J. M., Jones J. R., Danforth C. W., Collins J. A., 2009, ApJ, 699, 754

Sod G. A., 1978, Journal of Comp. Phys., 27, 1

Spitzer Jr. L., 1956, ApJ, 124, 20

Spitzer Jr. L., Jenkins E. B., 1975, ARA&A, 13, 133

Strickland D. K., Heckman T. M., Colbert E. J. M., Hoopes C. G., Weaver K. A., 2004, ApJ, 606, 829

Struck C., Smith D. C., 2009, MNRAS, 398, 1069

Sutherland R. S., Dopita M. A., 1993, ApJS, 88, 253

Tassoul J., 1978, Theory of rotating stars. Princeton Series in Astrophysics, Princeton University Press

Teyssier R., 2002, A&A, 385, 337

Thilker D. A., Braun R., Walterbos R. A. M., Corbelli E., Lockman F. J., Murphy E., Maddalena R., 2004, ApJL, 601, L39

Toro E. F., 1999, Riemann Solvers and Numerical Methods for Fluid Dynamics: Second Edition. Springer–Verlag

Trangenstein J. A., 2009, Numerical Solution of Hyperbolic Partial Differential Equations. Cambridge University Press

Twarog B. A., 1980, ApJ, 242, 242

Vieser W., Hensler G., 2007a, A&A, 472, 141

Vieser W., Hensler G., 2007b, A&A, 475, 251

Wakker B. P., van Woerden H., 1997, ARA&A, 35, 217

Wakker B. P., York D. G., Wilhelm R., Barentine J. C., Richter P., Beers T. C., Ivezić Ž., Howk J. C., 2008, ApJ, 672, 298

Waxman A. M., 1978, ApJ, 222, 61

Westmeier T., Brüns C., Kerp J., 2005, A&A, 432, 937

Wolfire M. G., McKee C. F., Hollenbach D., Tielens A. G. G. M., 1995, ApJ, 453, 673